

INVESTIGATION OF THERMAL MANAGEMENT OPTIONS FOR ROBOTS

by

Eren SEVINCHAN

A Thesis Submitted in Partial Fulfillment

of the Requirements for the Degree of

Masters of Applied Science

in

The Faculty of Engineering and Applied Science,

Mechanical Engineering Program

University of Ontario Institute of Technology

August 2018

ABSTRACT

This thesis research studies the thermal challenges of robots and evaluates the potential thermal management options. In this regard, it aims to develop and analyze various thermal management options for robotic systems. Ten different thermal management options are investigated theoretically in this thesis, such as forced air/liquid systems, heat pipes, thermal interface materials, thermoelectric generators, phase change materials, thermal insulating materials, etc. Three different thermal insulating materials (namely stone wool, fiberglass, and extruded polyurethane) and an air heating/cooling thermal management system are tested at both high and low temperatures. At 40°C, the energy efficiencies for the utilization of these thermal insulating materials are obtained 47.34% for the stone wool, 48.09% for the fiberglass, and 32% for the extruded polyurethane. At the same temperature, the exergy efficiencies for the utilization of these thermal insulating materials are 23.66% for the stone wool, 18.19% for the fiberglass, and 20.73% for the extruded polyurethane. At the -25°C, the energy efficiencies are 49.91% for the stone wool, 48.24% for the fiberglass, and 31.31% for the extruded polyurethane, while the exergy efficiencies for the stone wool, fiberglass, and extruded polyurethane are 17.25%, 21%, and 21.12%, respectively. On the other hand, the energy efficiency of the air cooling system is obtained 37.58% at 40°C, while the exergy efficiency is 5.89%. Finally, at -25°C, the energy efficiency of the air heating thermal management system is 27.32%, and its exergy efficiency becomes 3.60%, respectively.

Keywords: Robots, Thermal management, Efficiency, Heating, Cooling, Electronic Components.

ACKNOWLEDGMENTS

I would like to express my gratitude to my supervisor, Professor Ibrahim Dincer, for giving me this opportunity and supporting me while I am taking an important step on my career path. Also, I would like to thank my co-supervisor, Dr. Haoxiang Lang, for his continuous support during this thesis research.

I would like to thank the members of ACE 3030B laboratory for giving me motivation and huge support throughout my thesis study: Arda Yapicioglu, Anwar Hammad, Ahmed Hassan, Burak Yuzer, Ghassan Chehade, Huseyin Karasu, Haris Ishaq, Maan Al-Zareer, Murat Demir, Mohammed Ra'fat, Osamah Siddiqui and Zeynep Demir. Moreover, I also would like to thank my dearest friends: Ege Yilmaz, Guner Yigit Kuner, Kaan Ayberk Sahinoglu, and Sinan Kahraman who have been motivated me throughout this study.

Last but definitely not least, I would like to express my deepest gratitude to my lovely family: Ezgi Sevinchan, Melek Sevinchan and Mehmet Sevinchan who have been supported me throughout my entire life. Even though they were far away from Canada, I feel their support and love in every single moment of my study.

TABLE OF CONTENTS

ABSTRACT	i
ACKNOWLEDGMENTS	ii
LIST OF TABLES	1
LIST OF FIGURES.....	2
NOMENCLATURE.....	6
CHAPTER 1. INTRODUCTION	1
1.1. Thermal Challenges of Robots	2
1.2. Thermal Management Methods.....	4
1.2.1. Passive Methods	5
1.2.2. Active Methods.....	11
1.2.3. Moisture Control Methods.....	14
1.3. Objectives	15
CHAPTER 2. LITERATURE REVIEW	16
2.1. Thermal Management Options	16
2.1.1. Passive Thermal Management Systems	16
2.1.2. Active Thermal Management Systems.....	19
2.1.3. Hybrid Thermal Management Systems	20
2.2. Evaluation of Thermal Management Systems.....	21
CHAPTER 3. MODELING AND ANALYSIS	25
3.1. Heat Transfer Analysis	25
3.1.1. Conduction Heat Transfer	25
3.1.2. Convection Heat Transfer.....	26
3.2. Thermodynamic Analysis.....	28
3.3. System Modelling.....	28
CHAPTER 4. EXPERIMENTAL APPARATUS AND PROCEDURE.....	35
4.1. Thermal Analysis Experimental Setup	36
4.2. Relative Humidity Analysis Experimental Setup.....	41
CHAPTER 5. RESULTS AND DISCUSSION.....	42
5.1. Theoretical Results	42
5.1.1. Insulating materials Theoretical Results.....	42
5.1.2. Phase Change Materials Theoretical Results.....	55
5.1.3. Air Heating/Cooling Thermal Management System Theoretical Results	63
5.2. Experimental Results	71
5.2.1. Experimental Results at Low Temperature	71

5.2.2.	Experimental Results at High Temperature.....	89
CHAPTER 6.	CONCLUSIONS AND RECOMMENDATIONS	107
6.1.	Conclusions	107
6.2.	Recommendations	108
REFERENCES	109

LIST OF TABLES

Table 1.1. Explanation of IP score method based on ICE 60529.....	4
Table 1.2. Advantages of PCMs based on different properties.....	6
Table 1.3. Thermal conductivity values of various heat sink materials (data from Ref. [52]).	10
Table 2.1. The coefficient of performance range of different active thermal management systems.....	22
Table 2.2. Energetic and exergetic COP values of different air and liquid cooling systems. .	22
Table 2.3. Performance effectivenesses of three different passive thermal management methods.....	23
Table 3.1. Nusselt number equations depending on the geometry of the surface and Rayleigh number.....	27
Table 3.2. Thermal and physical properties of different insulating materials.....	29
Table 3.3. Fire classification of the insulating materials.....	31
Table 3.4. Thermal and physical properties of PCMs.....	32
Table 3.5. Physical properties of different gases at a 15°C temperature and 6 bar pressure...	33
Table 5.1. Uncertainties table for the results of stone wool insulation experiment at low temperature.....	75
Table 5.2. Uncertainties table for the results of fiberglass insulation experiment at low temperature.....	80
Table 5.3. Uncertainties table for the results of extruded polyurethane insulation experiment at low temperature.....	84
Table 5.4. Uncertainties table for the results of stone wool insulation experiment at high temperature.....	92
Table 5.5. Uncertainties table for the results of fiberglass insulation experiment at high temperature.....	97

LIST OF FIGURES

Figure 1.1. Evolution of robotic technologies (Adapted from [1])	1
Figure 1.2. Operating temperature ranges of different type of robots in outdoor conditions (data from ref. [3]).....	3
Figure 1.3. Thermal management methods for electronic components.	7
Figure 1.4. Operating temperature ranges and lower heating values of heat pipe working fluids for cryogenic and low temperature applications.	8
Figure 1.5. Thermal contact conductance comparison of various thermal interface materials [37].	9
Figure 1.6. Thermal conductivity comparison of different insulating materials (data from ref. [55,59,60]).....	12
Figure 1.7. Effective heat transfer coefficients of coolants for indirect liquid cooling systems [73].	13
Figure 1.8. Effective heat transfer coefficients of coolants for direct liquid cooling systems [73].	14
Figure 2.1. Thermal resistance comparison of various thermal interface materials (data from [80]).	18
Figure 2.2. Thermal conductivity and operating temperature comparison of thermal management methods.	23
Figure 2.3. Comparison between price and operating temperature of thermal management methods.	24
Figure 3.1. The concept of the application of the PCM packages.....	31
Figure 3.2. The layout of the air cooling thermal management system.	33
Figure 4.1. The flowchart of the experimental process.	35
Figure 4.2. The testing robot (a) right view, (b) left view, (c) back view.....	36
Figure 4.3. The robot with the stone wool cover in the climatic chamber.....	37
Figure 4.4. The robot with the fiberglass cover in the climatic chamber.....	38
Figure 4.5. The robot with the extruded polyurethane cover in the climatic chamber.....	38
Figure 4.6. The robot with the air cooling/heating thermal management system and the fiberglass insulating material in the climatic chamber.....	39
Figure 4.7. The locations of the K type thermocouples.	40
Figure 4.8. Data acquisition module.	40
Figure 4.9. The locations of the desiccant pack and the humidity sensor.	41
Figure 5.1. The heat transfer rates of different insulating materials corresponding to the change in the ambient temperature.	43
Figure 5.2. The energy efficiencies of different insulating materials corresponding to the change in the ambient temperature.....	45
Figure 5.3. The energy efficiencies of different insulating materials corresponding to the change in the ambient temperature.....	46
Figure 5.4. The heat transfer rates of different insulating materials corresponding to the change in the thickness at high temperature.	47
Figure 5.5. The energy efficiencies of different insulating materials corresponding to the change in the thickness at high temperature.....	49
Figure 5.6. The exergy efficiencies of different insulating materials corresponding to the change in the thickness at high temperature.....	50

Figure 5.7. The heat transfer rates of different insulating materials corresponding to the change in the thickness at low temperature.	51
Figure 5.8. The energy efficiencies of different insulating materials corresponding to the change in the thickness at low temperature.	52
Figure 5.9. The exergy efficiencies of different insulating materials corresponding to the change in the thickness at low temperature.	53
Figure 5.10. The comparison of various insulating materials in terms of their weight.	54
Figure 5.11. The effect of the thickness on the water vapor resistance value of various thermal insulating materials.	55
Figure 5.12. The effect of the ambient temperature on the energy efficiency of the PCMs. ..	56
Figure 5.13. The effect of the ambient temperature on the exergy efficiency of the PCMs. ..	57
Figure 5.14. The effect of the PCMs thickness on energy efficiency at high temperature.	58
Figure 5.15. The effect of the PCMs thickness on exergy efficiency at high temperature.	59
Figure 5.16. The effect of the PCMs thickness on energy efficiency at low temperature.	60
Figure 5.17. The effect of the PCMs thickness on energy efficiency at low temperature.	61
Figure 5.18. The temperature increase of the PCMs by time at high temperature.	62
Figure 5.19. The temperature increase of the PCMs by time at low temperature.	63
Figure 5.20. The effect of the inlet pressure on the energy efficiency of the air heating/cooling thermal management system at high temperature.	64
Figure 5.21. The effect of the inlet pressure on the exergy efficiency of the air heating/cooling thermal management system at high temperature.	65
Figure 5.22. The effect of the inlet pressure on the energy efficiency of the air heating/cooling thermal management system at low temperature.	66
Figure 5.23. The effect of the inlet pressure on the exergy efficiency of the air heating/cooling thermal management system at low temperature.	67
Figure 5.24. The effect of the cold mass ratio on the energy efficiency with different gases. 68	
Figure 5.25. The effect of the cold mass ratio on the exergy efficiency with different gases. 69	
Figure 5.26. The effect of the hot mass ratio on the energy efficiency of the system.	70
Figure 5.27. The effect of the hot mass ratio on the exergy efficiency of the system.	70
Figure 5.28. The temperature distribution of the inside of the robot for stone wool thermal insulating material at low temperature.	72
Figure 5.29. The temperature distribution of the battery and the motor of the robot for stone wool thermal insulating material at low temperature.	73
Figure 5.30. The experimental heat transfer rates of the robot for stone wool insulation at low temperature.	74
Figure 5.31. The energy and exergy efficiencies of the stone wool insulating material at low temperature.	75
Figure 5.32. The comparison between the relative humidity percentages of the inside and the outside of the robot with the stone wool insulating material at low temperature.	76
Figure 5.33. The temperature distribution of the inside of the robot for fiberglass thermal insulating material at low temperature.	77
Figure 5.34. The temperature distribution of the battery and the motor of the robot for stone wool thermal insulating material at low temperature.	78
Figure 5.35. The experimental heat transfer rates of the robot for fiberglass insulation at low temperature.	79
Figure 5.36. The energy and exergy efficiencies of the fiberglass insulating material at low temperature.	79

Figure 5.37. The comparison between the relative humidity percentages of the inside and the outside of the robot with the fiberglass insulating material at low temperature.	81
Figure 5.38. The temperature distribution of the inside of the robot for extruded polyurethane thermal insulating material at low temperature.	81
Figure 5.39. The temperature distribution of the battery and the motor of the robot for extruded polyurethane thermal insulating material at low temperature.	82
Figure 5.40. The experimental heat transfer rates of the robot for the extruded polyurethane insulation at low temperature.	83
Figure 5.41. The energy and exergy efficiencies of the extruded polyurethane insulating material at low temperature.	84
Figure 5.42. The comparison between the relative humidity percentages of the inside and the outside of the robot with the extruded polyurethane insulating material at low temperature. .	85
Figure 5.43. The temperature distribution of the inside of the robot with the air heating thermal management system at low temperature.	86
Figure 5.44. The temperature distribution of the battery and the motor of the robot for the air heating thermal management system at low temperature.	87
Figure 5.45. The experimental heat transfer rates of the robot for the extruded polyurethane insulation at low temperature.	87
Figure 5.46. The energy and exergy efficiencies of air heating thermal management system at low temperature.	88
Figure 5.47. The comparison between the relative humidity percentages of the inside and the outside of the robot with the air heating thermal management system at low temperature.	88
Figure 5.48. The temperature distribution of the inside of the robot for stone wool thermal insulating material at high temperature.	89
Figure 5.49. The temperature distribution of the battery and the motor of the robot for the stone wool insulating material at high temperature.	90
Figure 5.50. The experimental heat transfer rates of the robot for the stone wool insulating material at high temperature.	91
Figure 5.51. The energy and exergy efficiencies of the stone wool insulating material at high temperature.	92
Figure 5.52. The comparison between the relative humidity percentages of the inside and the outside of the robot with the stone wool insulating material at high temperature.	93
Figure 5.53. The temperature distribution of the inside of the robot for the fiberglass thermal insulating material at high temperature.	94
Figure 5.54. The temperature distribution of the battery and the motor of the robot for the stone wool insulating material at high temperature.	95
Figure 5.55. The experimental heat transfer rates of the robot for the fiberglass insulating material at high temperature.	95
Figure 5.56. The energy and exergy efficiencies of the fiberglass insulating material at high temperature.	96
Figure 5.57. The comparison between the relative humidity percentages of the inside and the outside of the robot with the fiberglass insulating material at high temperature.	96
Figure 5.58. The temperature distribution of the inside of the robot for the extruded polyurethane thermal insulating material at high temperature.	98
Figure 5.59. The temperature distribution of the battery and the motor of the robot for the extruded polyurethane insulating material at high temperature.	98

Figure 5.60. The experimental heat transfer rates of the robot for the extruded polyurethane insulating material at high temperature.	99
Figure 5.61. The energy and exergy efficiencies of the fiberglass insulating material at high temperature.	99
Figure 5.62. The comparison between the relative humidity percentages of the inside and the outside of the robot with the extruded polyurethane insulating material at high temperature.	100
Figure 5.63. The temperature distribution of the inside of the robot for the air cooling thermal management system at high temperature.	101
Figure 5.64. The temperature distribution of the battery and the motor of the robot for the air cooling thermal management system at high temperature.	102
Figure 5.65. The change of the cooling power of the air cooling thermal management system in time at high temperature.	103
Figure 5.66. The energy and exergy efficiencies of the air cooling thermal management system at high temperature.	103
Figure 5.67. The comparison between the relative humidity percentages of the inside and the outside of the robot with the air cooling thermal management system at high temperature. ..	104
Figure 5.68. The temperature distribution of the inside of the robot at high temperature. ...	104
Figure 5.69. The temperature distribution of the battery and the motor of the robot at high temperature.	105
Figure 5.70. The experimental heat transfer rates of the robot at high temperature.	106
Figure 5.71. The comparison of experimental and theoretical energy efficiencies.	106

NOMENCLATURE

A	Area (m ²)
C	Coefficients for Nusselt number equations
C _p	Specific heat capacity (kJ/kgK)
D _m	Mass loss percentage (%)
DT	Temperature increase (°C)
FIGRA	Fire Grown Rate Index (W/s)
F _s	Flame spread (mm)
g	Gravitational acceleration (m/s ²)
Gr	Grashof number
h	Heat transfer coefficient (W/m ² K)
k	Thermal conductivity (W/mK)
L	Length (m)
m	Mass of material (kg)
Nu	Nusselt number
p	Perimeter (m)
Pr	Prandtl number
Q̇	Heat transfer rate (W)
Ra	Rayleigh number
R _i	Random error (%)
R	Thermal resistance (K/W)
S	Systematic error (%)
T	Temperature (K)
T _f	Time of sustained flaming of the specimen (s)
THR600s	Total heat release (MJ)
U	Total uncertainty (%)
Ẇ	Work (W)
x	Mean
<i>Greek letters</i>	
ϑ	Kinematic viscosity (kg/ms)
ε	Emissivity
β	Coefficient of volume expansion
μ	Water vapor resistance factor
ε	Performance effectiveness
σ	Stefan-Boltzmann constant
<i>Subscripts</i>	
0	Ambient condition
a	Actual
bevap	Battery evaporator
c	Characteristic length
comp	Compressor
cond	Condenser
conv	Convection
evap	Evaporator
ex	Exergy
l	Latent heat
rad	Radiation
surr	Surrounding air

Acronyms

ARC	Active Refrigerant Cooling
COP	Coefficient of Performance
CPL	Capillary Pumped Loop
GFP	Gas Filled Panel
LHP	Loop Heat Pipe
PCM	Phase Change Material
TIM	Thermal Interface Material
VIP	Vacuum Insulation Panel
WVR	Water Vapor Resistance

CHAPTER 1.INTRODUCTION

With the development of computer technologies, robots and their applications are gradually becoming a part of our life. Robots are able to perform tasks that are not or partly possible for humans. They can be implemented in many different applications such as medical, military, nuclear rescue, space missions and mining. Humanity always makes such tools for themselves to make their daily life more comfortable. With the help of modern technologies, many different mechanical structures with moving parts are developed, which are accepted as the beginning of the robotic technologies. Over the years, people developed the modern world's robots because of exponentially increased knowledge. Eventually, we can see the robots in various areas of our life, and they are going to be a vital part of our daily life in the future. Meanwhile, they are also developed and improved to reduce human errors on sensitive applications, such as surgeries. Therefore, there is no doubt that robots will be our one of the indispensable parts of our daily life in the future. The evaluation and future directions of the robotic technology are illustrated in Figure 1.1.

In this chapter, the thermal challenges of the robots and electronic components are presented. Thermal management solutions are investigated in three different groups, which are passive, active and hybrid thermal management methods. Moreover, current moisture control methods are also presented from a robotic applications point of view.

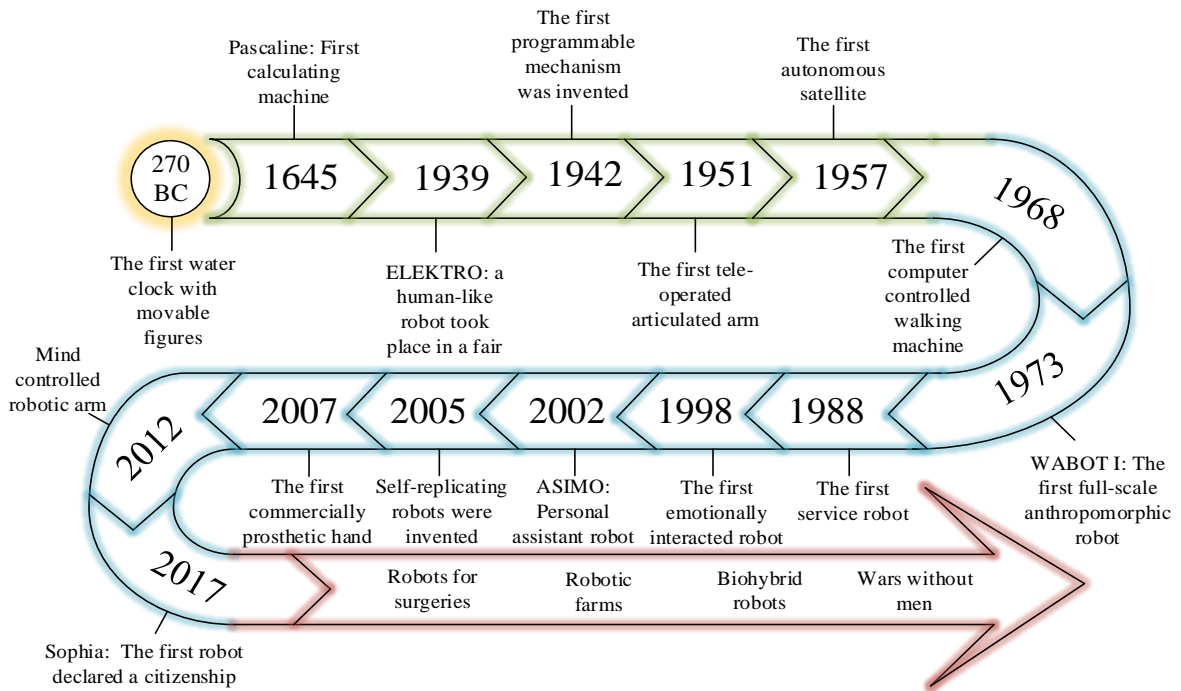


Figure 1.1. Evolution of robotic technologies (Adapted from [1]).

1.1. Thermal Challenges of Robots

Robotic systems are complicated systems consisting of mechanical and electrical subsystems. Some of the subsystems are not capable of running in harsh environments (e.g., low/high temperature, high humidity), especially electronic and electrical subsystems. Therefore, adaptive thermal management systems are required, which can intelligently adjust the thermal condition of the running robot depending on the ambient conditions. A wide range of thermal management systems are developed and improved for other applications, however, it lacks in-depth analyses and development in robotic applications. Therefore, one of the objectives of this thesis aims to review cutting-edge thermal management technologies and provide guideline and instruction for developing a thermal management system for robotic systems.

A practical robotic system should be able to be implemented in real-world environments at both low and high temperatures. Because of the working conditions, robots should be designed to the environment where the robot is operated in. Every electronic component has a range of operating temperature. Therefore, it is crucial to design a system that can maintain the temperature in a certain range so that none of the electronic components will be failed. According to U.S. Air Force estimation, over 55% of problems in electronics are caused by elevated temperature [1]. On the other hand, moisture is another significant factor that needs to be taken into consideration because moisture content of the air directly affects the oxidation of the electrical components, which is a significant cause of a poor performance and short service life. In addition, each type of batteries is also affected by changing of temperature and humidity.

Most of the current robots are not designed for harsh environments. Therefore, they face many challenges of running in real-world scenarios such as low or high temperature, moisture, dust, snow, storm and many other extreme conditions depending on operating conditions. In general, mobile robots should be able to operate at -30°C in winter. During the summer, the overall temperature of the inside of the robot chase could be higher than 50°C . There are other external challenges for robots in real-world applications. For example, relative humidity up to 100%, condensation, possibly highly radiant heat from process equipment, heavy precipitation, splash water, salty air, storms, and direct sunlight can also be observed in some offshore locations and applications [2].

Thermal challenges of robots and electronic components vary depending on the environmental conditions. The operating temperatures of the robots are given in Figure 1.1.

According to Figure 1.1, military robots have the largest range of operating temperature due to their manufacture and material quality. Since the role of the robots in many different areas increased dramatically, more effective, economic, environmentally friend, reliable, lightweight and long-lasting thermal management systems are required [3].

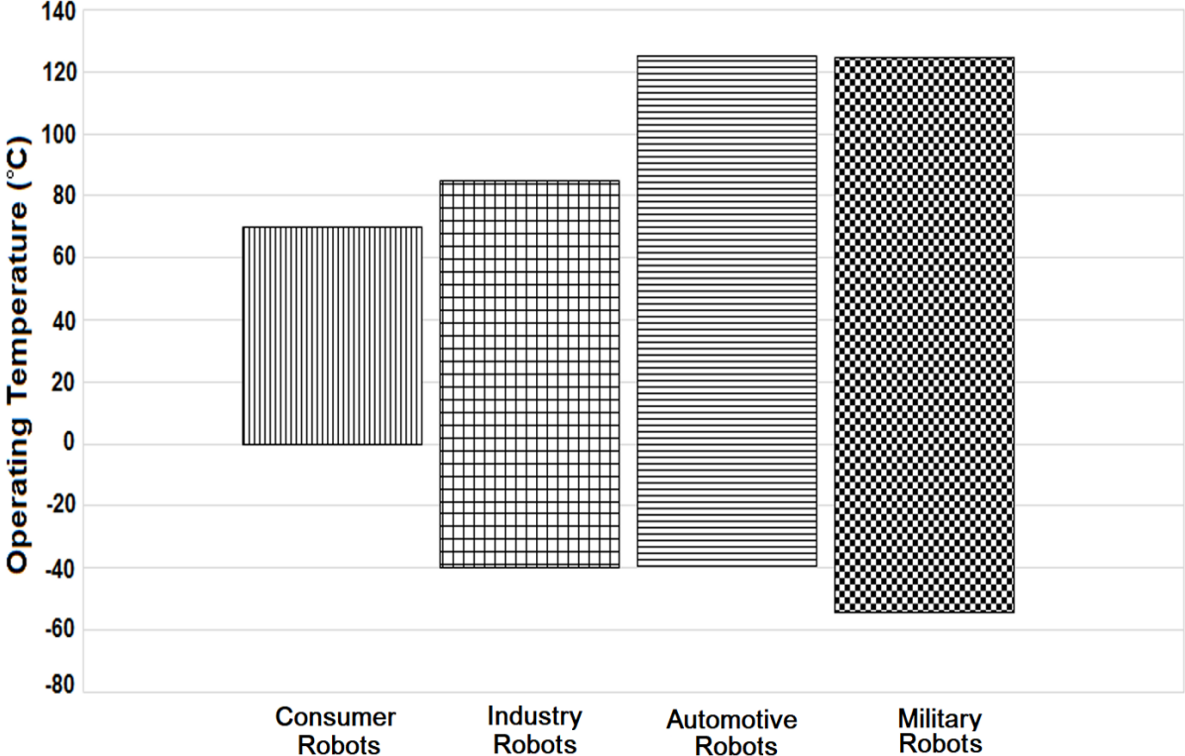


Figure 1.2. Operating temperature ranges of different type of robotics in outdoor conditions (data from ref. [3]).

Because of the fast-developing technology, complex computing electrical systems, such as robots, require more power for higher performance. Since high power dissipation has an impact on system and data center level, the density of the power and its distribution are also significant points for thermal management of robots. However, high power dissipation causes to occur some power-dense areas on die level, which can produce hot-spot regions. For electronic components, overall reliability is defined as the temperature of the hottest point on the die, instead of the average temperature of the component. Therefore, thermal control has a significant role in the reliability of electronic parts and the robot as well [4].

In terms of battery performance, there is a linear relationship between the chemical reaction and temperature. The decrease of the operating temperature will reduce the reaction rate and capacity of the battery during charge and discharge. The reaction rate is increased by higher power and temperature. However, this situation causes to increase heat dissipation and generates higher temperature [2].

Lastly, out of the thermal challenges of the robots, the endurance of robots is indicated in terms of IP score system. Depending on the operation area, dust and water leakages are also some issues for robots. Dust and water protection systems need to be developed for robots based on the operation conditions. Their protection type against solid foreign objects and water ingress can be represented by IP score system. IP score system involves two different digits, which clarify the applied protection systems for the robot. Table 1.1 indicates IP score system and the meaning of the digit numbers.

Table 1.1. Explanation of IP score method based on ICE 60529.

IP	First Digit Number (X)	Second Digit Number (Y)
Protection Type	Solid Foreign Object	Water Ingress Protection
0	No protection	No protection
1	Protected against solid objects up to 50 mm	Protected against vertically falling drops of water
2	Protected against solid objects up to 12 mm	Protected against direct sprays of water up to 15° from the vertical
3	Protected against solid objects up to 2.5 mm	Protected against sprays of water up to 60° from the vertical
4	Protected against solid objects up to 1 mm	Protected against water splashed from all directions
5	Protected against dust	Protected against low pressure jets of water from all directions
6	Totally protected against dust	Protected against strong jets of water
7		Protected against immersion
8		Protected against complete continuous submersion in water
9		Protected against pressure water

Source: [3]

1.2. Thermal Management Methods

Most of the devices need thermal management system depending on their targeted application and working conditions. However, reducing the failures related to low/high temperature or temperature swings are not the only reason to operate a thermal management, it is also essential for a better utilization of the existing hardware of the devices [5]. The thermal management methods should be presented in three different categories, which are passive, active and hybrid thermal management methods. Figure 1.3 shows active and passive thermal management methods, which are operated for robots in both board and system level. Furthermore, all thermal management systems are categorized in terms of their commonly used types and materials for robotic technologies. According to Figure 1.3, passive thermal management methods are heat sinks, heat spreaders, heat pipes, thermal interface materials, phase change materials and

insulating materials, while active thermal management methods are heater units, forced air and liquid control, phase change materials, thermoelectric modules and heat pipes.

1.2.1. Passive Methods

Passive thermal management methods are solutions for electronic components to control their thermal durability without any electrical power input. Passive thermal control systems are commonly used for cooling technologies based on three main heat transfer mechanisms, namely conduction, free convection, and radiation. The most commonly preferred passive thermal management systems for electronics are heat sinks [6–12], heat spreaders [13–16], heat pipes [17–26], thermal interface materials (TIMs) [27–38] and more [39].

1.2.1.1. Phase Change Materials

Phase change materials (PCMs) are considered as the most common and best solutions for thermal energy storage due to their high latent heat capacity. PCMs can be used for both passive and active systems. Battery thermal management of the robots is the most common application area of the PCMs. The process is completed in two stages, which are the storing and releasing the thermal energy at nearly constant temperature. Other application areas of PCMs are heating/cooling of buildings, thermal comfort textile, electric/power peak regulation, battery thermal management, industrial thermal energy storage and solar energy systems. However, they have a limitation because of low thermal conductivity. Moreover, it should be operated carefully due to the leakage problem when the phase change takes place. PCMs can also be operated in microcapsules, which are structures that consist of a central PCM core and organic or inorganic shell material. Mononuclear, polynuclear, matrix and multi-wall are the types of core-shell structures. The process is simple and effective. Table 1.2 indicates the properties of PCMs in terms of their four different features namely thermophysical, chemical, economic and environmental perspectives.

PCMs can be used by different phase change types, such as solid to liquid, liquid to gas or solid to gas. However, the most preferred phase change direction of PCMs is from solid to liquid. As the temperature increases, PCMs change their phases from solid to liquid, meaning that the reaction is endothermic, and PCMs absorb the heat from the heat source. In a similar way, when the temperature decreases, PCMs change their phase from liquid to solid, meaning the reaction is exothermic, and PCMs release the heat [40,41].

PCMs are categorized into three different types, and these are organic, inorganic and eutectic. Organic materials are non-corrosive, low subcooling and compatibility with

conventional construction materials. However, they have low phase change enthalpy and thermal conductivity. Another type of PCMs is inorganic, which has greater phase change enthalpy and low cost. However, they are supercooling, corrosive and phase segregation. The third type, eutectic PCMs, have sharp melting temperatures and high volumetric storage density (higher than organic PCMs). However, they have drawbacks of the limited availability of test data due to the thermophysical properties of eutectic phase change materials [42].

Table 1.2. Advantages of PCMs based on different properties.

Property	Advantages
Thermo-physical	High latent heat potential per unit volume High thermal conductivity Cycling stability Suitable for various applications
Chemical	Non-toxic, non-flammable, non-explosive Durable against corrosion to construction materials Chemically suitable with construction materials
Economical	Economically effective Commercially available
Environmental	Recyclable Low environmental impact Non-polluting during process

Source: Ref. [40,42–44]

1.2.1.2. Heat Pipes

Heat pipes are considered one of the most efficient methods for both passive and active thermal management technologies. They are commonly used for many robotic applications functioning to keep the temperature of the robot's components in a specific operating temperature range. Heat pipes are structures, which have high thermal conductivities. In general, heat pipes are passive thermal management options, which can transport large amounts of heat over long distances. The main structure of heat pipes consists of a tube that involves a working fluid in both fluid and vapor phases. First, the heat that transfers from the electronic devices evaporates the working fluid. Second, the vapor reaches to the condenser as a reason of density difference between the working fluid and vapor. Finally, the working fluid returns to the evaporation section by an influence of gravity or the wick structure of the heat pipe.

Out of the high performance and wide range of operating temperatures of heat pipes, there are some limitations for these devices, which are significant parameters while selecting a heat pipe for a particular operation. Working fluid, wick structure, and dimensions are the main factors of these limitations.

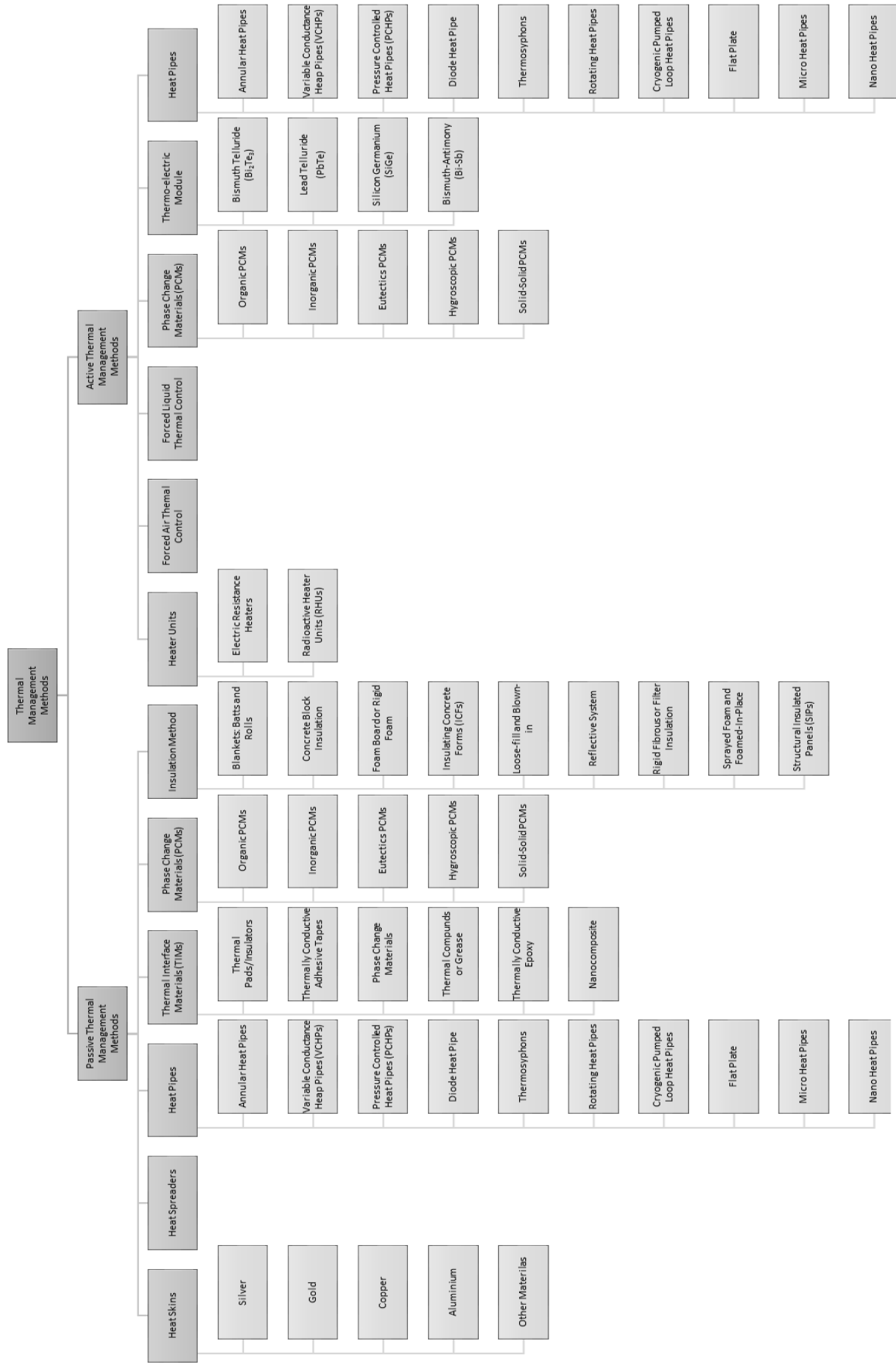


Figure 1.3. Thermal management methods for electronic components of robots.

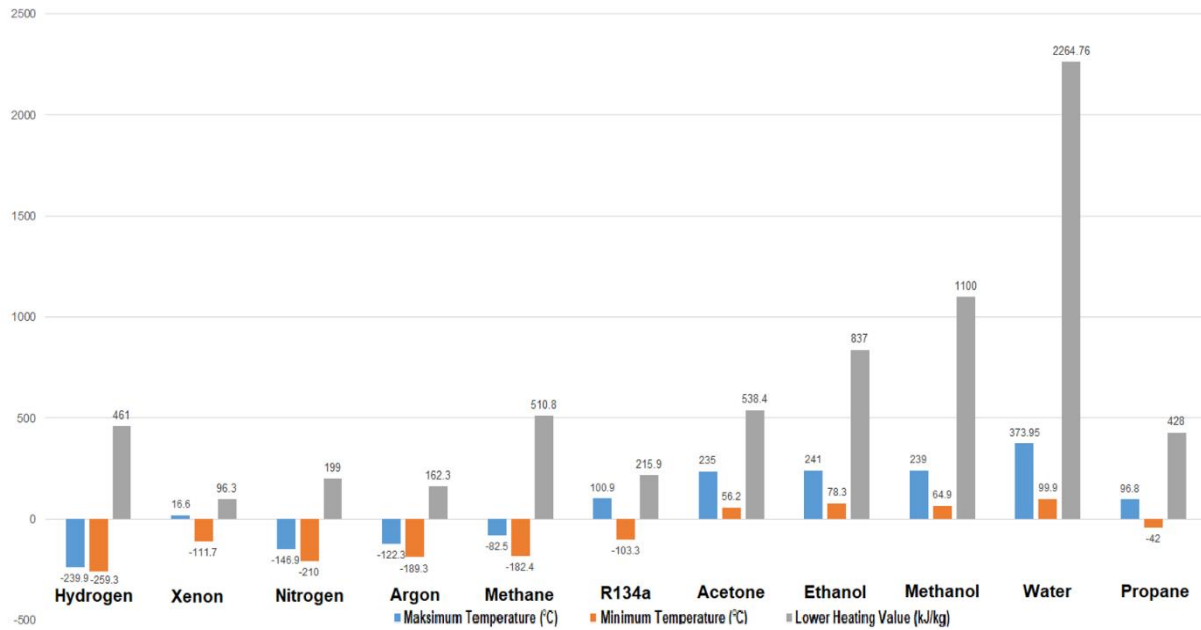


Figure 1.4. Operating temperature ranges and lower heating values of heat pipe working fluids for cryogenic and low temperature applications.

One of these limitations is the capillary limitation, which takes place when the vapor velocity is higher than the velocity of the fluid. Because of this situation, the capillary pressure of the heat pipe may not be enough to pump the working fluid back to the condenser. On the other hand, if the vapor velocity in the heat pipe reaches to the sonic velocity, the sonic limitation should be considered. When the heat pipe operates above the sonic limitation, the heat transfer to the condenser is restricted and causes a choked flow in the heat pipe. However, the third limitation is entrainment limitation, which can be seen when working liquid droplets enter to the vapor, and are transferred to the condenser part. This situation causes to dry out the evaporator part. The boiling limitation is another heat pipe limitation, where the boiling of the working fluid occurs in the wick structure and causes some bubbles that block the liquid flow back to the evaporator. Furthermore, when the pressure gradients of the vapor are very low, it cannot generate a vapor flow. Therefore, the viscous limitation should be considered to prevent this issue in the heat pipe.

Heat pipes are considered as a suitable method for thermal management, which can be widely used for different application types in various environmental conditions. Because of this wide range of application type and easy usage of heat pipes, they are considered as one of the best thermal management options for both passive and active thermal management systems.

1.2.1.3. Thermal Interface Materials

Thermal interface materials are used to increase thermal conduction between two mating parts. They are commonly preferred for the electronic components of robots on both chip and board

levels. They are usually used to improve thermal conduction of another thermal management device, such as heat sinks, heat pipes. They are applied between two surfaces of the electronic device and thermal management unit, such as a heated sink. There are a lot of different types of thermal interface materials (e.g., greases, phase change materials, elastomeric pads, putties, and epoxies). Thermal interface materials (TIMs) are usually manufactured by dispersing higher conductivity particles, such as metals (silver, copper) or ceramics (e.g. aluminum oxide, zinc oxide or boron nitride) within a lower thermal conductivity organic phase, such as silicone grease. In addition, the most effective thermal conductivity of the best commercially available TIMs is between 5 - 10 W/mK [31,45,46]. TIMs have various range of types and application areas. Some of the tested TIMs in terms of different types can be found in following references [47–50]. Figure 1.5 demonstrates the thermal conductance of TIMs to compare their thermal performances.

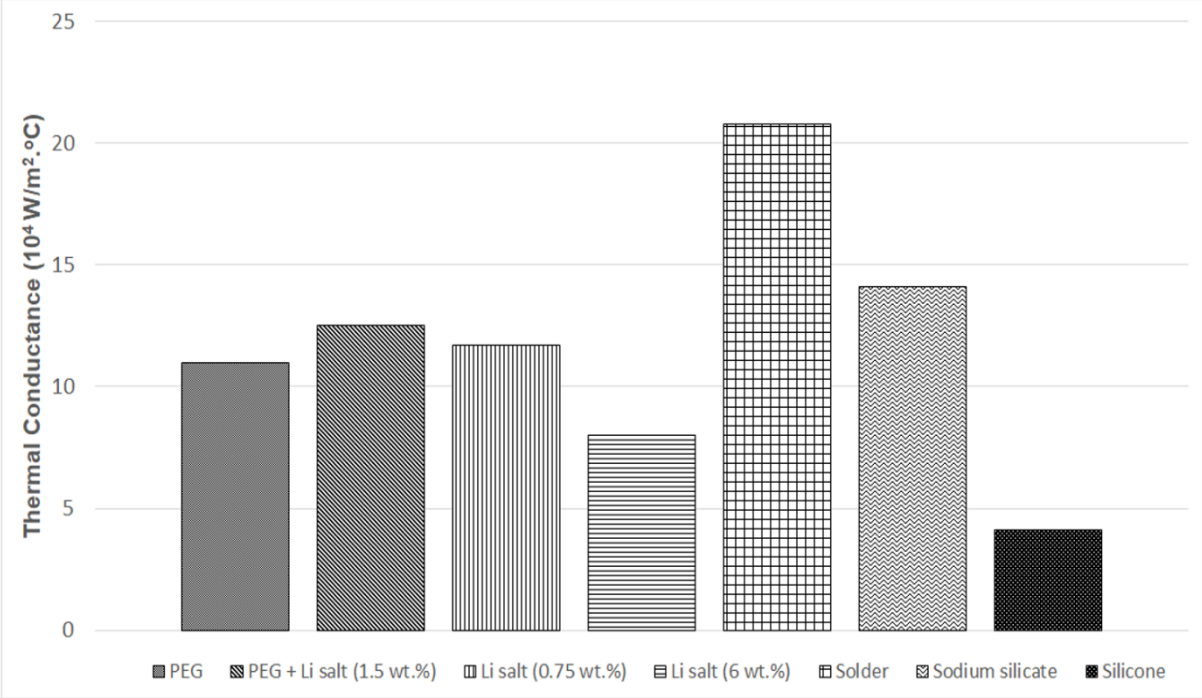


Figure 1.5. Thermal conductance comparison of various thermal interface materials (data from [36]).

1.2.1.4. Heat Sinks and Spreaders

Heat sinks are the simplest and most commonly used passive thermal management method for cooling electronics. The construction of a heat sink is a mass of thermally conductive metal, such as aluminum or copper. Heat sinks are mounted on the main body of electronic components. Two main heat transfer mechanisms take place in this application, which are conduction and convection, respectively. First, the heat transfers from the electronic device or component to the heat sink, which is conduction. Second, the heat sink is cooled by ambient or

forced air, which is a convention. The principle of the process is simple and effective. The heat transfer can be increased by the extension of sinks, which increases the heat transfer surface area [6]. Table 1.3 shows the thermal conductivity values of different heat sink materials, where silver has the highest and commercial bronze has the lowest value. Since heat sinks have a simple application process and relatively cheap components, they are highly effective thermal management methods to be used for electrical component cooling.

Table 1.3. Thermal conductivity values of various heat sink materials.

Material	Thermal Conductivity (W/mK)
Aluminium Alloy 195	170
Aluminium Alloy 2024	178
Aluminum (pure)	240
Bronze (Commercial)	50
Copper (pure)	400
Gold	318
Iron	82
Magnesium	159
Nickel	90
Silicon	148
Silver	432
Yellow Brass	110

Source: Ref. [51]

Heat spreaders are heat exchangers that transfer the heat from electronic devices with a similar working principle of the heat sink. They are usually produced as a plate made of copper that has a high thermal conductivity. They are simple and lightweight devices that can be easily operated for different kind of applications.

1.2.1.5. Thermal Insulating Materials

Since robots can be operated in various harsh environments, insulation of the electronic and mechanical parts of robots is one of the basic methods for thermal management. According to their substances and structures, insulating materials can be categorized into four different groups namely organic, inorganic, combined, and new technology materials. Inorganic materials can be categorized in two different types: foamy and fibrous. Foamy inorganic insulating materials are thermal insulation foams, and fibrous inorganic insulating materials are glass-wool and stone-wool. Moreover, organic insulating materials have three types, foamy, foamy expanded and fibrous. Foamy organic insulating materials are expanded polystyrene, extruded polystyrene, polyurethane foam. Foamy expanded type of organic insulating materials are cork, melamine foam, phenol foam. Finally, fibrous organic insulating materials are sheep-wool, cotton-wool, coconut fibers and cellulose. Siliconated calcium, gypsum foam and wood-

wool are considered as combined insulating materials. In addition, transparent and dynamic materials are defined as new technology insulating materials. Figure 1.6 shows the comparison of thermal conductivities of these insulating materials, which indicated that stone wool has the largest thermal conductivity range between 0.036 and 0.071 W/mK [52,53].

The state-of-the-art insulating materials can be categorized as closed cell foam, vacuum insulation panel, gas-filled panel, aerogel and PCMs. The structure of closed cell foam insulating materials can be established without any connection between bubble cells in the resin bulk. This makes the closed cell foam insulating materials thinner than others. As a comparison, they can save 40% more filling space than glass wool. However, they are not able to be used for cavity surfaces.

The vacuum insulation panels (VIP) are insulating materials, which consist of three main components: the core material, gas barrier/facer foil, and a getter/desiccant. The gas-filled panels (GFPs) are recently advanced technologies for ambient-temperature insulation. Gas-filled panels insulating materials consist of infrared reflecting for low emissivity and multilayers baffles, which are enveloped by a barrier ad, filled up with air or a low conductivity gas.

The aerogel is another substance that is utilized in insulating materials or directly used as an insulating material. Aerogels are produced from the liquid component of a gel that has a supercritical drying feature. The preferred gel to produce aerogel is silica gel because of its high porosity with a huge quantity of tiny air-filled pores. Due to these properties, aerogels have special thermal, physical, optical and acoustic properties. In addition, their thermal conductivities are usually less than 25 mW/mK [86]. PCMs are other materials that are used for insulation applications. PCMs store and release the latent heat that occurs when the phase change takes place. A thin PCM layer can be used for thermally controlling a certain volume. In the literature, there are many different application types of PCMs as insulating materials [54,55].

1.2.2. Active Methods

Active thermal management methods are methods that require electrical power input to control the temperature of the robot properly. Active thermal management methods are usually more complex methods than passive thermal management methods, which have some mechanical components that run working fluids as single or two-phase working principle. The active

thermal management methods that are suitable for robotic applications are heater units, forced air and liquid and thermos-electric generator methods.

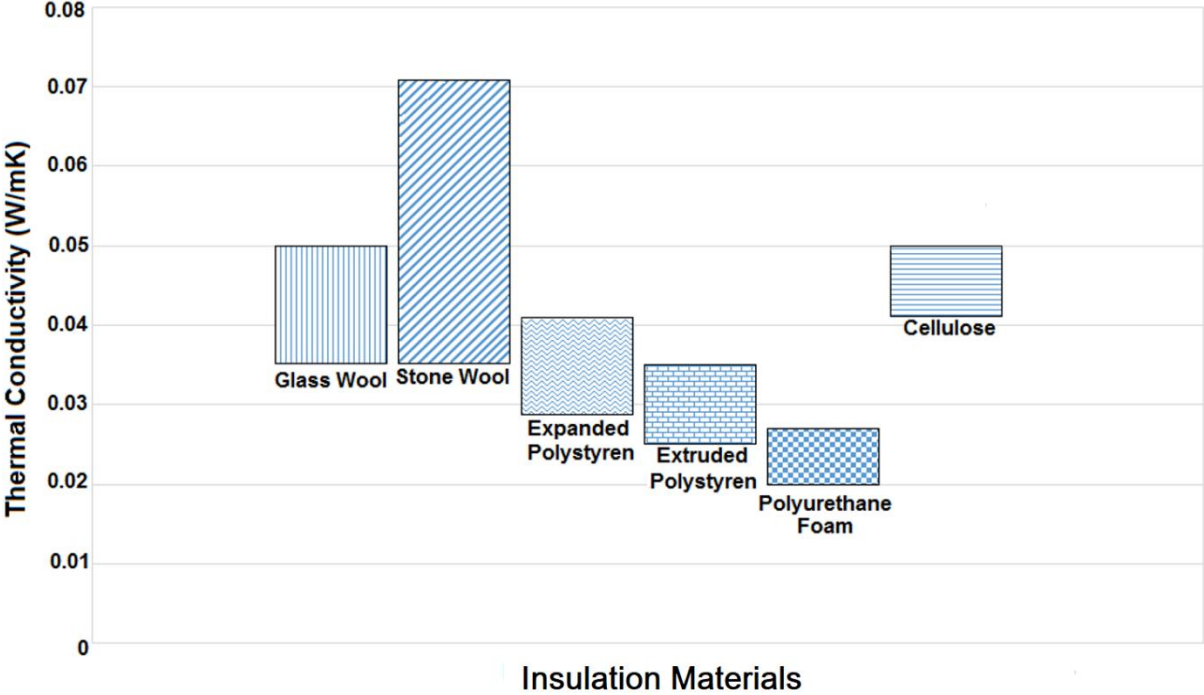


Figure 1.6. Thermal conductivity comparison of different insulating materials (data from ref. [53,56,57]).

1.2.2.1.Heater Units

Heater units are simple devices, which convert electrical power to heat power. Heater units can be operated with many different electricity sources, such as batteries, solar PV panels, and generators. Various types of heater units are widely used for different applications (e.g., heating of electrical components and buildings). Furthermore, they can be used for many different surfaces and volumes because of their flexible production features. Because of their flexible structure, it is easy to see various application types of heater units in the literature [58–60].

1.2.2.2.Forced Air Method

Forced air cooling systems are thermal management systems that utilize the forced air as a cooler by a fan. Depending on the design of the thermal management system, forced air firstly flows into a filtration to avoid pollutant and dust transport, and then a cooling system to absorb the generated heat from electronic devices of robots. On the other hand, if the air can be heated before reach to electronic components, this system can be used as a heating system. Although it is one of the simple thermal management systems, there are some potential issues that should be considered during the design process, such as velocity distribution and pressure loss. Moreover, three main design parameters should be considered (air-inlet angle, air-outlet angle,

and width of the airflow channel). In the literature, there are many different types of forced air applications for cooling of electronic components and batteries [61–65].

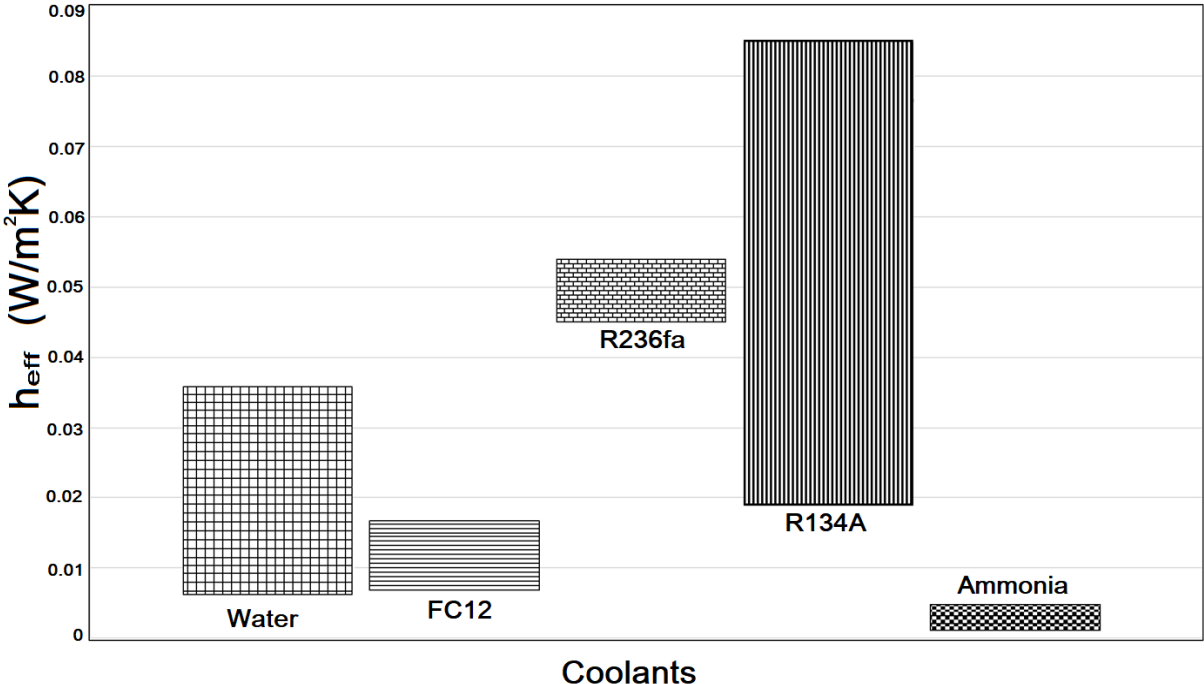


Figure 1.7. Effective heat transfer coefficients of coolants for indirect liquid cooling systems (data from ref.[66]).

1.2.2.3. Forced Liquid Method

Forced liquid thermal management systems can be preferred for both cooling and heating. The structure of the system involves heated/cooled plates, which are located by the surface and consists of tubes and working fluid. The working fluid for this operation can be water, glycol, oil, acetone or refrigerant. The forced liquid thermal management systems are more complicated systems than forced air systems. Figure 1.6 shows effective heat transfer coefficients of different coolants, which are used for indirect liquid cooling systems of electronics, while Figure 1.7 presents the same parameter of various coolants for direct liquid cooling systems. There are various application types of forced liquid cooling systems for battery thermal management and robotic operations in the literature [67–70].

1.2.2.4. Thermo-electric Generators

The thermoelectric generator is a technology that enables both cooling and heating applications. The working principle of the thermo-electric generator is that when electric current flows between two different types of semiconductor metals, the electric current generates heat that is transferred from one surface to another. While one surface is cold, the other one starts to heat up. If the direction of the electric current is changed, the hot and cold surfaces are switched.

Some special assessments should be studied in the production or application of thermo-electric generators, such as thermoelectric materials [71,72], manufacturing process [73], cost analysis [74], the geometry of modules [75] and electricity consumption [76].

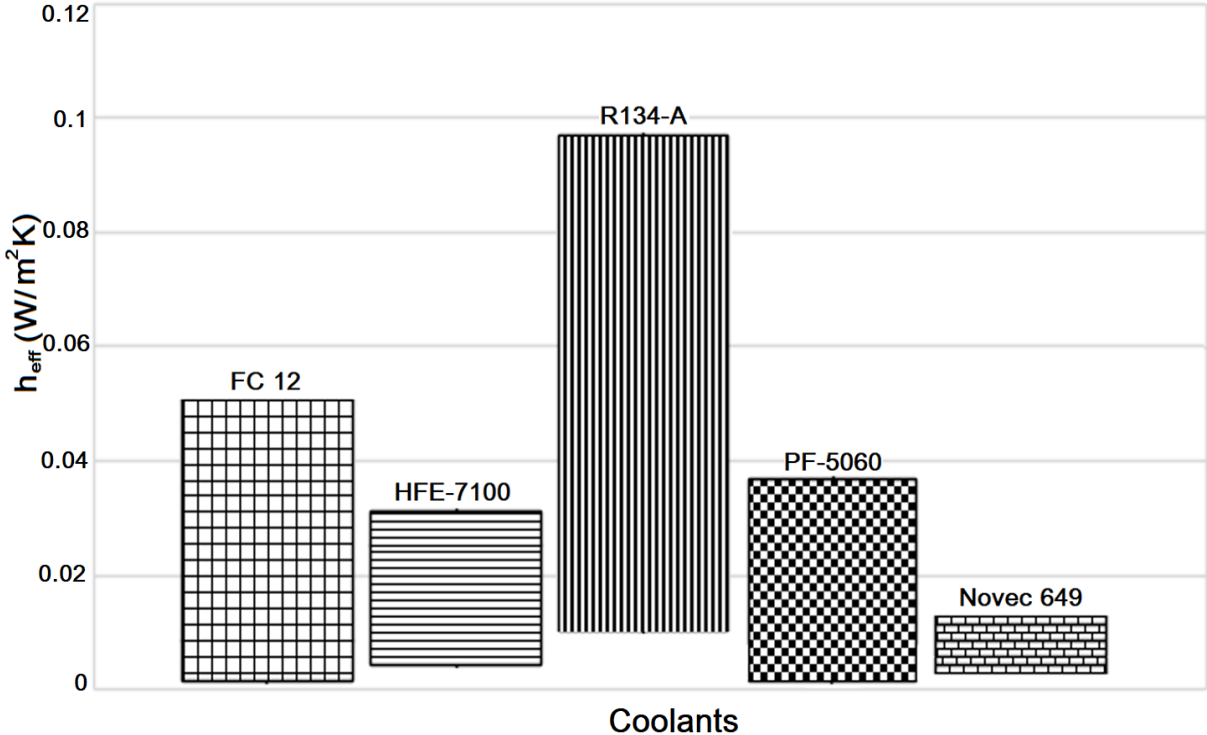


Figure 1.8. Effective heat transfer coefficients of coolants for direct liquid cooling systems (data from ref. [66]).

1.2.3. Moisture Control Methods

The moisture control is one of the main challenges of robots, and other electrical and mechanical devices. The moisture of inside of the robot should be kept as possible as low during the operation. The relative humidity content of inside of the robot is also significantly related to the relative humidity content of the environment where the robot is operated in. Since the humidity moves from the higher humidity content to lower humidity content, this humidity transfer between the inside and outside of the robot occurs in two ways. However, the relative humidity is also related to the ambient temperature as well. There is a lot of different types of moisture control methods and materials, such as vapor barriers, and desiccants.

There are some fabrics that are specifically manufactured to keep the moisture or avoid the moisture transfer between two surfaces. Super absorbent fabrics are one of them, which can absorb ten times its weight in moisture. The rated absorption time of the superabsorbent fabrics is 0.5 seconds, and these fabrics are anti-microbial options. On the other hand, bamboo fabric is also another type of fabric that is produced to be used as moisture absorption fabric. Bamboo

fabrics can absorb three times its weight in moisture, and these materials are environmentally friendly. The bamboo content of these fabrics is 70%. Lastly, hemp fabric can be also used as moisture absorption fabrics, which has a good performance and able to absorb three times of its weight in moisture. Moreover, hemp fabric is also an environmental friendly option because of its plant-based structure.

1.3. Objectives

The main objective of this thesis is to develop a thermal management system for a mobile robot, which makes the robot enable to operate at low and high ambient temperatures, and preserves the electronic components of the robot against high relative humidity. The specific objectives of the thesis are listed as follows:

- To develop the thermal issues of the robot, which may be a significant problem while the robot is operated at both harshly low and high ambient temperatures, critical electronic components and locations on the robot. Then, to compare various thermal management systems and methods for the robot to obtain the best solution based on different ambient conditions.
- To analyze the performance of various thermal management systems on the robot theoretically to gain an idea to determine the most suitable and effective thermal management system for the robot.
- To perform theoretical parametric analyses for the robot to understand clearly the performance of the designed thermal management system under various environmental conditions.
- To design a thermal management system for the mobile robot based on theoretical analyses, which should be suitable to operate at both high and low temperatures.
- To assemble the thermal management system on the robot and develop an experimental setup. Then, to analyze the thermal management system experimentally at various temperatures and relative humidity ranges to obtain the thermal behavior of the robot.

CHAPTER 2.LITERATURE REVIEW

In this chapter, the status of the mobile robot technology, thermal management options and the evaluation of these systems are discussed. Thermal management options are investigated from the robotic applications point of view to obtain an idea about the thermal performance of different thermal management systems in the literature.

2.1. Thermal Management Options

In this section, various thermal management systems, which aim to achieve a better performance with robotic applications, are investigated. These thermal management systems have different operating temperatures corresponding to the thermal management need of the operation based on the electronic components of the robot. As it is discussed before, electronic components can be operated only in their specific temperature and moisture ranges. Because of these limitations, robotic systems should be operated with a thermal management system to achieve a better performance. Furthermore, in some cases, the current material technology could not be enough, such as space missions. Therefore, thermal management systems become a vital part of the overall system. As a result of one of the main requirements of the robotic applications, various thermal management systems are developed and operated under different operating conditions. These systems can be studied in three different groups, which are passive, active and hybrid thermal management systems.

2.1.1. Passive Thermal Management Systems

Passive thermal management systems are such structures that do not require any electrical power input. These systems are operated by following three main heat transfer mechanisms, which are conduction, free convection, and radiation. These thermal management systems contain one or multiple operations of different passive thermal management methods, such as PCMs, TIMs, heat pipes, thermal insulating materials, heat sinks and heat spreaders. In some cases, it can be clearly sufficient to operate only one of these passive thermal management methods, but mostly they are operated as multiple systems to obtain a better thermal performance for the robot.

In the literature, heat pipes are commonly analyzed for thermal management of batteries. However, they are able to be located in many different hot regions in the robots, as they have various shape and dimensions based on the operating conditions. Rao et al. [45] studied the performance of a heat pipe, which consists of water as a working fluid for battery thermal management. According to their study, the temperature of the battery can be kept between 24

°C and 44°C, which is almost in the range of the best operating temperature of Li-ion batteries [45]. On the other hand, Tsai et al. [77] investigated another study, which shows the effect of the nanoparticle usage in heat pipes. They studied the thermal performance of a heat pipe with gold nanoparticles. According to their results, the thermal resistance of circular heat pipes varies between 0.17°C/W and 0.215°C/W. Furthermore, they also mention that the thermal resistance of heat pipes with a nanoparticle solution is lower than the heat pipe with DI water [77]. Wang et al. [78] analyzed an experimental study for asymmetrical heat pipes. They operated the asymmetric heat pipe with Freon 11 and 113 working fluids, and their results show that the average heat transfer coefficient of the heat pipe is 12.4W/m²°C for the heat flux in the range of 425 - 1780 W/m² [78].

Heat pipes have various parameters, which should be considered while thermal assessment, such as viscous limit, sonic limit, entrainment limit, capillary limit, boiling limit, wick characteristic and working fluid. The viscous limit is seen when the operating temperature and the operation heat load are low [79]. The sonic limit shows the maximum acceptable mass flow and heat transfer rates that directly affect the performance of the operation. When the vapor reaches to the sonic speed, choked vapor flow rate occurs[79]. Entrainment limit occurs at the outer surface of the primary wick. The capillary limit is seen when the evaporator does not has sufficient capillary pumping pressure for dealing with the overcome pressure losses. Finally, the boiling limit occurs when the boiling still takes place below the heating surface when the heat load of the heat pipe is extremely high [79].

Thermal interface materials are the passive thermal management methods that are only operated with other passive thermal management systems. Thermal interface materials are thermal management options for electronics, which increase the thermal conduction between two layers. They are usually used between electronic components and heat sinks. Goyal et al. [57] studied the hybrid graphene-metal nano-micro-composite applications in thermal interface materials. They mentioned that the thermal conductivity of thermal interface materials with the hybrid graphene-metal particle increases almost 500% between the temperature ranges from 300K to 400K at 5-vol.-% graphene loading fraction. Furthermore, they also estimate that the thermal conductivity of the thermal interface material increases due to the increase of the temperature. From 15°C to 75°C, the thermal conductivity increases slightly from almost 9.5W/mK to 10.5W/mK [57]. As another research, Hamdan et al. [80] investigated characterization of liquid–metal microdroplet thermal interface materials. They express that the thermal resistance can be as low as 0.253×10^{-7} m²K/W for the thermal interface material that

consists of an array of mercury microdroplets deposited in a silicon die [80]. In Figure 2.2, thermal resistances of six different thermal interface materials are compared by their thicknesses. There is no doubt that the thermal resistance of thermal interface materials increases corresponding to the increase of the thickness. However, the best performance can be seen with Aavid Thermalloy Thermalcote among these TIMs, while the poorest performance can be obtained for Thermaxtech Xt-flux-GA.

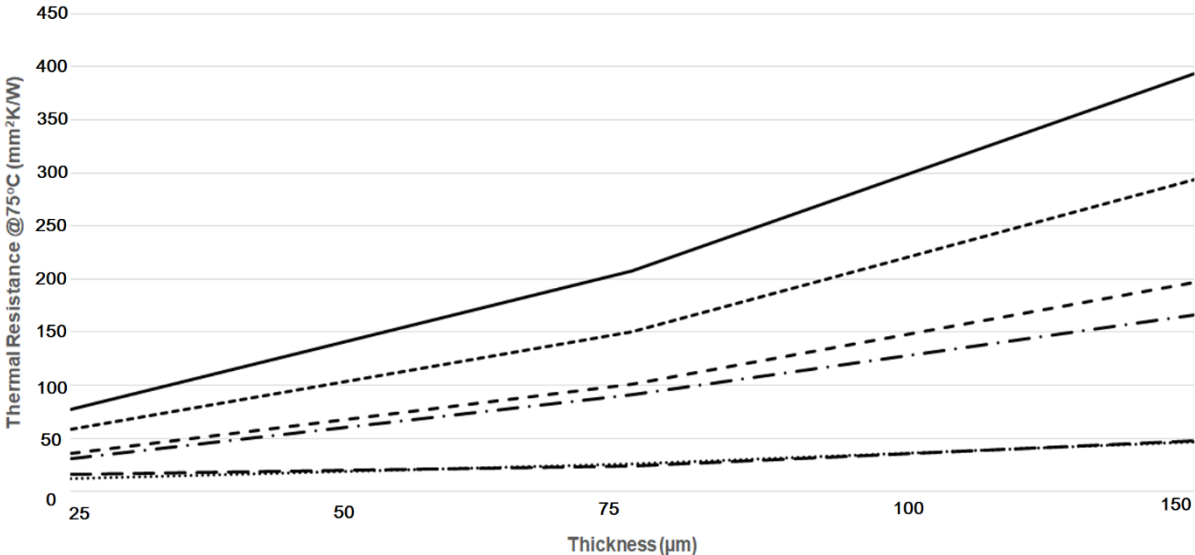


Figure 2.1. Thermal resistance comparison of various thermal interface materials (data from [81]).

In some operating conditions, the thermal management solution may be only one of the passive thermal management methods. As an example, passive thermal management methods are only solutions for the mobile robots operating in the areas where nuclear leakage takes place, since fans and pumps are fragile under nuclear conditions. Yanlong et al. [26] studied the performance of PCMs to prevent the robot against overheating on the motor drivers. Although the maximum temperature to shut-off the motor is around 88 °C, the maximum driver temperature is 60 °C in two hours. In the experimental setup of the study, 65 kg OP44E PCMs that have a melting temperature between 42°C and 53.6°C latent heat are filled in a support frame. Two electric heaters are placed on two sides of the support frame, and the heater power is fixed to 2.8W to simulate the heat generation on the motors. In this study, the change in the heating surface temperature is analyzed for two different conditions, which are the operation with thermal protection and without thermal protection. The temperature of the system without thermal protection increased quickly to 80.1 °C in 15 minutes, and then it went up to 91.0 °C in 100 minutes. On the other hand, the temperature of the system with thermal protection increased slightly at the beginning of the experiment and reached to almost 50°C. From the 7th minute to

50.5th minute, the temperature stayed almost constant, when PCM absorbs the heat from the system [26].

2.1.2. Active Thermal Management Systems

Active thermal management systems are other structures that require an electrical power input to operate the system properly. In this case, there should be a power supply in these systems, which may vary depending on the operating conditions, such as batteries, and solar PVs. These active thermal management systems are more complex and relatively expensive systems than passive thermal management systems. Forced liquid, forced air, thermo-electric generators and heater units can be considered as the main active thermal management methods that can be operated for robotic applications.

The liquid cooling thermal management system for robots in temperature-restricted environments involves a liquid that is able to absorb the heat by convection heat transfer from the motors and electronic components and releases this heat to the environment. A pump circulates the liquid through the system at a determined mass flow rate by the loop controller. The controller is also able to check the speed of the motor and the heat output depending on this speed. Therefore, the system has four main outputs, which are the liquid temperature, environment temperature, motor speed and motor temperature. On the other hand, the system inputs are defined based on the robot motor speed demand and fluid pump volumetric flow demand. According to their results of trapezoidal velocity input, motor temperature increases from -42°C to 155°C after 12000 seconds, while fluid temperature goes up from -42°C to nearly 35°C. After 2000 seconds, the motor temperature decreases to around 90 °C, while fluid temperature increases slightly to 40 °C [82]. On the other hand, Table 7 compares three different air and liquid cooling system COP values, which are designed for battery cooling applications.

Motors are significant parts of robots, which should be studied carefully and operated with a thermal management system to avoid the overheating. A forced-liquid cooling system for motors of a humanoid robot is developed by Urata et al. [70]. In their system, the temperature of the motors is enabled to be checked by a temperature sensor on the motor and to be controlled by water passing through the motor and then goes to the radiator. According to their results, although the estimated core temperature of the motor was almost 80°C in 5 seconds, the temperature reached to around 40°C. However, the timing of the operation is one of the biggest problems, which should be solved by designing a special method with thermal estimation.

The liquid-cooled cold plates in a humanoid robot for multiple heat sources are studied in reference [83]. In this study, the experiments are analyzed to compare two different array types of cold plates, which are attached to multiple heat sources. Six cartridge heaters are used to simulate heat generation. However, the cold plates consist of a metal case and non-metallic material of PC cover. These heat sources and cold plates are attached to each other and the performance of the liquid-cooled cold plates is analyzed. According to their result, two-way parallel circulation has better thermal performance in all cases [83].

2.1.3. Hybrid Thermal Management Systems

Thermal management systems vary based on the application area of the robotic operation. Robots are usually able to operate in extreme conditions, such as low/high temperature, low/high pressure. Two-phase thermal management technologies, such as loop heat pipes (LHPs) and capillary pumped loop (CPL), are widely used for robots working in extreme conditions. Two-phase technology is already used by NASA and commercial applications. As an example, Terra spacecraft has three CPLs, which operate successfully since launch [41]. In July 2001, the ASTER-SWIR device, one of the thermally conditioned devices with CPL, was exposed to extreme temperatures. The CPL's temperature control point is set to orbit to compensate for this temperature increase, thus the life of the instrument is extended. Another space shuttle that has CPLs is Hubble Space Telescope (HST), which operates a CPL to absorb the heat from new NICMOS cryocooler in the aft shroud. In the March of 2002, astronauts working at the HST / Service Mission - 3D installed a CPL evaporator under the aft shroud, attached to the new NICMOS cryocooler, and installed a new radiator on the external guardrail. According to the flight data, the new cooling system, which consists of cryocooler and CPL, successfully decreased the temperature to the required operating temperature, which is 70 K [84].

The LHPs are currently used in TES instrument of AURA Spacecraft, the BAT instrument of SWIFT instrument and GLAS instrument, which have 120W thermal load, of ICESAT spacecraft [8]. However, there are also some issues with CPL and LHP technologies, such as the significant amount of engineering ability to design the technology and required preconditioning before the start-up. On the other hand, existing two-phase technologies can be reliably implemented, and they offer significant design flexibility, tight temperature control, large heat carrying capacity, diode function and isothermalization [84].

Another thermal management method, which is used for NASA Spacecraft, is single-phase cooling system. In this system, a single-phase liquid is circulated by a mechanical pump

to remove the heat from the hot robotic equipment. This system is used for the first time for a long-term robotic mission of Mars Pathfinder in 1996. This system provided the thermal needs of the spacecraft for over seven months during the mission [84].

2.2. Evaluation of Thermal Management Systems

Thermal management systems can be compared to each other in terms of different parameters, such as coefficient of performance (COP), performance effectiveness (ε), cost, operating temperature, and thermal conductivity range. Although some of these parameters are suitable to analyse both passive and active systems, some of them should be considered for particular groups, such as COP and performance effectiveness.

The coefficient of performance is a value that indicates the thermal performance of a thermal management system. However, the thermal management system should be an active or hybrid system to define a COP value, since COP is a ratio of useful heat output of the system and net power input. COP can be defined as

$$COP = \frac{\dot{Q}_{out}}{\dot{W}_{in}} \quad (2.1)$$

where \dot{W}_{in} indicates the net electrical power input of the thermal management system, and \dot{Q}_{out} is the useful heat output of the system. This equation may be applied for different active thermal management systems to estimate the thermal performance of the system. Therefore, the net power input and useful heat output of the system may vary depending on the structure and application purpose of the system. To illustrate that, COP of an active refrigerant cooling system can be defined as,

$$COP_{arc} = \frac{\dot{Q}_{evap} + \dot{Q}_{b,evap}}{\dot{W}_{comp}} \quad (2.2)$$

where *evap*, *bevap* and *comp* indicate evaporator, battery evaporator, and compressor power, respectively. In Table 2.1, COP ranges of different active thermal management systems are represented. There is no doubt that it is possible to design various active thermal management systems depending on the cooling or heating requirements of the operation. In Table 2.1, it can be obtained that active refrigerant cooling thermal management systems provide the highest range of COP values from 0.24 to 2.32, while thermo-electric generators have the poorest performance among the others with the range of 0.267 – 0.618.

Table 2.1. The coefficient of performance ranges of different active thermal management systems.

Active Thermal Management Methods	COP Range	Ref.
Thermoelectric modules	0.267 – 0.618	[68,85]
Active air cooling	0.58 – 2.12	[86]
Active refrigerant cooling	0.24 – 2.32	[86]
Heat sink – Thermoelectric module combination	0.21 – 1.4	[68]

To obtain a more accurate comparison of active thermal management systems, exergetic COP of the systems should be considered as well. The exergetic COP is defined as

$$COP_{ex} = \frac{\left(1 - \frac{T_0}{T_s}\right) \dot{Q}_{out}}{W_{in}} \quad (2.3)$$

where T_0 is ambient temperature, and T_s indicates surface temperature. Table 2.2 shows energetic and exergetic COP values of different active thermal management systems for battery cooling, where cabin air cooling is operated with the highest energetic and exergetic COP values, and refrigerant-cooler cooling has the lowest energetic and exergetic COP values. This situation proves that higher cooling performance can be achieved with lower energy input into the system, such as a simple fan of a cabin air cooling system.

Table 2.2. Energetic and exergetic COP values of different air and liquid cooling systems.

Thermal Management Systems	Energetic COP	Exergetic COP
Cabin Air Cooling	2.18	0.32
Direct Refrigerant Cooling	2.07	0.30
Refrigerant and Cooler Cooling	2.05	0.30

Source: Ref. [68]

Since passive thermal management systems do not require any electrical power input, the coefficient of performance cannot be defined as a thermal performance comparison parameter. In order to estimate a thermal performance parameter for passive thermal management systems, performance effectiveness value can be defined. Performance effectiveness is a ratio of actual heat transfer between two layers with the passive thermal management system and maximum heat transfer without any passive thermal management system. Therefore, performance effectiveness can be defined as

$$\epsilon = \frac{\dot{Q}_a}{\dot{Q}_m} \quad (2.4)$$

where subscripts of a and m indicate actual and maximum heat transfer rates between two layers, respectively. Table 2.3 shows the performance effectiveness of different passive thermal management systems, where PCMs have the highest ratio and heat pipes has the lowest range of performance effectiveness value.

Table 2.3. Performance effectiveness of three different passive thermal management methods.

Passive Thermal Management Method	Performance Effectiveness	Ref.
Phase Change Materials	0.64 – 0.98	[87]
Heat Pipes	0.1 – 0.54	[88]
Thermal Interface Materials	0.12 – 0.75	[89]

Figure 2.2 illustrates the comparison of four different active and passive thermal management methods in terms of their operating temperatures and thermal conductivities. In Figure 2.2, it is clear that thermal interface materials have the highest range of thermal conductivity, which is one of the main application purposes of thermal interface materials. Since increasing the thermal conductivity between two surfaces is the main application purpose of a thermal interface material, this situation can be seen properly. However, thermo-electric generators have the lowest range of thermal conductivity values, as a reason of limited material options of this thermal management method.

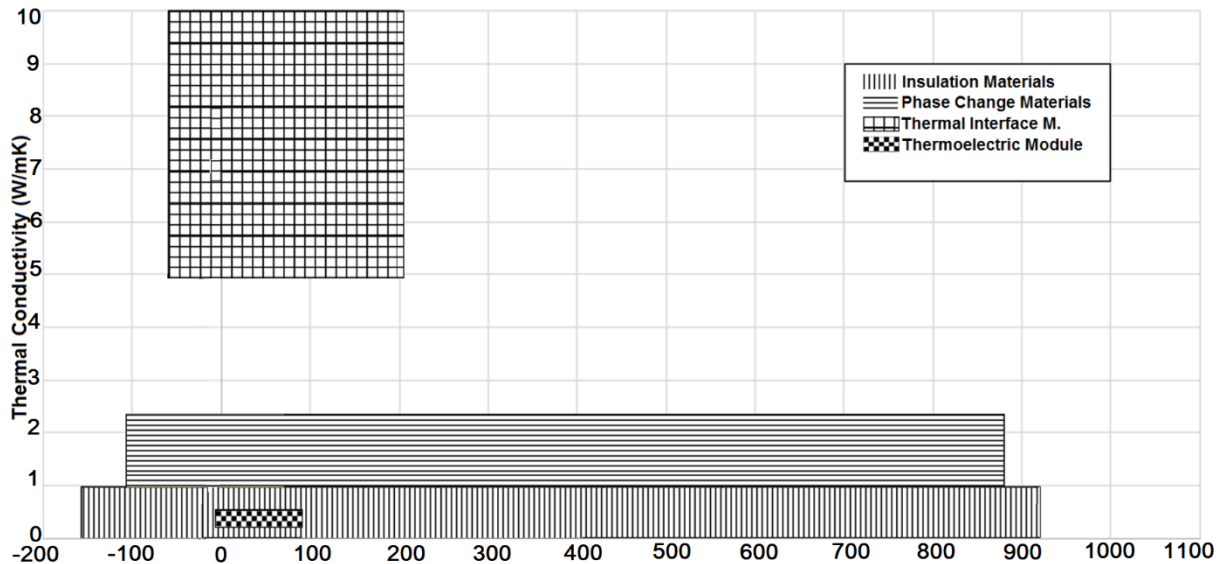


Figure 2.2. Thermal conductivity and operating temperature comparison of thermal management methods.

In Figure 2.3, PCMs, heat pipes, thermo-electric generators and thermal interface materials are analyzed in terms of their costs and operating temperatures. The heat pipes have the largest range of operating temperature, which makes them one of the best solutions for the robotic applications at low and high ambient temperatures. From the cost point of view, thermal interface materials and thermo-electric generators have the lowest range of the cost, where the cost of TIMs varies between almost \$10 and 60\$.

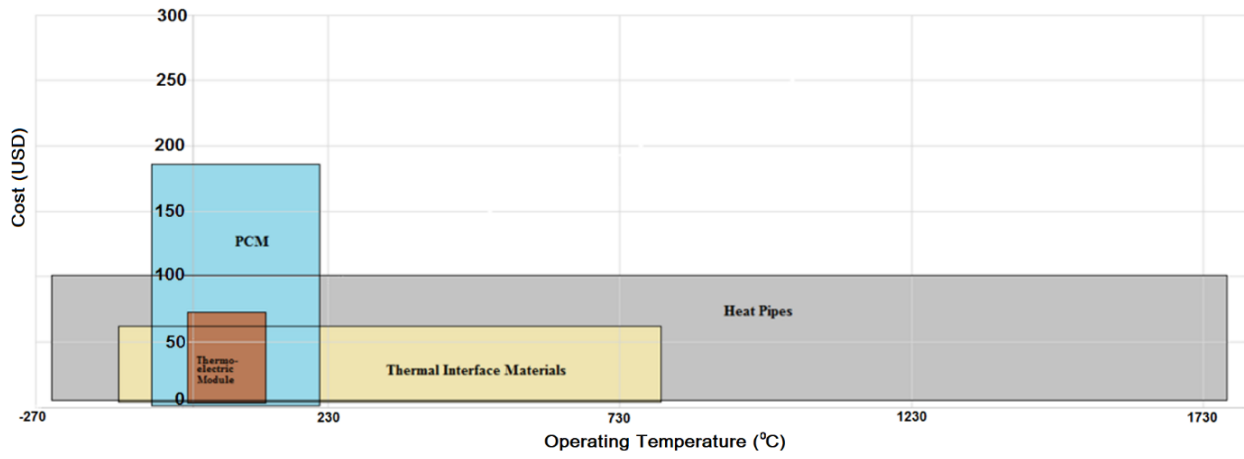


Figure 2.3. Comparison between price and operating temperature of thermal management methods (data from ref. [90]).

CHAPTER 3. MODELING AND ANALYSIS

In this chapter, the developed model for the heat transfer and thermodynamic analyses of the study is introduced. Conduction, convection, and radiation heat transfer mechanisms, and thermodynamic analyses are investigated for the thermal insulating materials, phase change materials, and an air cooling/heating thermal management system.

3.1. Heat Transfer Analyses

The heat transfer model is created for simulating the heat dissipation on the surface and temperature distributions on different regions of the robot. Therefore, the combined heat transfer mechanism is considered during the heat transfer analyses of the system. In this case, three heat transfer mechanisms, which are conduction, convection, and radiation, are considered to obtain a combined heat transfer analysis. The following assumptions are made in order to perform the thermodynamic and heat transfer analyses of the thermal management methods:

- The initial temperature of the robot is 25°C.
- The ambient temperature during the analyses varies between -25°C and 40°C to obtain the thermal performance of the thermal management methods at different ambient temperatures.
- The inside of the robot and ambient pressures are 101.325 kPa.
- The thickness of the wall of the robot is 1.58 millimeters, and the thermal conductivity of the surface material is 50W/mK.
- In theoretical analyses, the thickness of the thermal insulating material is 15 mm.
- The thickness of the PCMs packages is 10 mm.
- The cold mass friction of the air cooling thermal management system is 0.5 at the beginning of theoretical analyses.
- The compressed inlet air pressure of the air cooling/heating thermal management system is 6 bar.

3.1.1. Conduction Heat Transfer

Conduction is a heat transfer mechanism that occurs as a result of interactions between the particles from high energy to low energy. Conduction heat transfer can be seen in solids, liquids, and gases, where diffusion and collisions during the random motions of the molecules of liquids and gases happen. However, conduction mechanisms take place in solids as vibrations and energy transportation by free electrons. The rate of the heat transfer through a medium depends on three main parameters for conduction heat transfer, such as thickness and material of the

medium, and temperature difference across the medium. The rate of heat conduction is defined as

$$\dot{Q}_{cond} = kA \frac{T_1 - T_2}{\Delta x} = kA \frac{\Delta T}{L} \quad (3.1)$$

where k is the thermal conductivity of the material, A is the area of the surface, $\Delta x = L$ is the thickness of the material and $\Delta T = T_1 - T_2$ is the temperature difference through the medium.

3.1.2. Convection Heat Transfer

Convection heat transfer is a different kind of heat transfer mechanism between a surface and other moving liquids or gases. There is a linear relationship between the heat transfer rate and fluid motion. The conduction heat transfer can be seen in two different types, such as forced and natural convection. Forced convection heat transfer occurs, if the fluid is forced by an external fan, pump, or naturally wind. On the other hand, natural convection heat transfer is seen without these external effects. Natural convection heat transfer is a reason of buoyancy forces that occur when there is a temperature difference between any object and the environment. Convection heat transfer is a complex mechanism, which can be expressed by Newton's law of cooling,

$$\dot{Q}_{conv} = hA_s(T_s - T_\infty) \quad (3.2)$$

where h is the convection heat transfer coefficient, A_s is surface area where convection heat transfer takes place, T_s and T_∞ are the surface and fluid temperatures, respectively.

Furthermore, natural heat convection is a convective heat transfer mechanism, which depends on the geometry and orientation of the surfaces. To obtain a convective heat transfer rate, the convection heat transfer coefficient should be defined first. Nusselt number is one of the values that is defined by the convective heat transfer coefficient as

$$Nu = \frac{hL_c}{k} \quad (3.3)$$

where L_c is the characteristic length, which equals the length of the vertical and inclined surfaces. For the horizontal surfaces, the characteristic length is defined as

$$L_c = \frac{A_s}{p} \quad (3.4)$$

where p is the perimeter of the surface. However, the Nusselt number also is defined as a function of Grashof, Prandtl, and Rayleigh numbers.

$$Nu = C(Gr \times Pr)^n = CRa^n \quad (3.5)$$

where C and n are coefficients varying depends on the range of Rayleigh number, Gr is Grashof number, Pr is Prandtl number. Since Rayleigh number is a function of Grashof and Prandtl numbers, it is defined as

$$Ra = \frac{g\beta(T_s - T_o)L_c^3}{\vartheta^2} Pr \quad (3.6)$$

where g , β and ϑ indicate gravitational acceleration, coefficient of volume expansion, and kinematic viscosity of the fluid, respectively. However, various Nusselt number equations are given in Table 3.1 depending on the range of Rayleigh number.

Table 3.1. Nusselt number equations depending on the geometry of the surface and Rayleigh number.

Geometry	Rayleigh number range	Equation
Vertical Surface	10^4 - 10^9	$Nu = 0.59Ra^{1/4}$
Vertical Surface	10^9 - 10^{13}	$Nu = 0.1Ra^{1/3}$
Horizontal Plate Upward	10^4 - 10^7	$Nu = 0.54Ra^{1/4}$
Horizontal Plate Upward	10^7 - 10^{11}	$Nu = 0.15Ra^{1/3}$
Horizontal Plate Downward	10^7 - 10^{11}	$Nu = 0.27Ra^{1/4}$

Source: [90]

3.1.1. Radiation Heat Transfer

Radiation heat transfer occurs by the emitted energy that is a reason for the change in the electronic configurations of atoms, which create a form of electromagnetic waves. Therefore, the heat transfer that takes places due to the electromagnetic waves is called as radiation heat transfer. The maximum rate of the heat transfer by radiation can be seen only for a blackbody, which is given by the Stefan-Boltzmann law as

$$\dot{Q}_{rad,max} = \sigma A_s T_s^4 \quad (3.7)$$

where $\dot{Q}_{rad,max}$ is the radiation heat transfer rate, $\sigma = 5.67 \times 10^{-8} W/m^2.K^4$ is the Stefan-Boltzmann constant, A_s is the surface area and T_s is the surface temperature. The surfaces do not behave like a blackbody. Because of this reason, emissivity is defined to make the equation enable for all other surfaces.

$$\dot{Q}_{rad} = \varepsilon \sigma A_s T_s^4 \quad (3.8)$$

where ε is the emissivity value of the surface. The emissivity varies between 0 and 1, and the criteria is that how close the surface is to the emissivity of a blackbody, which is 1. On the other hand, since the surfaces can take a place into gases, such as air, the radiation heat transfer on the surface is defined as

$$\dot{Q}_{rad} = \varepsilon\sigma A_s(T_s^4 - T_{surr}^4) \quad (3.9)$$

where *surr* indicates the surface at absolute temperature separated by a gas, such as air mostly.

3.2. Thermodynamic Analysis

Thermodynamic analyses are performed to obtain the amount of thermal power coming in and going out during the operation of the robot and system. In some methods, it is better to complete thermal analyses first to see that if sufficient cooling or heating power could be produced by the thermal management system. Therefore, this is a significant analysis of the relationship between the amount of heat that produces by the components of the system plus the heat transferring from ambient conditions and the cooling or heating power of the thermal management system.

The amount of maximum cooling or heating powers of a thermal management system that consists of a working fluid to absorb or release the heat are defined as

$$\dot{Q}_{max} = \dot{m}C_p(\Delta T) \quad (3.10)$$

where C_p is the specific heat value of the fluid at a constant pressure, and ΔT is the temperature difference between the working fluid and the applied surface.

3.3. System Modelling

Some of the thermal management methods are applied to the robot theoretically, as taking consideration of ambient conditions and the heat production on electronic components of the robot. Using insulating materials is one of the most common methods that allows arranging heat flux between two surfaces. However, there are some vital properties that have to be taken into consideration. Since the main purpose of an insulating material is to increase the thermal resistance between the surfaces, the low thermal conductivity is one of the main properties. On the other hand, water vapor resistance of the insulating materials should be considered while selecting the suitable material to the system. Furthermore, fire classification of the insulating materials is also a significant feature, because the ideal insulating material for the insulation of the robots has to have a higher fire classification to avoid possible fire detection during the process of the robot. In addition, the weight of the insulating material that will be applied on

the robot also should be taken into consideration, since the lighter thermal management method is always a preferable solution than the heavier ones for robotic applications. Depending on these main features of an ideal insulating material, 19 different insulating materials are analyzed for the robot. Table 3.2 indicates the thermal and physical properties of these insulating materials, while Table 3.3 shows the explanation of fire classification for insulating materials.

Table 3.2. Thermal and physical properties of different insulating materials.

Insulating material	Thermal Conductivity (W/mK)	Water Vapour Resistance Factor	Density (kg/m³)	Fire Classification
Stone Wool	0.033–0.040	1–1.3	40–200	A1–A2–B
Glass Wool	0.031–0.037	1–1.1	15–75	A1–A2
Expanded Polystyrene	0.031–0.038	20–70	15–35	E
Extruded Polystyrene	0.032–0.037	80–150	32–40	E
Phenolic Foam	0.018–0.024	35	40–160	B-C
Polyurethane	0.022–0.040	30–170	15–45	E
Polyisocyanurate	0.018–0.028	55–150	30–45	B
Cellulose	0.037–0.042	1.7–3.0	30–80	B-C-E
Cork	0.037–0.050	5–30	110–170	E
Wood fibers	0.038–0.050	1–5	50–270	E
Mineralized wood fibers	0.060–0.107	5	320–600	B
Hemp fiber	0.038–0.060	1.0–2.0	20–90	E
Kenaf	0.034–0.043	1.2–2.3	30–180	D-E
Sheep wool	0.038–0.054	1.0–3.0	10–25	E
Coir fiber	0.040–0.045	5.0–30	75–125	D-E
Jute fiber	0.038–0.055	1–2	35–100	E
VIP	0.0035–0.008	Up to 340,000	160–230	A1
GFP	0.010 (Krypton) -0.035 (air)	Very high	N.A.	N.A.
Aerogel	0.013–0.015	5.0–5.5	70–150	C

To obtain the heat flux through a surface, total thermal resistance should be defined. Since conduction, convection, and radiation heat transfer mechanisms take place on the surface, the thermal resistance of these mechanisms is defined. Firstly, conduction thermal resistance is the resistance of the surface against heat conduction, which depends on the geometry and thermal properties of the surface. The conduction thermal resistance of a flat surface that is the outer shell of the robot is defined as

$$R_{cond} = \frac{L}{kA} \quad (3.11)$$

where L is the thickness of the surface of the robot, A is the area of the surface of the robot, and k indicates the thermal conductivity of the surface material. However, convection thermal resistance of a surface can be defined by the heat transfer coefficient and surface area, which is

$$R_{conv} = \frac{1}{hA} \quad (3.12)$$

where h is the convection heat transfer coefficient value, which can be defined by a Nusselt number. Thus, convection thermal resistance is the resistance of the surface against heat convection. Furthermore, the radiation thermal resistance can be defined by the radiative heat transfer coefficient and surface area. Therefore, the radiation heat transfer coefficient is defined as

$$h_{rad} = \varepsilon\sigma A_s(T_s^4 - T_{surr}^4)(T_s + T_{surr}) \quad (3.13)$$

Depending on the radiation heat transfer coefficient, the thermal resistance of the surface against radiation is defined as

$$R_{rad} = \frac{1}{h_{rad}A} \quad (3.14)$$

After defining all thermal resistance values of the surface, the total heat transfer can be found by the following equation as

$$\dot{Q}_{total} = \frac{\Delta T}{R_{total}} \quad (3.15)$$

Out of thermal resistance of the insulating materials, another significant parameter of an insulating material is water vapor resistance factor. Water vapor resistance factor is a dimensionless value that indicates the resistance of the surface material against water vapor ingress. However, it is possible to obtain water vapor resistance of the material in MNs/g by multiplying the thickness of the material and dividing by 0.2 g m/MNs which is a value of the vapor permeability of the air. Therefore, the water vapor resistance of the insulating material is defined as

$$WVR = \mu t / 0.2 \left(\frac{g.m}{MNs} \right) \quad (3.16)$$

where μ is the water vapour resistance factor and t is the thickness of the insulating material.

Note that insulating materials are treated as good solutions to reduce the heat flux through the surface as a reason of their low thermal conductivity features. However, another way to reduce the heat transfer through the surface of the robot is the usage of the phase change

materials on the surface. Phase change materials decrease the heat transfer through the surface of the robot by two ways. The first way is similar with the insulating materials, which is the method of increasing the thermal resistance through the surface.

Table 3.3. Fire classification of the insulating materials.

Class	Test Method	Description
A1	EN ISO 1182, EN ISO 1716	$DT \leq 30^{\circ}\text{C}, Dm \leq 50\%$ $t_f = 0 \text{ s}, PCS \leq 2.0 \text{ MJ/kg}$
A2	EN ISO 1182, EN ISO 1716, EN 13823	$DT \leq 50^{\circ}\text{C}, Dm \leq 50\%$ $t_f = 20 \text{ s}, PCS \leq 4.0 \text{ MJ/kg}$ $FIGRA \leq 120 \text{ W s}^{-1}, THR_{600 \text{ s}} \leq 7.5 \text{ MJ}$
B	EN 13823, EN ISO 11925	$THR_{600 \text{ s}} \leq 7.5 \text{ MJ}, Fs \leq 150 \text{ mm in } 60\text{s}$
C	EN 13823, EN ISO 11925	$FIGRA \leq 250 \text{ W s}^{-1}, THR_{600 \text{ s}} \leq 15 \text{ MJ}$
D	EN 13823, EN ISO 11925-2	$FIGRA \leq 750 \text{ W s}^{-1}, Fs \leq 150 \text{ mm in } 60\text{s}$
E	EN ISO 11925-2	$Fs \leq 150 \text{ mm in } 20\text{s}$

Source: [91]

The second way is thermal energy storage, which is one of the main purposes of PCMs. The concept of the PCM packages is illustrated in Figure 3.1. The PCM packs that are placed between the surface of the robot and insulating material decrease the heat transfer rate and store latent heat. During the theoretical study of the PCM concept, the thermal conductivity of the insulating materials is assumed as the approximate thermal conductivity values of the insulating materials that are represented in Table 3.2. The thermal energy storage is a two-stage process, which includes sensible and latent heat transfer. The sensible energy of PCMs is defined as

$$Q_{sensible} = m_{PCM} C_{p,PCM} \Delta T \quad (3.17)$$

where $Q_{sensible}$ is the sensible heat potential of PCMs, m_{PCM} and $C_{p,PCM}$ are the mass and specific heat value of PCMs. However, the latent heat potential of PCMs is defined as the following equation,

$$Q_{latent} = m_{PCM} L_l \quad (3.18)$$

where Q_{latent} is the latent heat potential and L_l is the latent heat of the PCMs. Moreover, Table 3.4 indicates the thermal and physical properties of phase change materials. In Table 3.4, the thermal properties of some of the PCMs are listed.

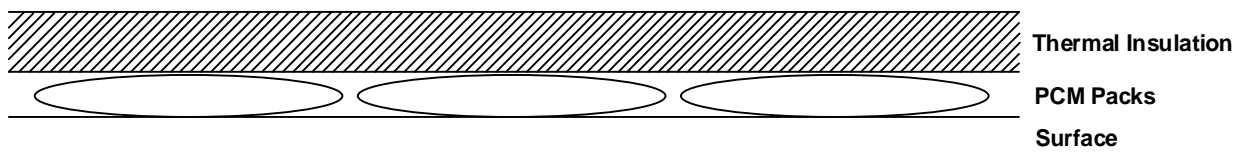


Figure 3.1. The concept of the application of the PCM packages.

Out of passive thermal management methods, active thermal management systems should be considered as well. In this case, air fans are the most common components to achieve a cooling performance on the batteries or robot. However, the performance of a fan is related to the ambient conditions. If the ambient temperature is extremely high, the performance of the fan will not be as effective as its usage at lower temperatures. Furthermore, it is not possible to achieve heating by a fan in cold ambient conditions. Therefore, a new concept of forced air thermal management should be modified.

Table 3.4. Thermal and physical properties of PCMs.

Property	n-octadecane	n-eicosane	n-docosane	n-pentadecane	n-heptadecane	Formic Acid
Specific heat (Solid) (J/kgK)	2150	2150	2150	2225	2300	2151
Specific heat (Liquid) (J/kgK)	2260	2275	2275	2250	2350	2250
Thermal conductivity (solid) (W/mK)	0.358	0.425	0.425	0.265	0.264	0.271
Thermal conductivity (liquid) (W/mK)	0.152	0.152	0.152	0.143	0.142	0.172
Density (solid) (kg/m ³)	814	814	814	785	795	1250
Density (liquid) (kg/m ³)	770	771	771	761	768	1220
Melting Point (°C)	27.07	35.69	44	10	16.7	7.8
Latent heat (kJ/kg)	243.68	247.05	252	205	237	247

Source: Refs. [92,93].

One of the main goals of a thermal management system for mobile robots is to be able to operate in both hot and cold environments. The system should meet the demand of thermal management without making any major adjustment on it. Although forced air cooling can be applied on the hot surfaces, the additional heating system is required to achieve the heating application. Therefore, vortex tubes are effective solutions for air cooling/heating application for thermal management of the electronic components. The vortex tube is a structure that works with compressed gases only. The vortex tube separates the compressed gas into two streams, which are cold and hot streams. The cold stream flows in the middle of the tube, while the hot stream flows by the tube wall. When the high pressured gas enters into the tube tangentially at a high velocity, the injected gas directly pressed towards the inner surface of the tube. As a reason of friction forces of the inner surface of the tube, the gas near the wall heats up. On the other hand, the cold stream is created by the radial expansion on the centerline of the vortex tube.

The forced air thermal management system consists of a battery, DC air compressor, pressure regulator, water separator, and vortex tube. The air compressor is pressured the surrounding air, which is connecting to the pressure regulator and water separator after the compressing process. After the pressure regulator and water separator, compressed air goes into

the vortex tube. One part of the vortex tube produces a cold stream, while the opposite part releases the hot stream at the same time. For the cooling application, the cold air is transferred to the inside of the robot with nozzles, which allow cooling down the components inside. For the heating application at low ambient temperature, the hot stream is given into the robot, while cold air is transferred to the environment.

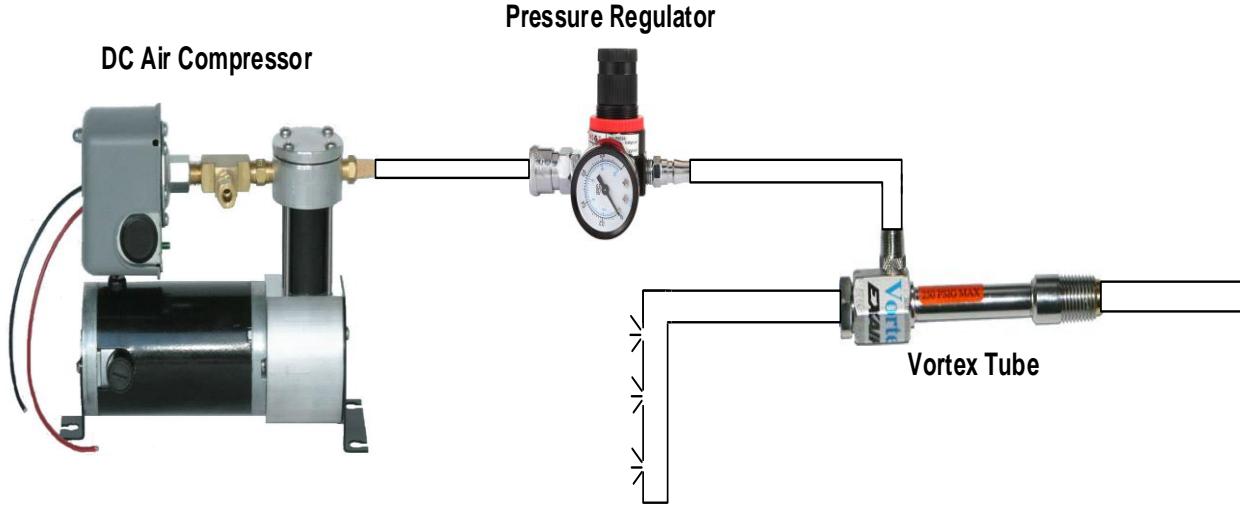


Figure 3.2. The layout of the air cooling thermal management system.

Out of air, the vortex tube can be operated with other gases. However, the most significant criteria for these gases is that the gas should be inflammable against any possible fire during the operation of the robot. On the other hand, an additional storage tank may be required to store the gas to use when it is needed. As it is discussed before, one of the main goals of a thermal management system is that the system should be as light as possible, since it increases the weight load on the robot that directly affects the performance of the robot. Because of this reason, the usage of other gases may not be suitable for every type of mobile research robots. At the same time, it might be a good solution for bigger robotic applications that have more tolerance for extra weight load, or such operations for a short working time. Table 3.5 shows four different inflammable gases that can be used as the working fluid of a vortex tube.

Table 3.5. Physical properties of different gases at 15°C temperature and 6 bar pressure.

Gas	Density (kg/m ³)	Specific Heat (kJ/kgK)
Air	7.304	1.014
Carbon Dioxide	11.02	0.8285
Nitrogen	7.028	1.051
Neon	5.039	1.032

The uncertainty analysis is also investigated for the experimental results in order to confirm the accuracy of the results. The total uncertainty can be written as

$$U_y = \sqrt{\sum_i \left(\frac{\partial y}{\partial x}\right)^2 U_x^2} \quad (3.19)$$

where U is the uncertainty of the element. The experimental uncertainty consists of random and systematic errors as written below.

$$U_i = \sqrt{S_i^2 + R_i^2} \quad (3.20)$$

where S_i is the systematic error and R_i indicates random errors. In addition, the relative standard deviation can be defined as

$$RSD = \frac{s}{\bar{x}} 100\% \quad (3.21)$$

where \bar{x} is the mean of the results.

CHAPTER 4. EXPERIMENTAL APPARATUS AND PROCEDURE

In this section, the experimental setup is introduced for nine different tests, where the relative humidity of the robot and surface temperatures of the robot, motor, and battery are measured. The total experiment consists of three main steps. First, the robot is tested at low temperature with three thermal insulating materials, and an air heating thermal management system to record the temperature data from different points inside of the robot. After that, the temperature values are collected at high temperature with three insulating materials and an air cooling thermal management system. Finally, the robot is tested in the climatic chamber without any thermal protection at high temperature to obtain the temperature distribution on the robot. Figure 4.1 illustrates the main steps of the experimental study.

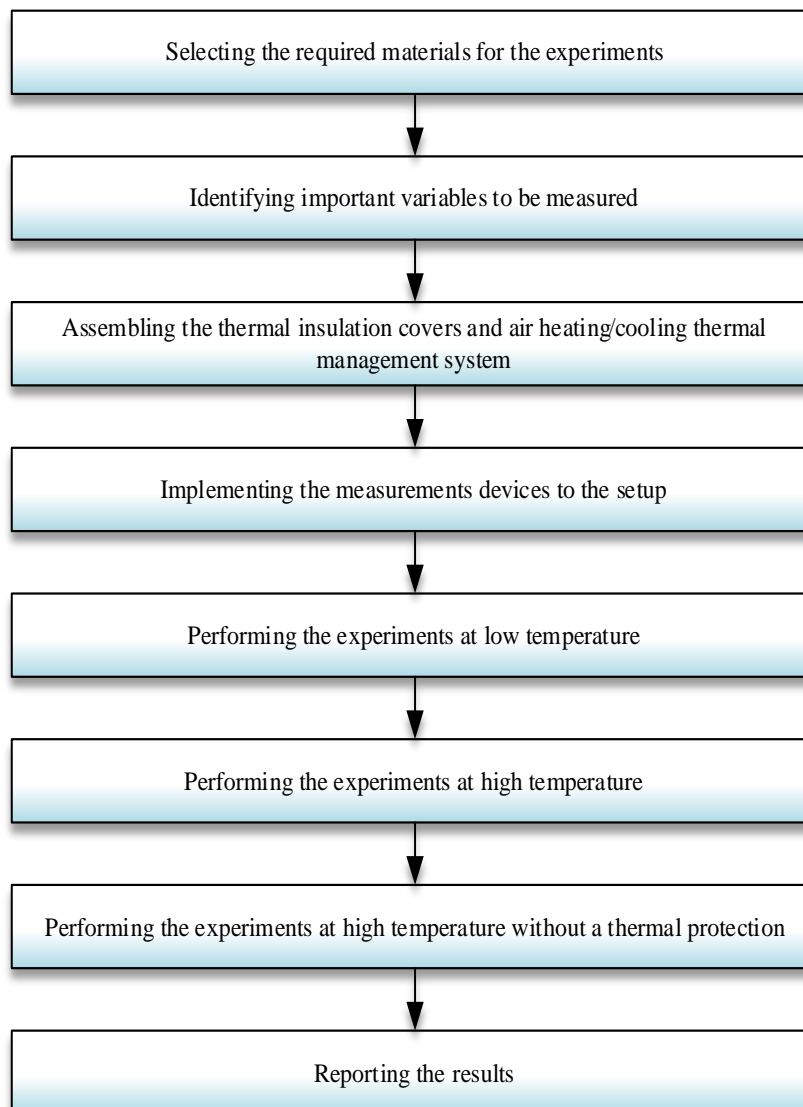


Figure 4.1. The flowchart of the experimental process.

4.1. Thermal Analysis Experimental Setup

During this study, three different insulating materials and air cooling/heating thermal management system are tested in the climatic chamber of ACE Wind Tunnel. The climatic chamber is a chamber in the ACE Wind Tunnel, where the temperature can be adjusted from -40°C to 60°C, and relative humidity also can be controlled between 5% to 95%. The room is adjusted to keep the temperature at -25°C for the low temperature testing, and 40°C for the high temperature tests. Therefore, one of the main challenge during the test is that the duration of the experiment decreases while the temperature difference between the low and high temperatures increases. Because of this reason, the room temperature is kept at -25°C and 40°C for the testing.

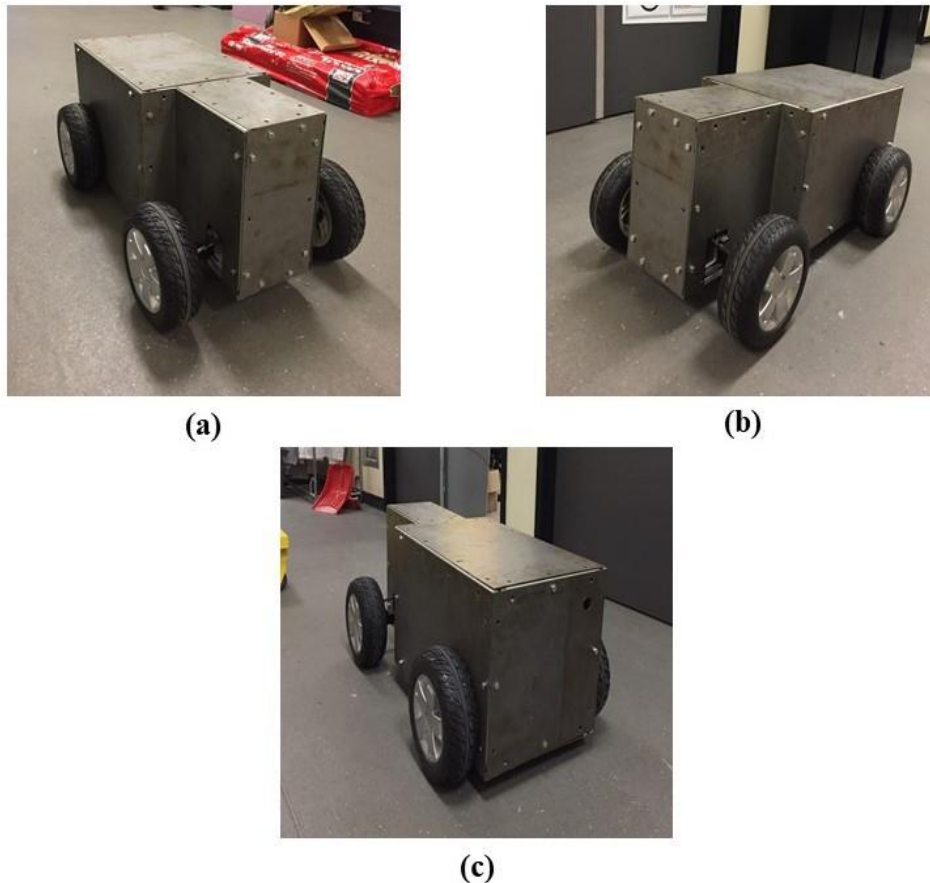


Figure 4.2. The testing robot (a) right view, (b) left view, (c) back view

The experiment is performed on the research robot, in Figure 4.2, that is designed for another project. The main aim of this thermal experimental analysis is to obtain the temperature distributions on the surfaces of the robot, and the surface temperatures of the battery and motor from different locations. Based on these temperature distribution data, the heat transfer rate and performance of the materials are defined. However, the robot should be operated during the test

to obtain a heat generation rate on the battery and motor, which is a more realistic way to test the performance of the materials for thermal management. On the other hand, the controller of the robot is not a remote control, which is connected to the robot with a cable, and it was not possible to stay inside to move the robot during the experiment due to the extreme conditions. The robot has four tires, and only two tires at the back are rotated by the motor. Therefore, the back side of the robot is lifted up and the controller is adjusted to the run position to provide a free rotation for the two tires at the back. In this way, the heat generation rates on the battery and motor are obtained.

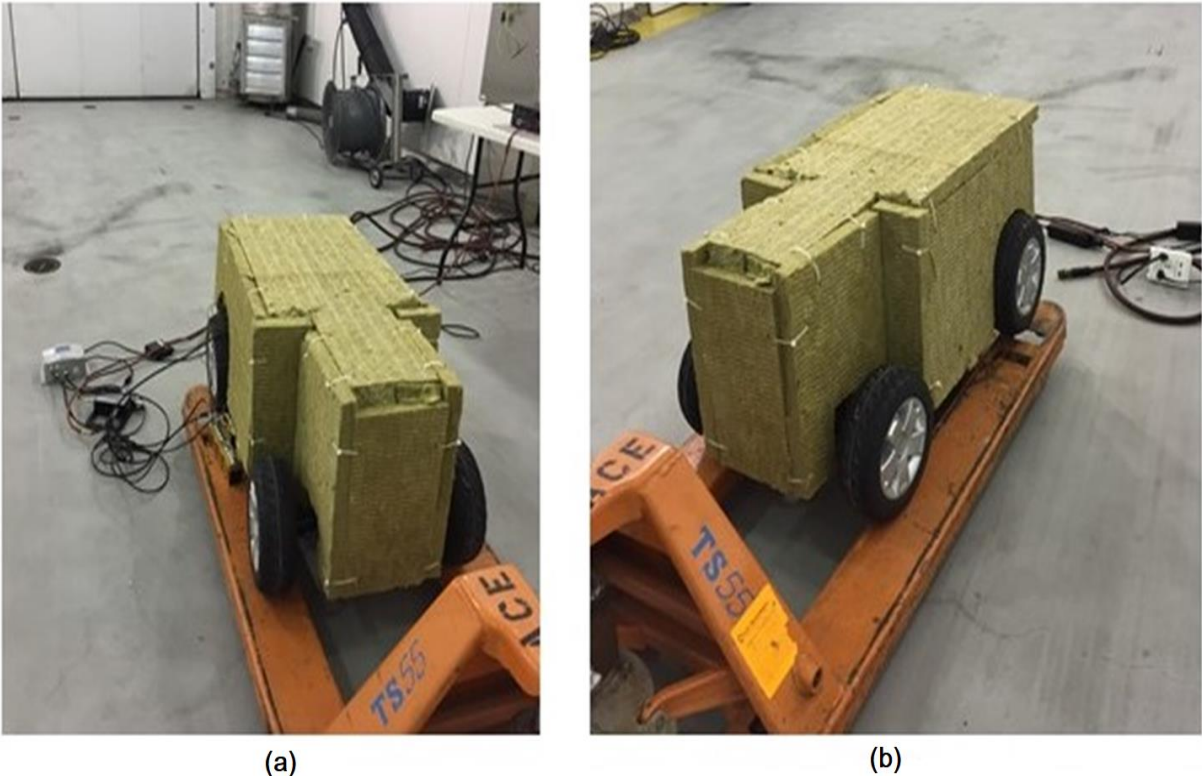
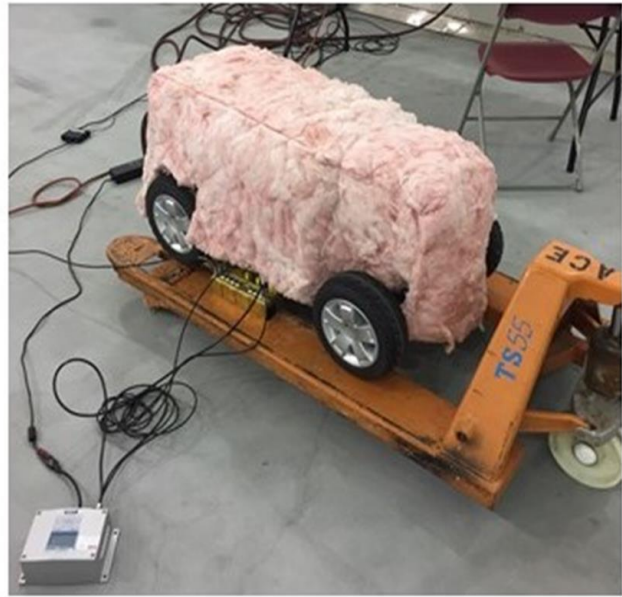


Figure 4.3. The robot with the stone wool cover in the climatic chamber.

The experiment consists of three main parts. First, the robot is tested with the insulating materials and air cooling/heating thermal management system at low temperature. At low temperature, firstly, the stone wool insulating material is tested. After that, fiberglass and extruded polyurethane insulating materials are tested, respectively. Between each test, the robot is kept outside of the chamber to increase the surface temperatures for the following trails. As a last low temperature test, air heating system is operated in the robot that is thermally protected by the fiberglass insulating material.



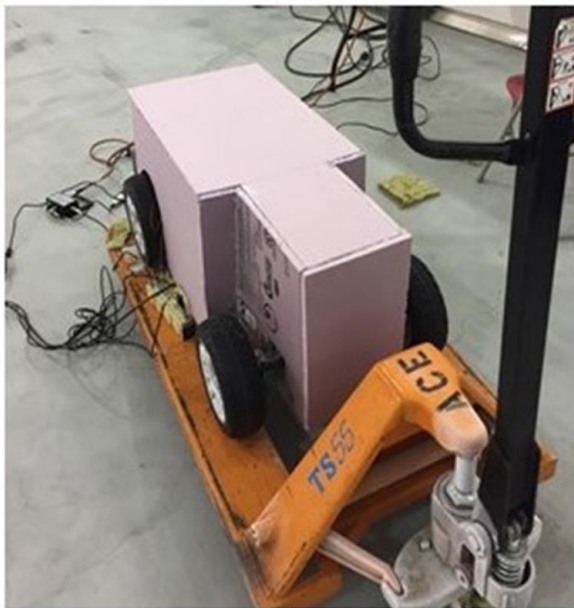
(a)



(b)

Figure 4.4. The robot with the fiberglass cover in the climatic chamber.

After low temperature experiments, the room is heated up from $-25\text{ }^{\circ}\text{C}$ to $40\text{ }^{\circ}\text{C}$ in 3 hours. When the temperature of the climatic chamber reaches to target high temperature, the high temperature experiments take place. In these experiments, the air cooling thermal management system is tested first, and the temperature data from different points of the robot is collected. During the air cooling process, the robot was protected by the fiberglass insulating material again. After that, thermal performances of fiberglass, stone wool, and extruded polyurethane covers are investigated, respectively.



(a)



(b)

Figure 4.5. The robot with the extruded polyurethane cover in the chamber.

Finally, the robot is tested without any thermal protection, meaning that the robot operated at the high temperature without any thermal insulating material or thermal management system. The aim of this last experiment is to see the data of temperature distribution on the robot without any thermal protection.



Figure 4.6. The robot with the air cooling/heating thermal management system and the fiberglass insulating material in the climatic chamber

The temperature data of the robot is collected by the K-type thermocouple cables. The thermocouples are used without a probe to obtain more accurate surface temperature values. Thermocouples are placed on nine different locations, which are shown in Figure 4.7 where the number one is located on the top surface. Four of these thermocouples are placed on the different surfaces of the robot, which are the bottom, top, left side and the right side of the robot. The inside temperature of the robot is measured by the moisture sensor, which is also able to measure the temperature. Two of the thermocouples are located in two different locations on the battery, and the other two of them are connected to the motor. The outer surface of the motor consists of two different materials, which are mainly metal and plastic.



Figure 4.7. The locations of the K type thermocouples.

On the other hand, the data acquisition module is used to record the data during the experiment, which is seen in Figure 4.8. All the data are collected per second in the data service of ACE Wind Tunnel and displayed by Talent Operator Interface software. The software shows the room temperature, humidity and dew point of the room, temperature values of the cooling and the heating system of the room, and temperature and humidity values from the thermocouples and humidity sensor in the robot.



Figure 4.8. Data acquisition module.

4.2. Relative Humidity Analysis Experimental Setup

The relative humidity contents of the inside of the robot and the climatic chamber are recorded during the test. Since each thermal insulating material has a different water vapor resistance value, the relative humidity of the inside of the robot varies. On the other hand, a packet of silica gel is placed in the robot to keep the moisture as possible as low. Since the water content of the air freezes when the ambient temperature is very low, the moisture in the robot should be controlled to avoid any ice formation on the electrical components of the robot. Because of this reason, the desiccant packet is located near the electronic control components and battery, which is shown in Figure 4.9 with the location of the relative humidity sensor that also measures the inside temperature.

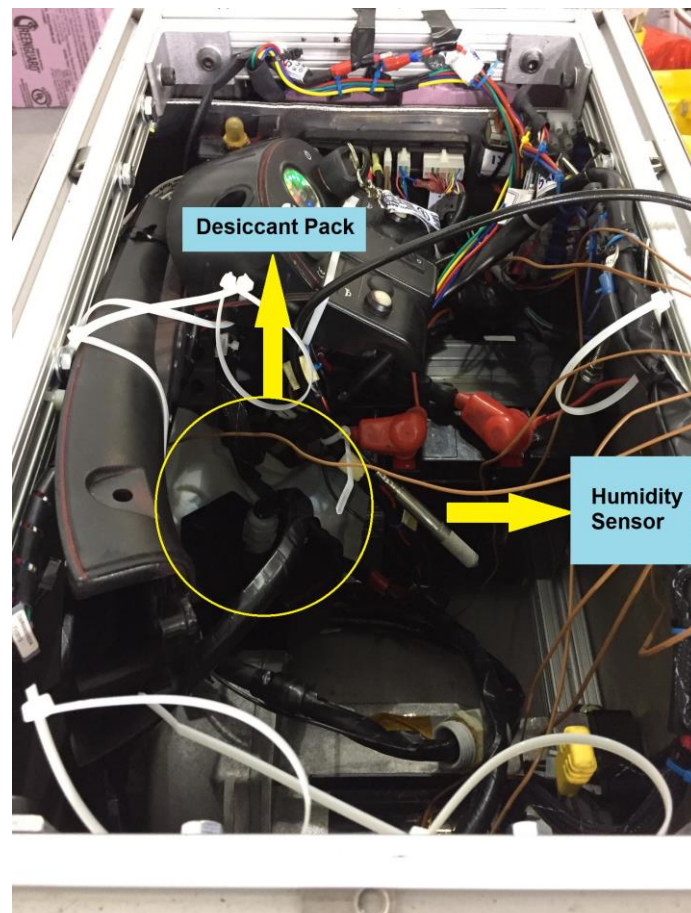


Figure 4.9. The locations of the desiccant pack and the humidity sensor.

CHAPTER 5.RESULTS AND DISCUSSION

In this chapter, the thermal performance of the robot is analyzed theoretically and experimentally with different materials and thermal management methods. Furthermore, their results are discussed in this chapter, which divided into two sections namely theoretical and experimental results.

5.1. Theoretical Results

In this thesis, nineteen different thermal insulating materials, four different phase change materials and an air cooling/heating system are analyzed theoretically.

5.1.1. Insulating Materials Theoretical Results

Insulating materials have a huge range of different varieties. There are different types of thermal insulating materials in the market based on their thermal conductivity value, fire protection classification, water vapor resistance value, thermal and acoustic insulation performance. Because of this huge variety of the thermal insulating materials, nineteen different thermal insulating materials are analyzed in terms of energy and exergy efficiencies, water vapor resistance, heat transfer rate, and total weight at high and low ambient temperatures. However, the effect of the thermal insulating material thickness is analyzed to obtain the change in energy and exergy efficiencies, water vapor resistance value, and heat transfer rate.

In Figure 5.1, heat transfer dissipation rate from the surface of the robot is analyzed. The heat transfer dissipation rate shows the amount of the heat transfer between the inside of the robot and the environment where the robot is operated in. The heat transfer dissipation rate is compared for 19 different thermal insulating materials corresponding to the ambient temperature change from -25 °C to 40 °C. When the temperature difference between the inside of the robot and the ambient condition increases, the heat transfer rate increases as well. However, if this temperature difference decreased, it means that the inside of the robot and the ambient conditions approximate the steady state condition. Therefore, when the system approximates the steady state conditions, the minimum heat transfer rate takes place in the system. This situation can be seen in Figure 5.1, where the heat transfer rate decreases, while the ambient temperature increases from -25°C to 25°C. When the ambient temperature reaches the assumed inside temperature, which is 25°C, the heat transfer rate between the surfaces and reduces just above 50W for all insulating materials.

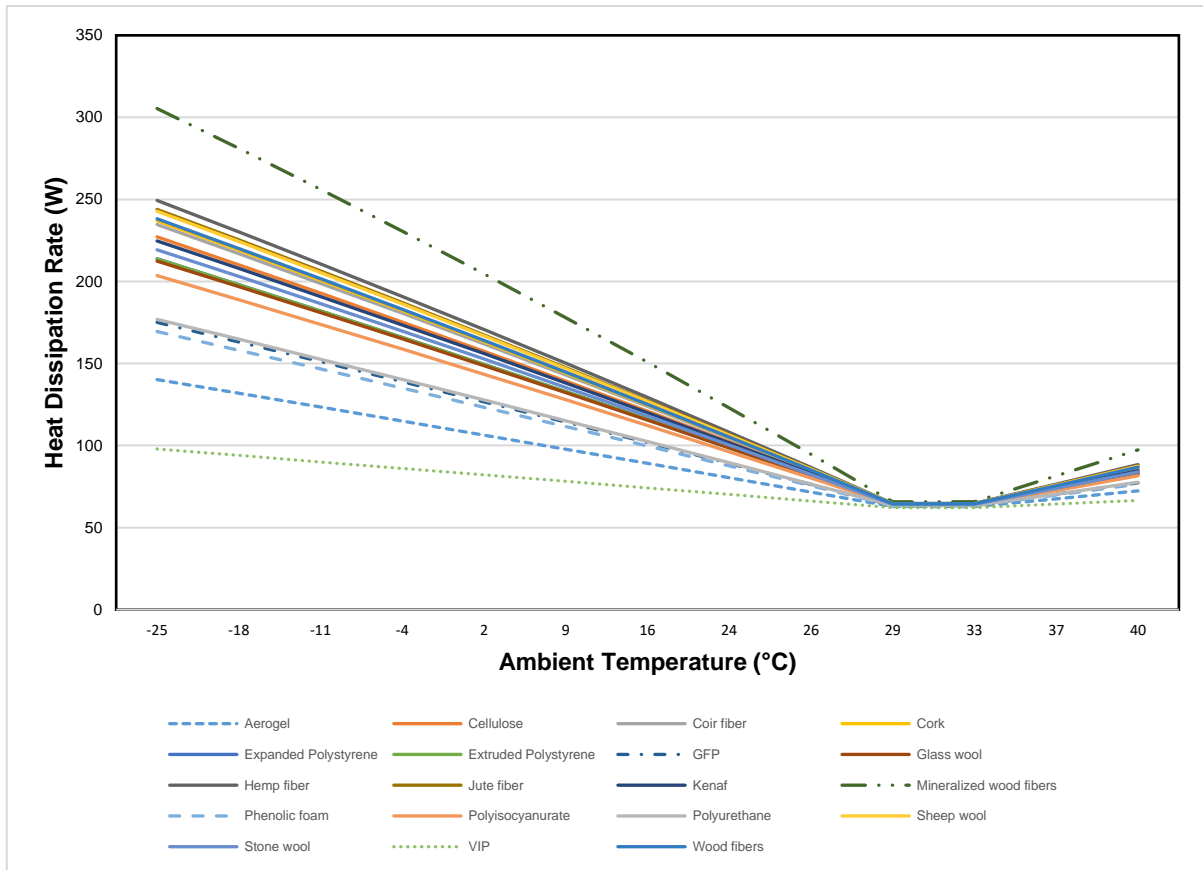


Figure 5.1. The heat transfer rates of different insulating materials corresponding to the change in the ambient temperature.

The high heat transfer dissipation rate indicates that the insulating material has a low thermal performance. Therefore, mineralized wood fibers thermal insulating material has the lowest performance with more than 300W heat transfer when the ambient temperature is 40°C. The heat transfer rates of all the other insulating materials start below 250W. After the mineralized wood fiber, hemp fiber also has one of the highest heat transfer rates with 249.4W at -25°C. The heat transfer rate of the hemp fiber varies between 210.8W and 64.7W, while the temperature increases from -25°C to 25°C. On the other hand, vacuum insulation panels, aerogel blankets, phenolic foam, and polyurethane are the thermal insulating materials that show a high thermal performance in terms of the heat transfer rate between the inside of the robot and the environment. The lowest heat transfer rate at -25°C is obtained by vacuum insulation panels, with 90.04W. There is an almost 43W difference between the heat transfer rates of the vacuum insulation panels and aerogel blankets that have one of the lowest heat transfer rates. On the other hand, the heat transfer rates of phenolic foam and polyurethane are 152.5W and 176.9W. Furthermore, all the other insulating materials, out of the ones that are mentioned, have a heat transfer rate that varies between 200W and 250W.

In Figure 5.1, it can be easily seen that mineralized wood fiber has the lowest thermal performance at high temperature, which is 40°C. Regarding the temperature difference, the heat transfer rate again increases, while the ambient temperature goes up from 25°C to 40°C. However, the vacuum insulation panel has the lowest heat transfer rate at the high temperature, with 70.75W. In addition, aerogel blankets show one of the low heat transfer rates, with 81.83W at high-temperature conditions. Since the heat transfer rate has a linear relation with the increase in temperature, the heat transfer rate rises when the ambient temperature goes up from 25°C to 40°C.

On the other hand, it is also significant to mention the heat transfer rate of the insulating materials that are used for the experimental study of this thesis. The heat transfer rate of the stone wool thermal insulating material is 186.8W at -25°C and decreases to 64.17W at 25°C. After that, when the ambient temperature reaches 40°C, the heat transfer rate increases to 169.7W. However, the thermal performance of the glass wool and extruded polyurethane thermal insulating materials are obtained as better than the stone wool insulating material. At -25°C, the heat transfer dissipation rates of the fiberglass and extruded polyurethane are 182.4W and 181.8W, respectively. Furthermore, the heat transfer rates of these two thermal insulating materials reach 102W for the fiberglass and 101.9W for the extruded polyurethane at 40°C.

For each thermal insulating materials, the energy efficiency is defined corresponding to the change in temperature of the ambient conditions, which is shown in Figure 5.2. As a result of a low heat transfer rate, some of the insulating materials have higher energy efficiency values than others. These insulating materials are vacuum insulation panels, aerogel blankets, phenolic foam, polyurethane, polyisocyanurate, gas-filled panels, fiberglass and extruded polyurethane. The highest energy efficiency can be seen for the vacuum insulation panel (VIP), with 77.79% at -25 °C and 77.08% at 40 °C. However, the energy efficiency decreases to 10.27%, while the ambient temperature reaches 25°C. Because of the low heat transfer rate between the inside of the robot and the ambient conditions, the energy efficiency decreases when the ambient temperature increases from -25°C to 25°C, and after that increases when the ambient temperature reaches to 40°C. There is no doubt that, the heat transfer rate and the energy efficiency values are high when the ambient temperature is -25°C, comparing to 40°C ambient temperature, because of the larger temperature difference between the assumed inside temperature of the robot and the outside.

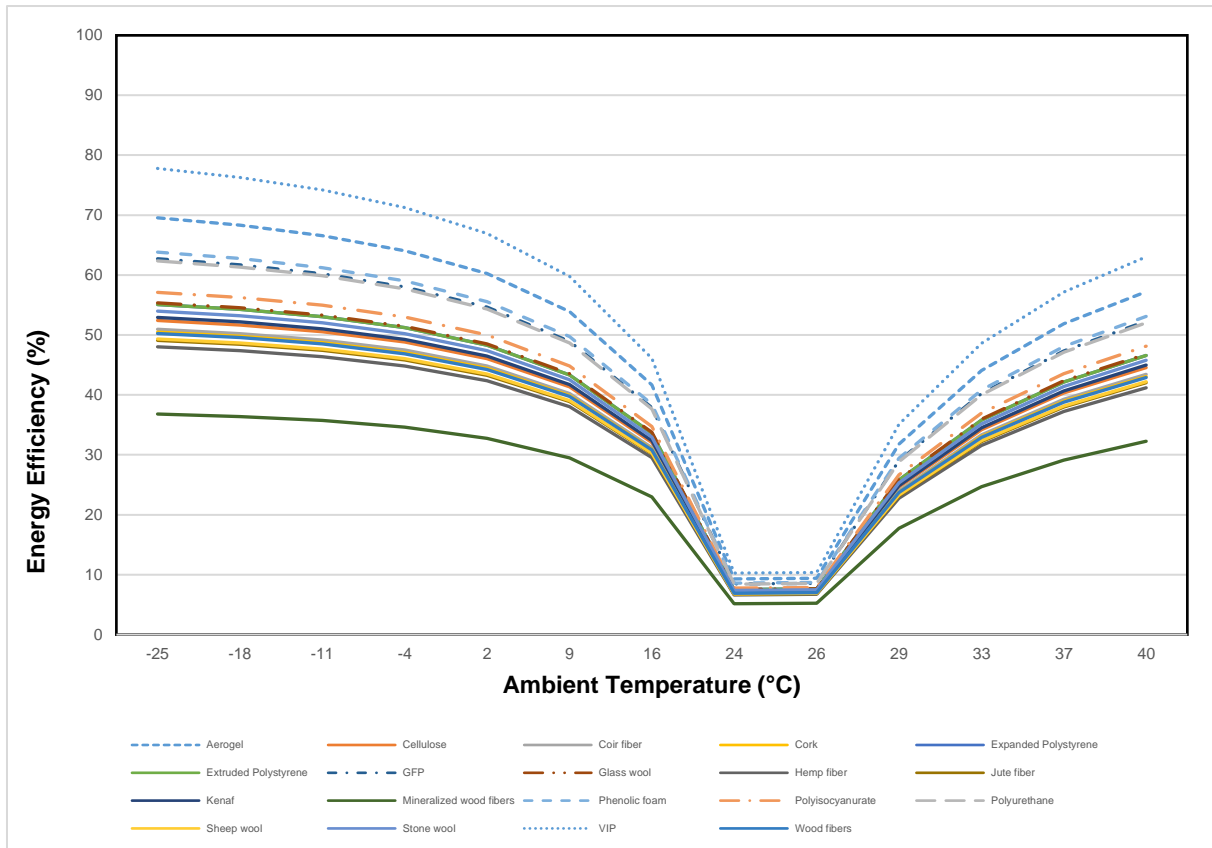


Figure 5.2. The energy efficiencies of different insulating materials corresponding to the change in the ambient temperature.

Aerogel blankets also provide high energy efficiency at both low and high temperatures. The energy efficiency of the aerogel blankets changes between 69.55% and 57.34% at low and high temperatures, respectively. However, phenolic foam, gas-filled panel, and polyurethane have also high energy efficiency values, with 63.82%, 62.72%, and 62.36% at -25°C, respectively. On the other hand, their energy efficiency values at 40°C are obtained as 53.1% for phenolic foam, 52.28% for gas-filled panel, and 52.02% for polyurethane.

Figure 5.2 also indicates the energy efficiency values of the insulating materials that are used during the experiment. One of these insulating materials is stone wool, and its energy efficiency changes between 53.98% and 7.33% from -25°C to 25°C. When the temperature increases to 40°C, the energy efficiency of the stone wool thermal insulating material rises up to 45.77%. These energy efficiency values for the stone wool insulating material are lower than the energy efficiencies of the other two thermal insulating materials that took place in the experiment. However, the energy efficiencies of the fiberglass material varies between 55.36% and 7.54%, while the ambient temperature increases from -25°C to 25°C. After that, the energy efficiency reaches 46.81%, when the ambient temperature increased to 40°C. Finally, the extruded polyurethane thermal insulating material provides 55.08% energy efficiency at -25°C,

which decreases to 7.51% when the ambient temperature is approximately 25°C. On the other hand, the energy efficiency of the extruded polyurethane increases to 57.58% with the change in the ambient temperature.

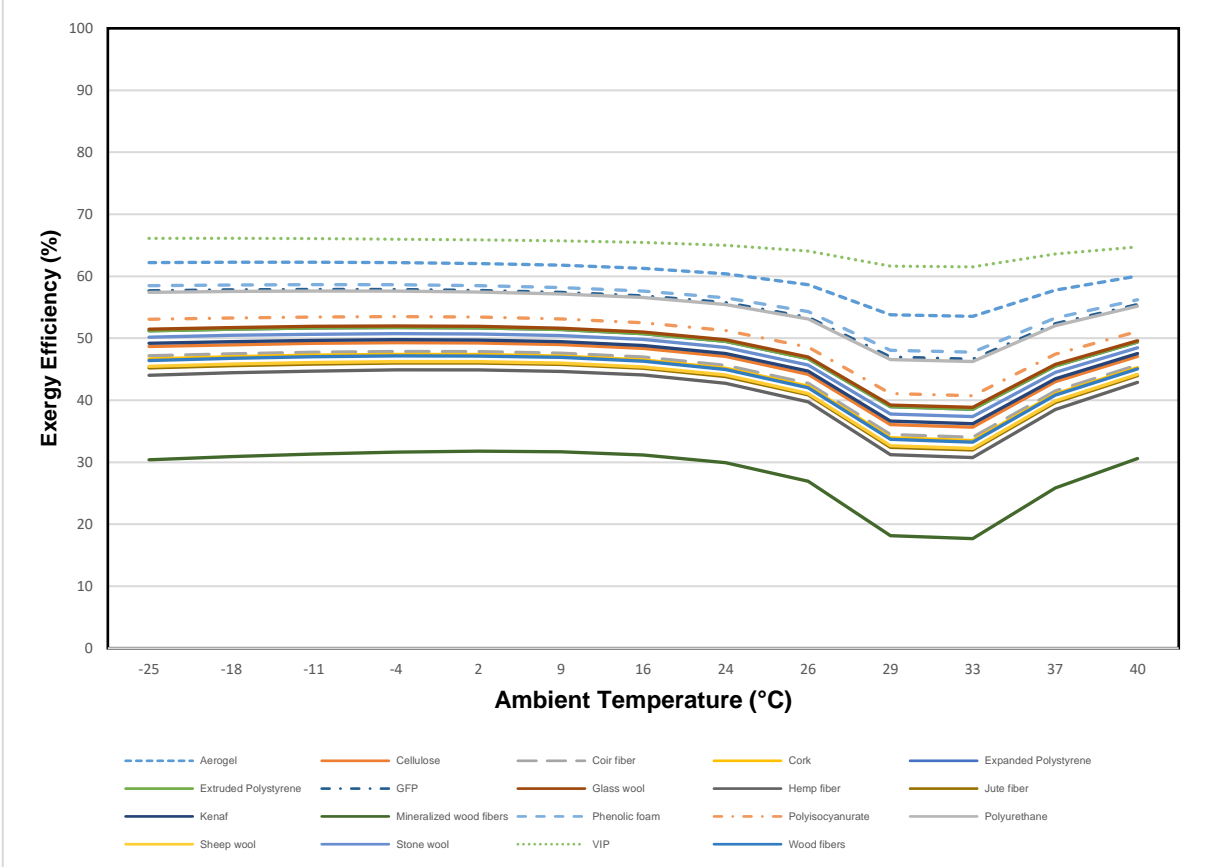


Figure 5.3. The energy efficiencies of different insulating materials corresponding to the change in the ambient temperature.

On the other hand, the effect of the ambient temperature on the exergy efficiencies of various thermal insulating materials is analyzed and demonstrated in Figure 5.3. The exergy efficiency of the thermal insulating materials is another significant parameter that should be taken into consideration while the design of the thermal insulation on a robot. The exergy analysis indicates the performance of the material to the reference of the ambient conditions. Therefore, the temperature difference between the ambient conditions and the surface of the robot has a highly significant effect to compare different thermal insulating materials. In Figure 5.3, it can be easily seen that the vacuum insulation panels have the highest rate of exergy efficiency corresponding to the temperature change of the ambient conditions. The exergy efficiency of the vacuum insulation panel changes between 66.12% and 65.85%, while the ambient temperature varies from -25°C and 40°C. However, aerogel, phenolic foam, polyurethane and gas-filled panels also have good exergy performance, with the exergy efficiencies of 62.27%, 58.66%, 57.62%, and 57.88%, at low temperature respectively. On the

other hand, the exergy efficiency of the stone wool decreases from 50.19% to 37.77% when the temperature changes from -25°C to 40°C, however, increases to 57.07% when the ambient temperature reaches to 40°C. Finally, the exergy efficiency of the fiberglass changes between 51.49% and 39.25%, from -25°C to 40°C, and rises to 57.94% at 40°C.

Another study for the thermal insulating material is performed to estimate the significant effect of the thickness of the thermal insulating materials on the heat dissipation rate, energy and exergy efficiencies. Nineteen of different thermal insulating materials are analyzed while the thickness of the material varies between 10 mm and 300 mm. Since the thermal performance of the materials is affected by the ambient temperature, the analyses are completed into two sections. First, the heat dissipation rate, energy and exergy efficiencies of these insulating materials are analyzed at low temperature, and after that, they are also analyzed at a high temperature, while the thickness of the material increases.

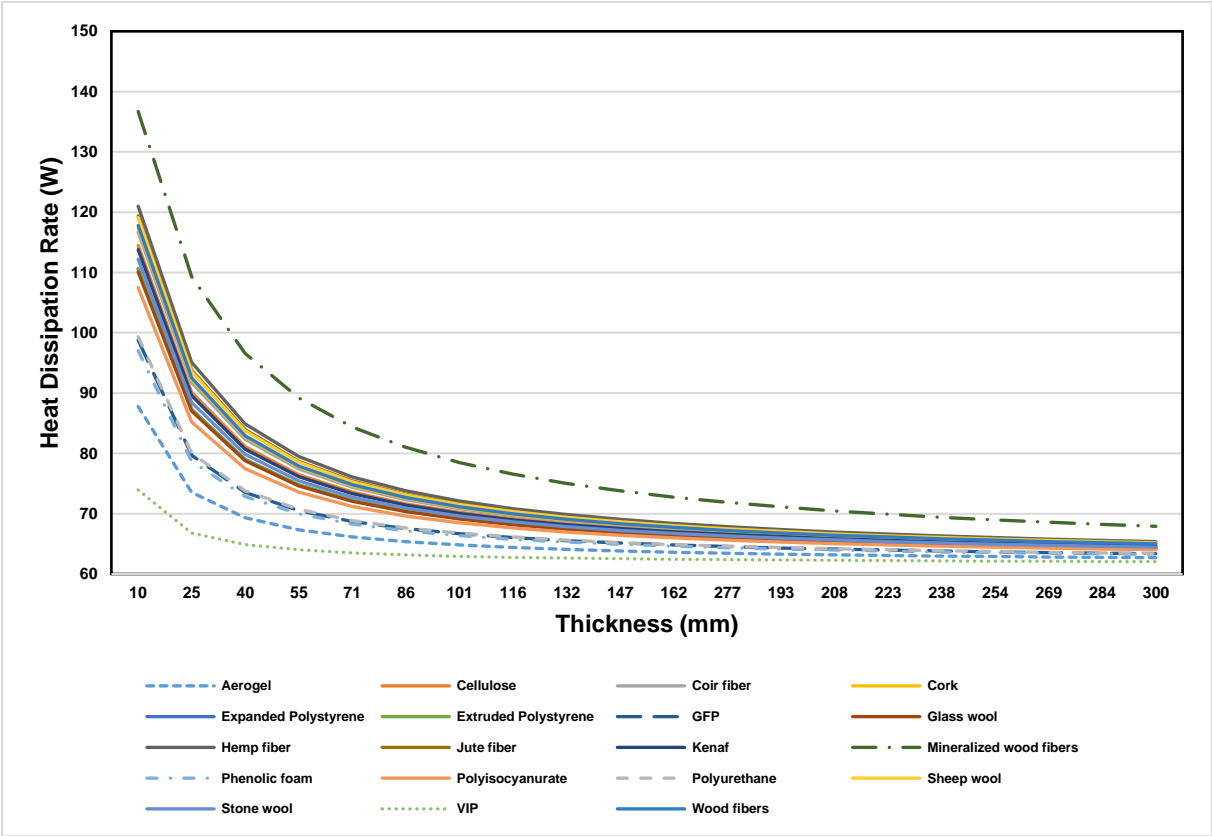


Figure 5.4. The heat transfer rates of different insulating materials corresponding to the change in the thickness at high temperature.

Figure 5.4 indicates the variation of the heat transfer rate corresponding to the change in the thickness of the insulating material at the high temperature (40°C). The insulating material, which has the highest rate of heat transfer between the outside and inside of the robot, has the lowest thermal performance. There is no doubt that mineralized wood fiber thermal

insulating materials have the lowest thermal performance corresponding to the change in the thickness, with 136.7W when the thickness is 10mm. However, the best performance can be seen for vacuum insulation panels, with the heat transfer rate of 73.94W. With 10 mm of insulation thickness, aerogel blankets, phenolic foam, gas-filled panel and polyurethane, and stone wool also have good thermal performances.

It is also significant to mention that after a certain value of the thermal insulation thickness, the heat transfer rate of the insulating materials approximates the range between 63W and 65W. Although the thickness of the material increases, the heat transfer rate stays constant after a specific thickness value. This situation shows the importance of the analyzing the insulation thickness before designing a thermal insulation protection on a robot to avoid the extra weight on the robot. However, it is also significant in terms of the cost of the insulation process. This critical thickness of the thermal insulating materials for this particular study can be defined as around 235mm for all them.

In addition, the performance of the insulating materials that are analyzed during the experiment should be investigated. The stone wool insulating material has 112.2W heat transfer rate when the thickness of the material is 10 mm. However, it decreases to 64.44W with the increase of the thickness. On the other hand, the heat transfer rate of the fiberglass thermal insulating material can be seen as 110.1W with 10mm of insulation thickness, and it reduces to 64.25W corresponding to the increase of the thickness from 10mm to 300mm. Finally, extruded polyurethane transfers 110.6W heat from outside to the inside of the robot when the thickness is 10 mm, but this rate decreases to 64.29 W while the thickness reaches 300mm.

The effect of the thickness of the thermal insulating material on the energy efficiency of the materials is analyzed in Figure 5.5. Since the heat transfer rate of the insulating material stays constant after a certain thickness, the energy efficiency increases very slightly after the same thickness value. Vacuum insulation panels have the highest energy efficiency, changing between 59.39% and 65.92%. Furthermore, aerogel, gas-filled panels, and polyurethane thermal insulations perform with high energy efficiency values, 51.78%, 45.75%, and 45.44%, respectively. On the other hand, the energy efficiency of the stone wool thermal insulating material increases from 38.38% to 64.61%, while the thickness changes between 10 mm and 300mm. The fiberglass material has 39.52% energy efficiency when the insulation thickness is 10mm, but the energy efficiency rises 64.71 % with 300 mm insulation thickness. The energy efficiency of the extruded polyurethane material varies between 39.28% and 64.69%.

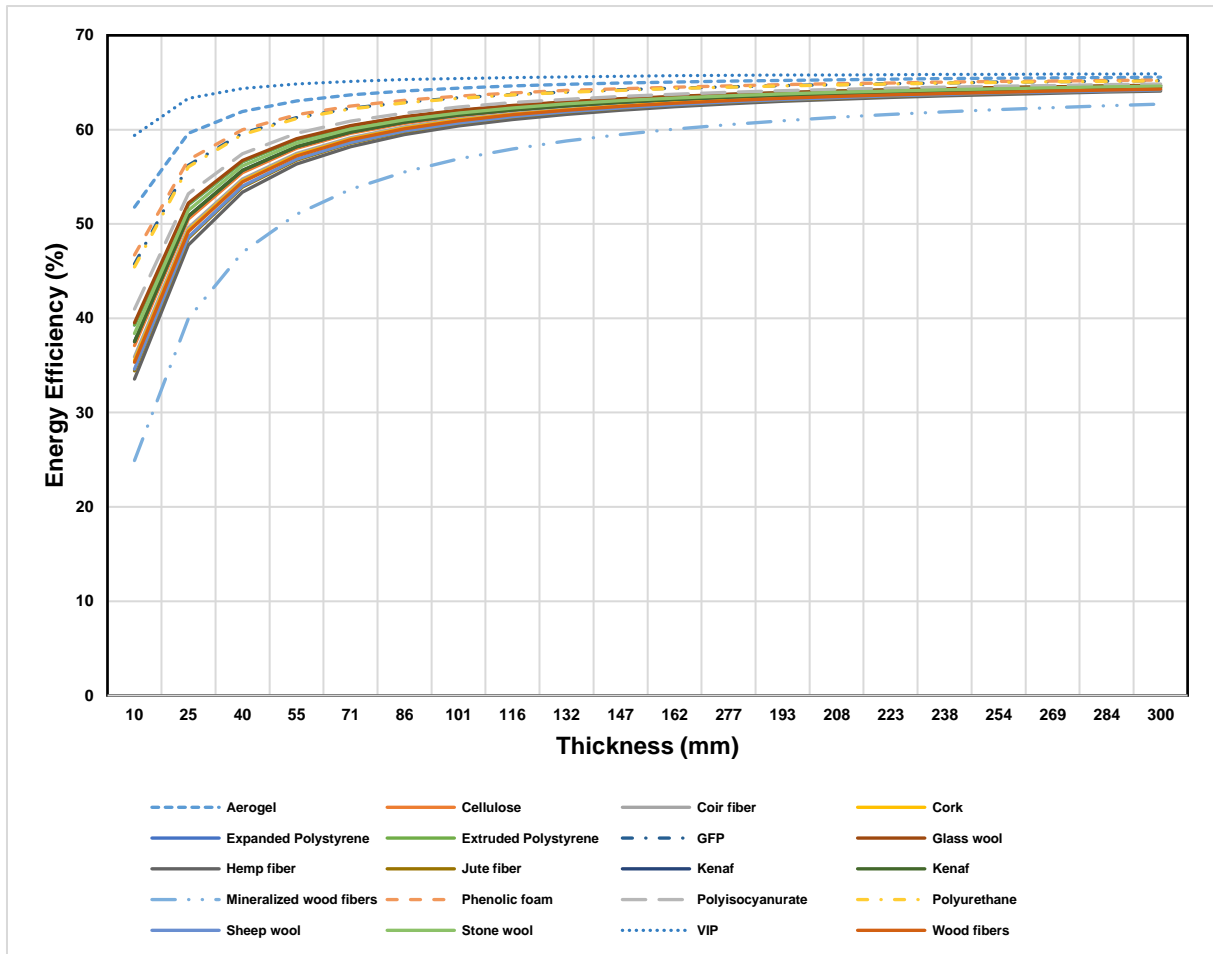


Figure 5.5. The energy efficiencies of different insulating materials corresponding to the change in the thickness at high temperature.

Figure 5.6 compares various thermal insulating materials in terms of the change in their exergy efficiencies corresponding to different insulation thicknesses. There is no doubt that the mineralized wood fibers have low exergy efficiencies, which are 20.72% when the thickness is 10 mm, and 62.38% with 300 mm insulation thickness. On the other hand, the exergy efficiency of the vacuum insulation panels varies between 60.52% and 63.89%. It also should be mentioned that the exergy efficiencies of all the materials stay almost constant, after a specific thickness value corresponding to the nearly constant heat transfer rate. From the exergy efficiency point of view, it is also clear that increasing the insulation thickness does not rise the thermal performance of the material. However, the exergy efficiency of the stone wool thermal insulating material changes between 41.02% and 63.31% with the increase of the thickness. Comparing to the stone wool, the exergy efficiency of the fiberglass insulating material increases from 42.44% to 63.36%, while the exergy efficiency of the polyurethane varies between 49.12% and 63.57%.

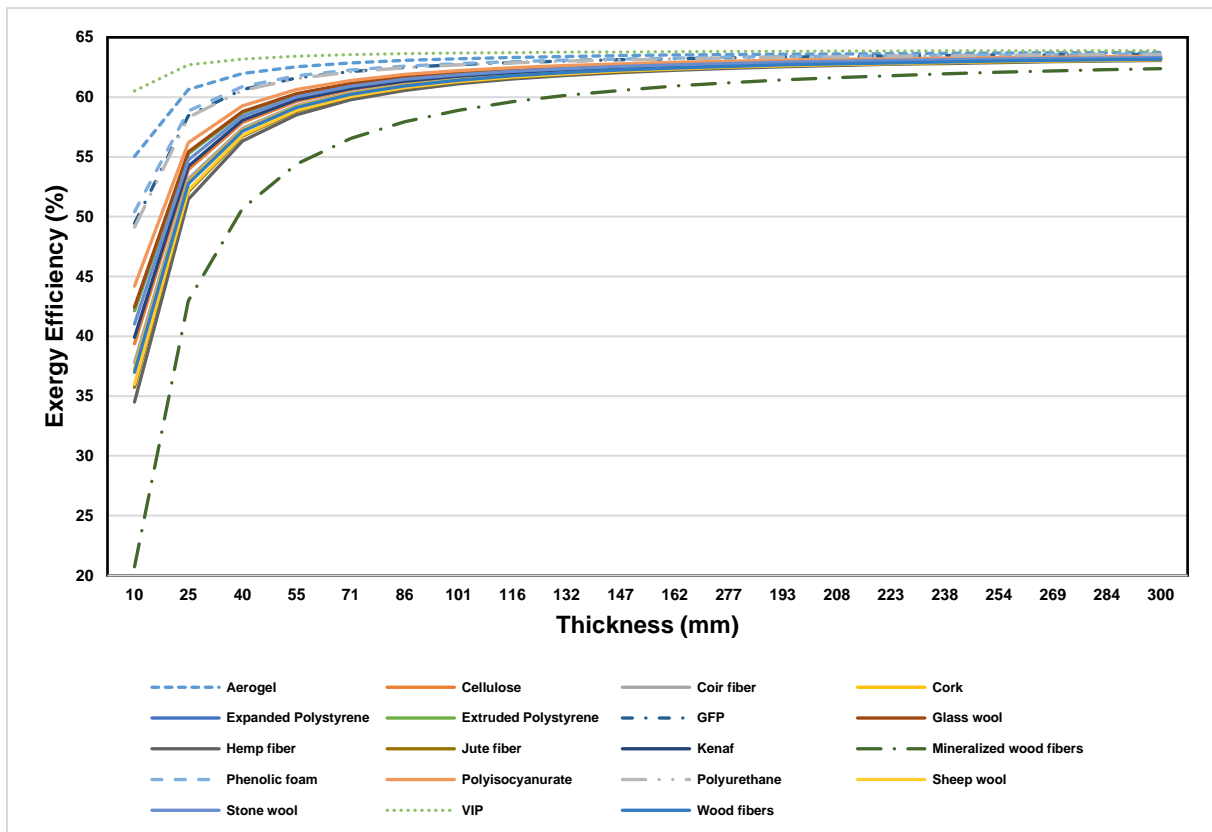


Figure 5.6. The exergy efficiencies of different insulating materials corresponding to the change in the thickness at high temperature.

The effect of the insulation thickness on the thermal performance of the robot should be analyzed at a low ambient temperature as well. Therefore, Figure 5.7 demonstrates that the heat transfer rate between the inside and the outside of the robot decreases dramatically, while the thickness of the insulation increases from 10 mm to 300 mm. Mineralized wood and hemp fibers thermal insulating materials have the highest rate of heat transfers, which are 345.5 W and 292 W with 10 mm thickness, respectively. On the other hand, vacuum insulation panels, aerogel, phenolic foam are the insulating materials that have lower heat transfer with the 10 mm insulation thicknesses. The heat transfer rate of the vacuum insulation panels is 113.8 W and decreases to 68.73W as a reason of the increase of the insulation thickness. In Figure 5.7, it can be seen that the heat transfer rate decreases gradually with the change in the thickness of the insulating material because the thermal resistance of the insulating material increases. Therefore, there is no doubt that, the heat transfer rate can be easily reduced by increasing the insulation thickness. However, Figure 5.7 indicates that the effect of insulation thickness on the heat transfer rate decreases after a certain thickness value, and the heat transfer rate of these thermal insulating materials reaches approximately 75 W with an insulation thickness of 300 mm.

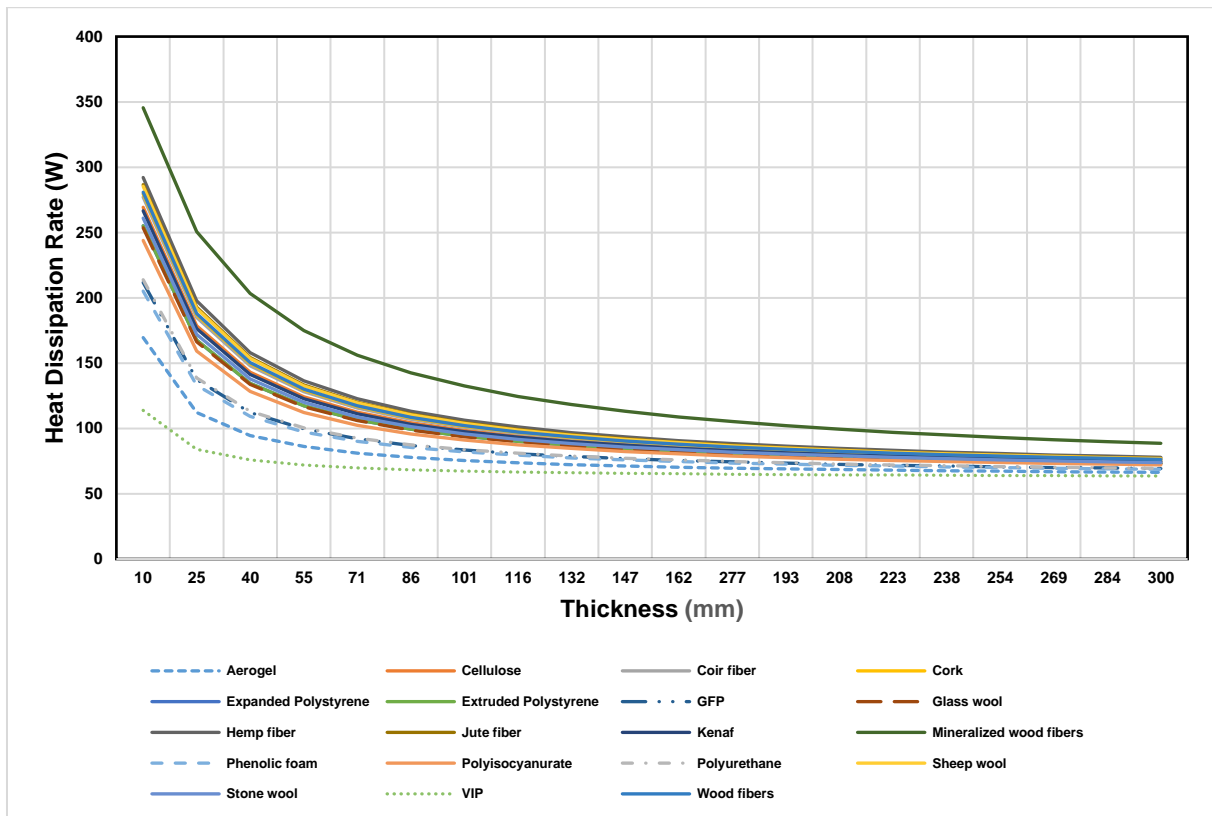


Figure 5.7. The heat transfer rates of different insulating materials corresponding to the change in the thickness at low temperature.

In addition, the heat transfer rate of the stone wool thermal insulating material is 261 W with the 10 mm insulation thickness and decreases to 73.84 W with the increase of the insulation thickness. On the other hand, fiberglass insulating material has a better thermal performance, which varies between 253.6 W and 73.02 W. Finally, the energy efficiency of extruded polyurethane material decreases from 255.1W to 73.18W, while the thickness changes between 10mm and 300mm.

From the energy efficiency point of view, the thermal performance of the insulating materials is showed in Figure 5.8. The energy efficiency of the vacuum insulation panels varies between 76.57% and 86.91%, which are the highest energy efficiencies. On the other hand, the lowest energy efficiency value is obtained by mineralized wood fibers, with 28.83 % at 10 mm insulation thickness. As a reason of their low heat transfer rates, aerogel, phenolic foam and gas-filled panels also have high energy efficiency values. It is also important that the energy efficiency stays constant after a certain insulation thickness value, which is directly related to the heat transfer rates of the thermal insulating materials.

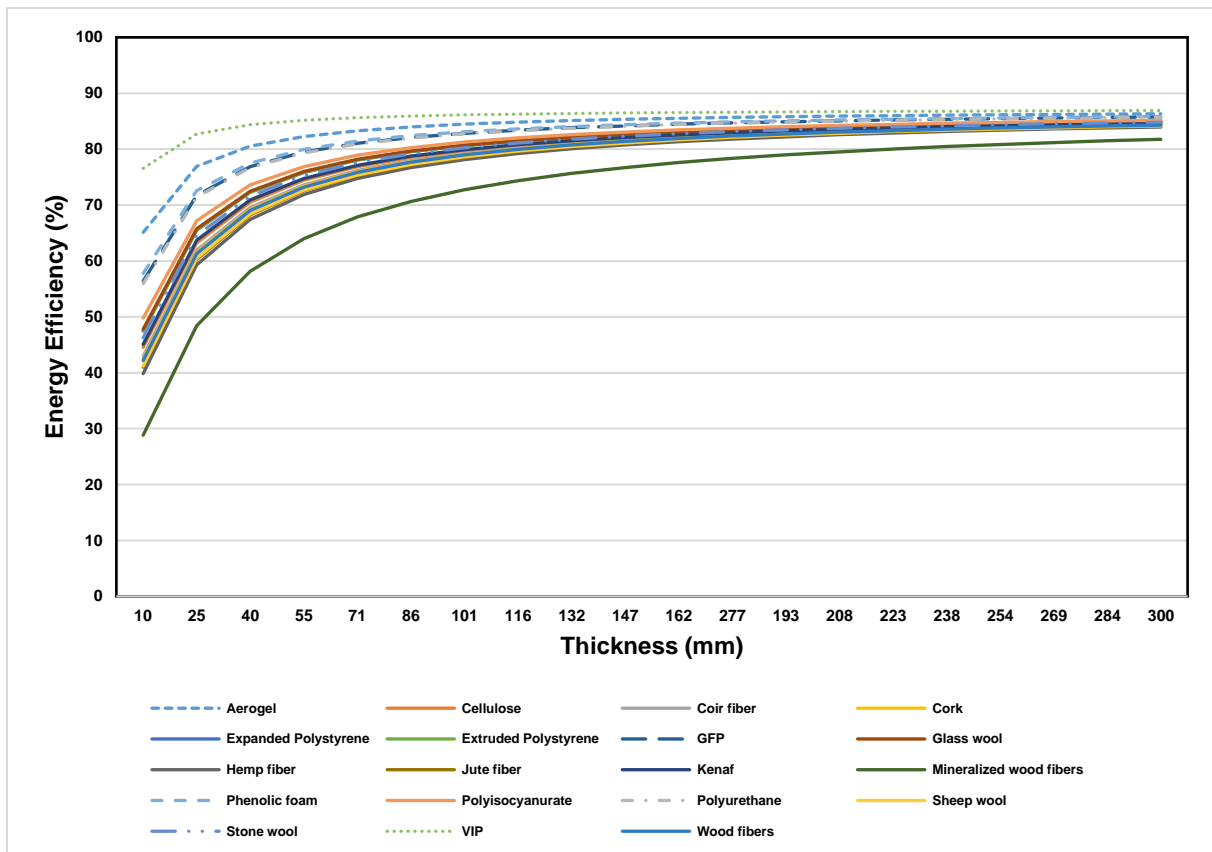


Figure 5.8. The energy efficiencies of different insulating materials corresponding to the change in the thickness at low temperature.

Furthermore, the energy efficiency of the stone wool increases from 46.25% to 84.79%, while the thickness rises to 300 mm from 10 mm. On the other hand, fiberglass has a better thermal performance, comparing to stone wool and extruded polyurethane. The energy efficiency of the fiberglass thermal insulating material is 47.78% when the insulation thickness is 10 mm. However, the efficiency increases to 84.96% when the insulation thickness is 300 mm. Finally, the energy efficiency of the extruded polyurethane material rises from 47.47% to 84.93%.

On the other hand, Figure 5.9 shows the exergy efficiency of various thermal insulating materials corresponding to the change in the insulation thickness at low temperature. The highest exergy efficiency is obtained for the vacuum insulation panel, which changes between 66.88% and 69.93% while the insulation thickness rises from 10 mm to 300 mm. However, the exergy efficiency of the stone wool insulating material increases from 43.44% to 69.52%. The increase of the exergy efficiency of the fiberglass can be seen as from 45.13% and 69.56%. Moreover, the exergy efficiency of the polyurethane goes up from 53.23% to 69.71%. Furthermore, it can be easily indicated that the exergy efficiencies of the materials reach the similar percentages when the thickness is 300 mm.

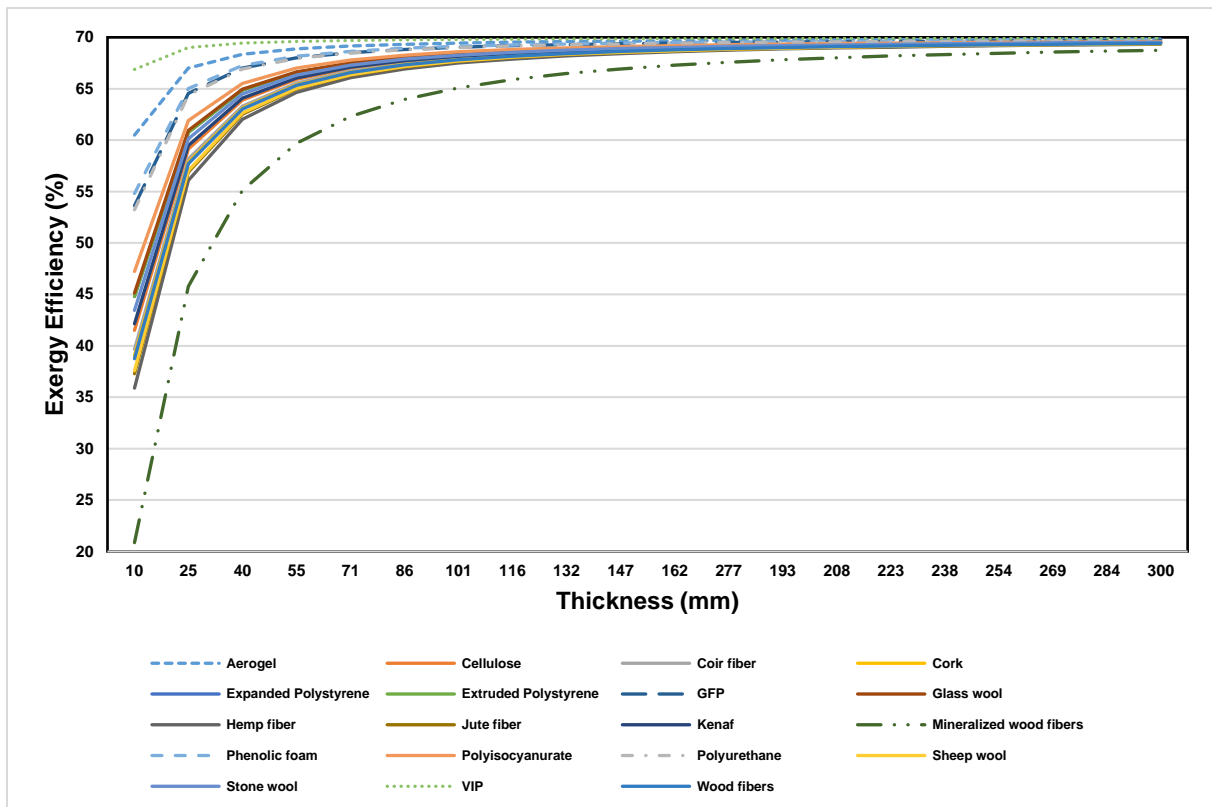


Figure 5.9. The exergy efficiencies of different insulating materials corresponding to the change in the thickness at low temperature.

Out of the thermal performance of the insulating materials, there are two more significant parameters that should be taken into consideration during the design process of a thermal insulation protection cover on a mobile robot. One of them is the weight of the insulation that will be applied to the robot. Since the mobile research robots are the electrical and mechanical structures that can move in the operation area, the amount of extra weight on the robot has a key role in the performance of the robot. Furthermore, the extra weight on the robot rises the load on the battery and motor, which is a reason of temperature increase on these two components of the robot. Figure 5.10 compares different thermal insulating materials in terms of their weights when the insulation thickness is 55 mm. On the other hand, water vapor resistance is the other important parameter of the insulating materials. The water vapor resistance of an insulating material is a parameter that varies with a change in the insulation thickness. Therefore, Figure 5.11 shows the variation of the water vapor resistance of different insulating materials for different thicknesses.

In Figure 5.10, the weights of various thermal insulating materials are compared each other when the insulation thickness is 55 mm. As an organic thermal insulating material, the sheep wool is the most lightweight thermal insulating material.

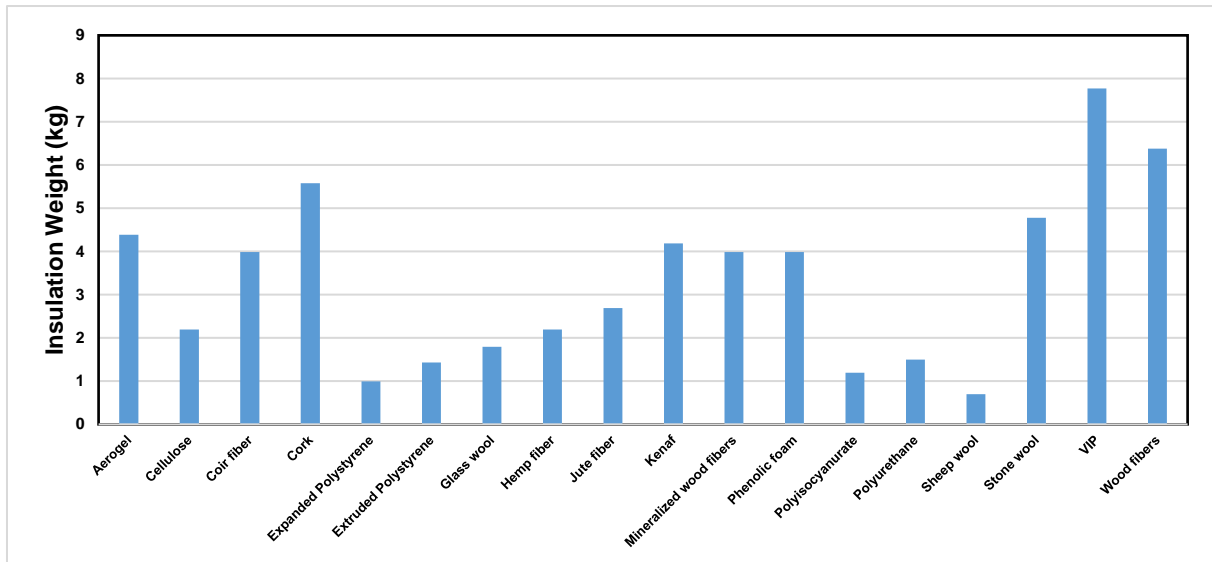


Figure 5.10. The comparison of various insulating materials in terms of their weight.

The total weight of the sheep wool is only 0.69kg with the 55mm of insulation thickness. Another lightweight thermal insulating material is the expanded polystyrene. The total weight of the expanded polystyrene on the robot is almost 1 kg. After these two lightweight thermal insulating materials, it also should be mentioned that extruded polyurethane, polyisocyanurate, polyurethane, fiberglass have a remarkable amount of weight on the robot. Although vacuum insulation panels have a better thermal performance than other materials, the weight of this material, which is 7.77 kg, is higher than others. In addition, wood fibers, cork, coir fiber and stone wool are also heavy thermal insulating materials. The weight of fiberglass insulating material is 1.7 kg with the thickness of 55 mm. On the other hand, the extruded polyurethane materials are slightly more lightweight than fiberglass. The total weight of the extruded polyurethane is estimated as 1.4 kg when the thermal insulating material thickness is 55 mm.

The water vapor resistance of an insulating material should be as possible as higher to be able to be used for robot thermal protection operations. If the robot is not protected against ingress of water, an insulating material that has a high water vapor resistance value should be applied to the robot. In terms of the insulation thickness variations, Figure 5.11 compares the water vapor resistance values of different insulating materials. It can be easily seen that extruded polyurethane is the thermal insulating material that has the highest water vapor resistance. The water vapor resistance value of this material varies between 5.75 MNs/g and 172.5 MNs/g, while the insulation thickness increases from 10 mm to 300 mm. Polyurethane is another thermal insulating material that has a high water vapor resistance, which increases from 5.12 MNs/g to 153.8 MNs/g. In addition, polyisocyanurate is also one of the thermal insulating materials with a high water vapor resistance. The water vapor resistance of polyisocyanurate

changes between 5 MNs/g and 150 MNs/g. However, these three thermal insulating materials, which have higher water vapor resistance, are formed as an organic chemistry structure. Because of the non-porous structure of these materials, their water vapor resistance value is higher, comparing to another type of thermal insulating materials.

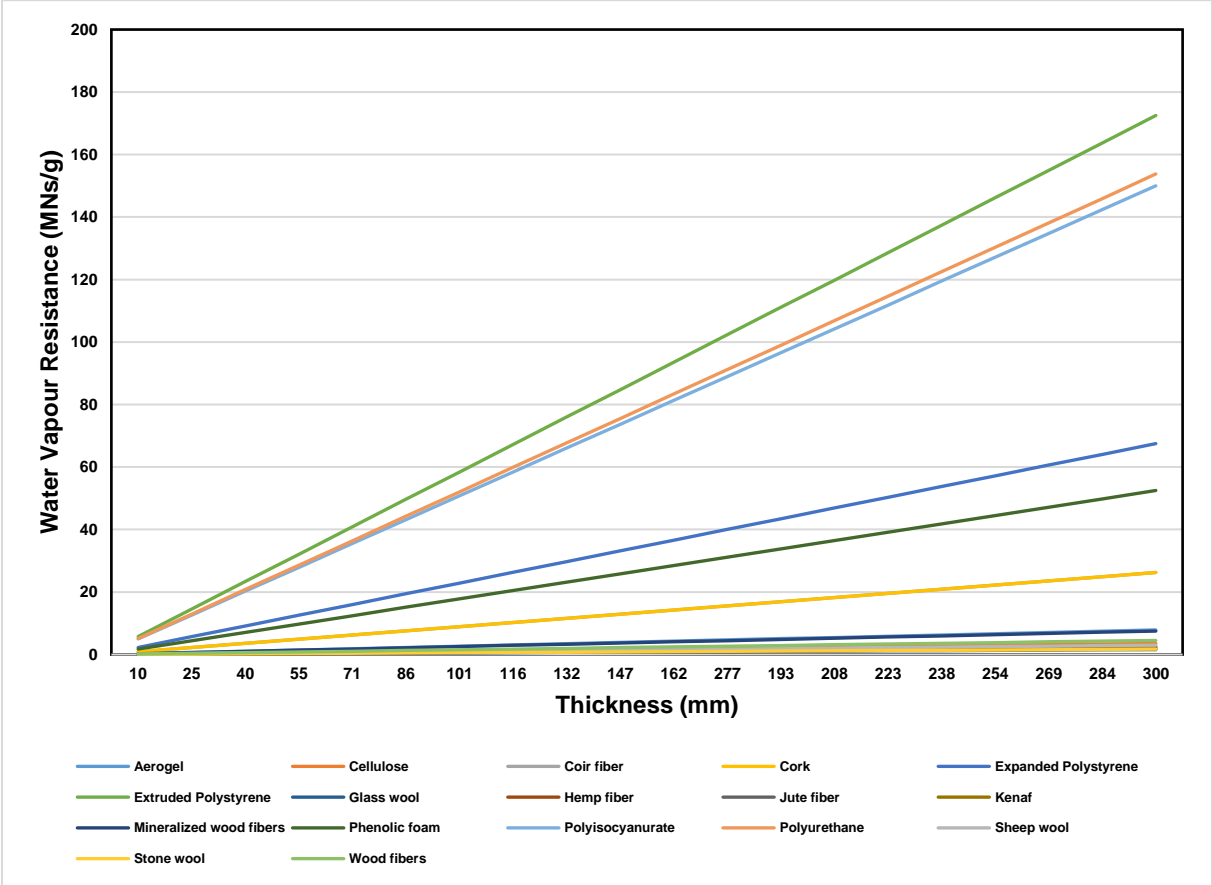


Figure 5.11. The effect of the thickness on the water vapor resistance value of various thermal insulating materials.

5.1.2. Phase Change Materials Theoretical Results

Six different PCMs are analyzed in terms of their energy and exergy efficiencies and temperature changes at high and low temperatures by changing the ambient temperature and the thickness of the PCMs. The results are investigated in this section with the graphs of these analyses, which show the change in the energy and exergy efficiencies and temperature of the PCMs.

Figure 5.12 indicates that the energy efficiency of the phase change materials increases when the temperature difference between the inside of the robot and ambient conditions. When the ambient temperature approximates the assumed inside temperature of the robot, the minimum heat transfer rate is seen.

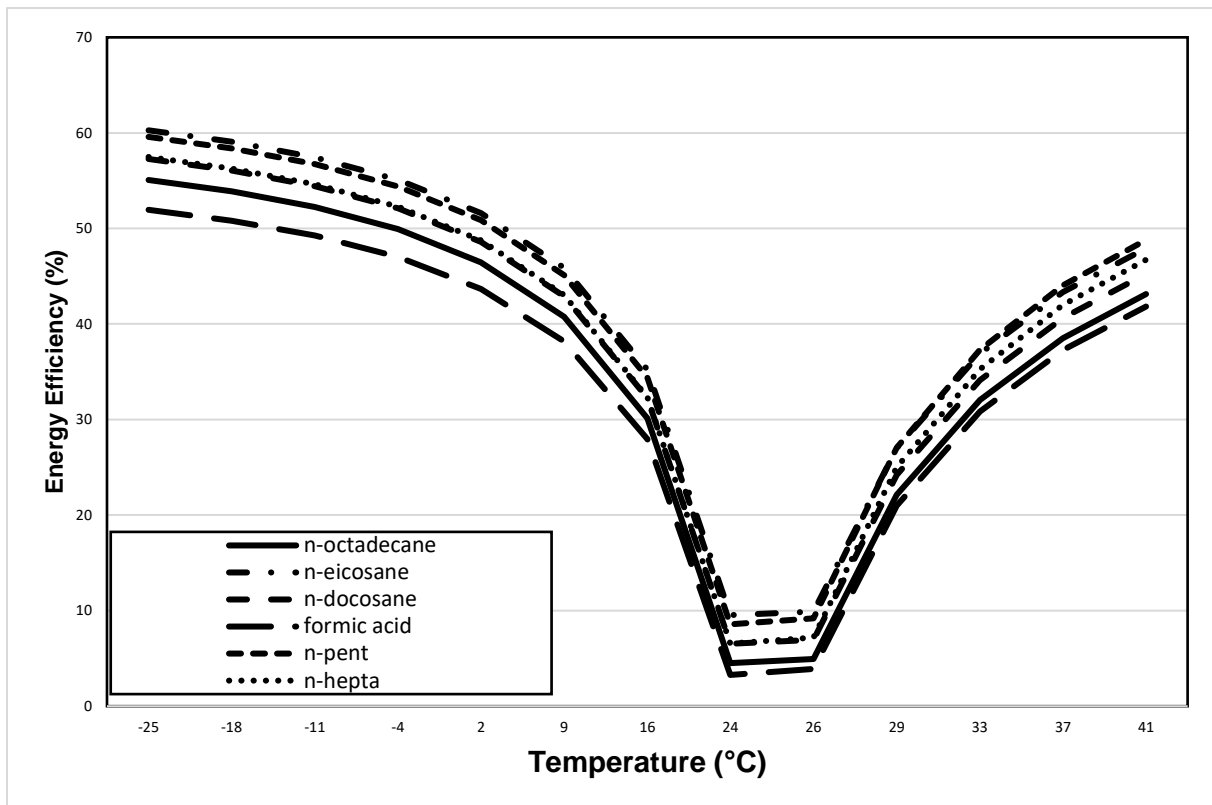


Figure 5.12. The effect of the ambient temperature on the energy efficiency of the PCMs.

Because of this reason, the energy efficiency of the PCMs decreases when the ambient temperature increases to around 25 °C. After this point, the energy efficiency increases as a reason of the upward heat transfer rate. In Figure 5.12, n-eicosane has the maximum energy efficiency value, which is 60.27%, when the ambient temperature is -25°C. The energy efficiency of the n-eicosane decreases to 9.53 % at 25 °C ambient temperature, but it reaches 47.93% with the increase of the ambient temperature to 40 °C. However, the energy efficiency values of the n-pentadecane are also very close to the values of n-eicosane. The energy efficiency of the n-pentadecane varies between 59.58% and 6.55%, while the ambient temperature rises from -25°C to 25°C. When the ambient temperature increases to 40°C, the energy efficiency of the n-pentadecane reaches 48.79%. However, formic acid has the lowest thermal performance as a phase change material, comparing to other PCMs options. The energy efficiency of the formic acid is estimated as 51.95% at -25°C, and 41.84% at 40°C.

On the other hand, the effect of the temperature increase on the thermal performance of the PCMs is analyzed from an exergy efficiency point of view and demonstrated in Figure 5.13. The exergy efficiency of n-pentadecane varies between 50.09% and 39.83 when the temperature increases to around 25 °C from -25°C as the highest exergy efficiency.

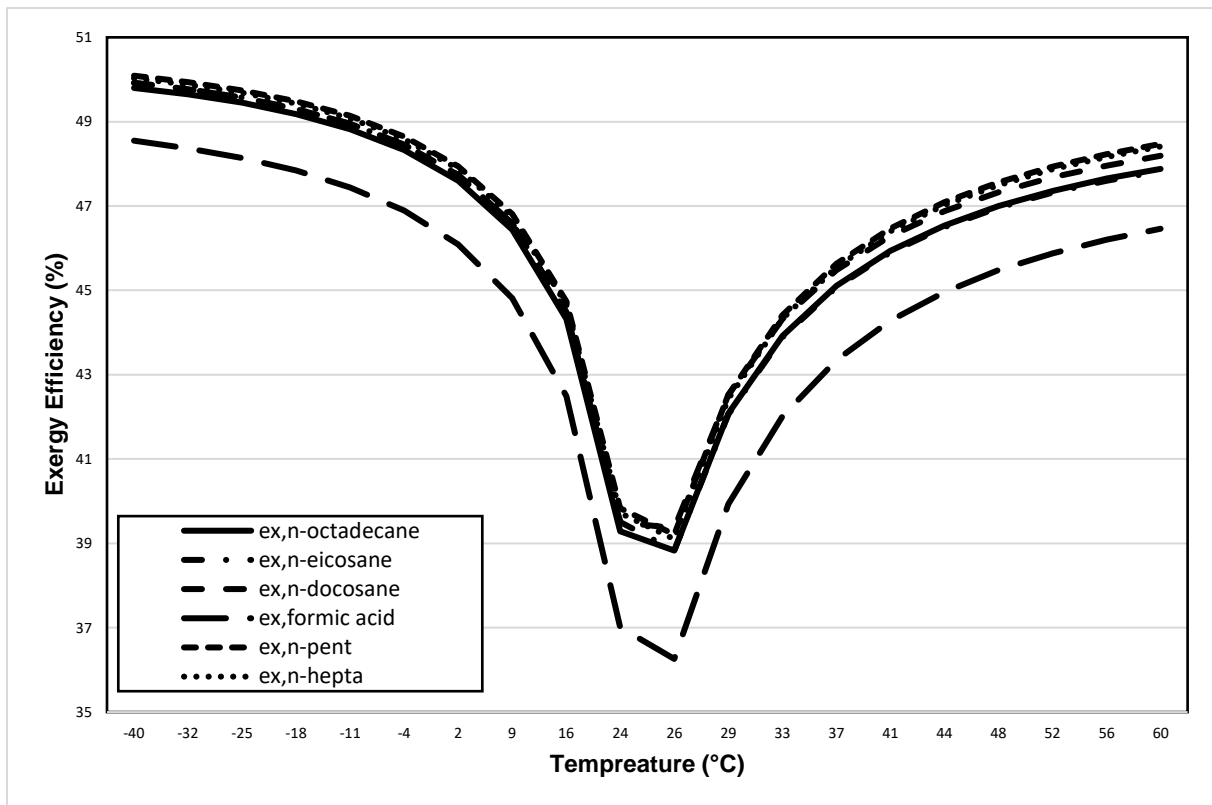


Figure 5.13. The effect of the ambient temperature on the exergy efficiency of the PCMs.

When the ambient temperature reaches 40°C, the exergy efficiency of n-pentadecane increases to 46.47%. On the other hand, the exergy efficiency of formic acid is obtained as the lowest exergy efficiency, comparing to other PCM options. The exergy efficiency of the formic acid decreases from 48.14% to 36.26%, while the ambient temperature rises to 25°C, and the exergy efficiency increases to 44.28% when the ambient temperature reaches to 40°C. Moreover, the exergy efficiencies of n-octadecane, n-eicosane and n-docosane changes with similar efficiency values, which are 49.45%, 49.57%, and 49.56%, respectively at low temperature. At 40°C ambient temperature, the exergy efficiency of the PCMs is 45.94% for n-octadecane, 45.9% for n-eicosane, 46.29% for n-docosane.

Figure 5.14 compares six different phase change materials in terms of the change in energy efficiency for various thickness of the PCMs at high temperature. The ambient temperature is assumed to be 40°C in this analysis. It can be seen that n-octadecane provides the highest thermal performance with the energy efficiency of 45.39 % when the thickness of the PCMs is 10 mm. However, the performance of the n-octadecane increases as a result of the change in the PCMs thickness from 10 mm to 100 mm. When the thickness is 100 mm, the energy efficiency of n-octadecane reaches 55.31 %. On the other hand, n-pentadecane has the lowest thermal performance among other PCMs options. The energy efficiency of the n-pentadecane increases slightly from 42.54% to 52.62%. Furthermore, the energy efficiencies of

n-heptadecane, n-pentadecane, n-eicosane and formic acid are 54.5 %, 52.62 %, 49.99 %, and 47.58 %, respectively.

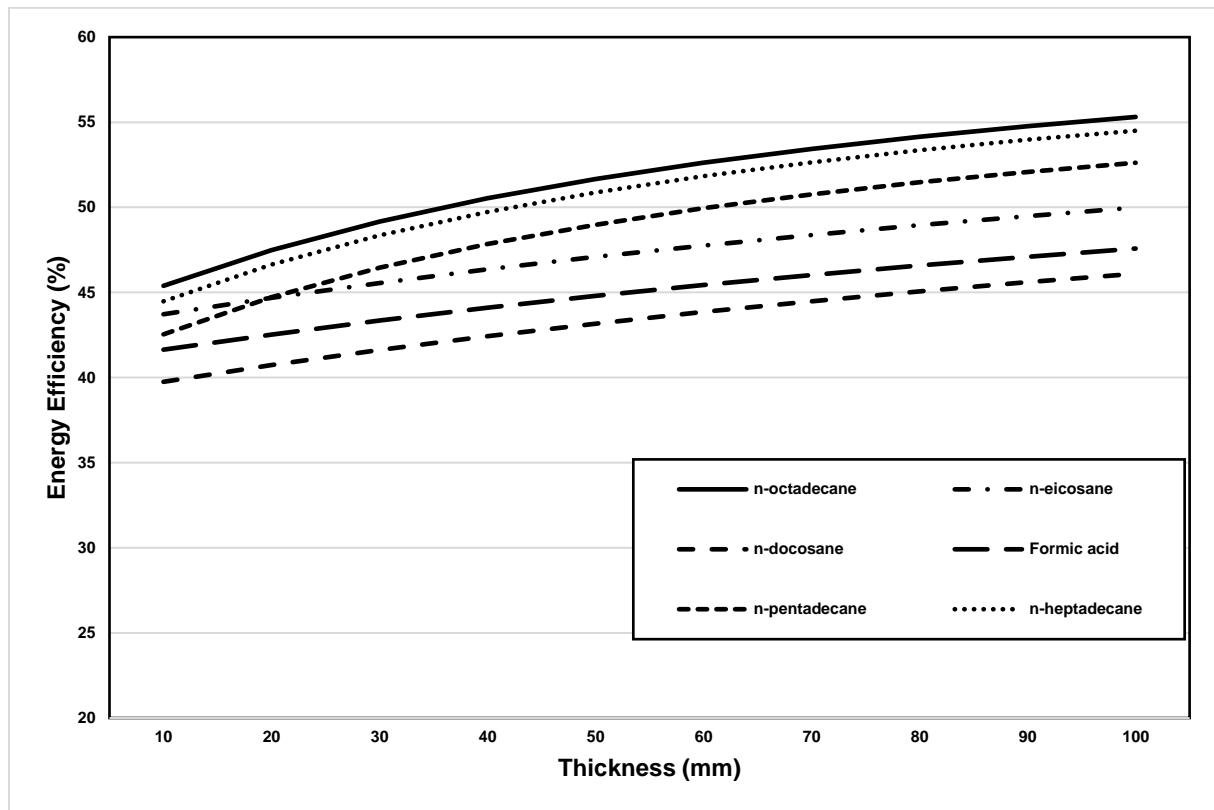


Figure 5.14. The effect of the PCMs thickness on energy efficiency at high temperature.

In Figure 5.15, the effect of the thickness of the PCMs on the exergy efficiency is analyzed. The thickness of the PCMs is increased from 1 mm to 10 mm, which also increases the amount of the PCMs and the latent heat capacity. Moreover, since the PCMs also provide thermal insulation, the increase of the thickness of the PCMs also changes the heat transfer rate between the inside and the outside of the robot. Therefore, the exergy efficiency analyses investigate this situation from the exergy point of view, which is directly related to the temperature difference between the surface of the robot and the ambient conditions. However, Figure 5.15 indicates that n-pentadecane has the highest exergy efficiency, which changes between 41.25% and 49.68%. The exergy efficiency of n-heptadecane varies in a similar range to n-pentadecane, which increases from 41.18% to 49.6%. On the other hand, the exergy efficiency of the n-docosane and n-octadecane change very close each other. The exergy efficiency of the n-docosane increases from 41.02% to 49.53% and the exergy efficiency of n-octadecane rises from 41.01% and 49.23%. Finally, the lowest exergy efficiency is obtained by formic acid as a phase change material. The exergy efficiency of the formic acid varies between 39.04% and 45.45%, while the thickness of the PCMs rises from 1 mm to 10 mm.

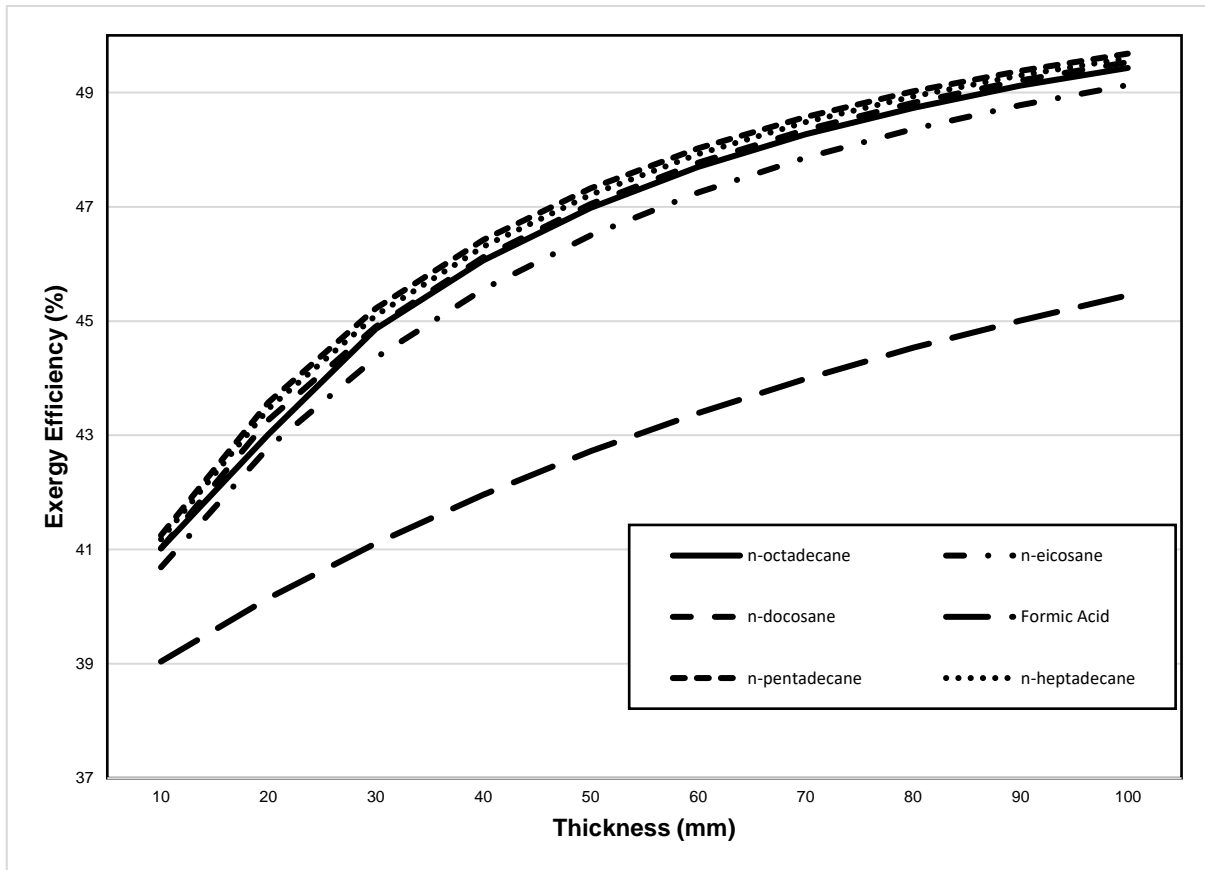


Figure 5.15. The effect of the PCMs thickness on exergy efficiency at high temperature.

The effect of the PCMs thickness on the energy efficiency at low ambient temperature is demonstrated in Figure 5.16. When the ambient temperature is $-25\text{ }^{\circ}\text{C}$, n-pentadecane provides the highest thermal performance, comparing to the other five options. The energy efficiency of the n-pentadecane increases moderately from 61.17% to 76.11%, while the thickness of the PCMs varies between 10 mm to 100 mm. However, the energy efficiencies of the n-eicosane, n-heptadecane, n-octadecane are also obtained high energy efficiency, and the increase of their energy efficiencies can be seen as similar. The energy efficiency of the n-eicosane rises from 59.36% to 74.5%. On the other hand, the energy efficiency of the n-heptadecane is very close to n-eicosane, which has an almost 4% difference between the energy efficiency values with the 10 mm and 100 mm PCMs thicknesses. Moreover, the energy efficiency of the n-octadecane changes between 58.86% and 73.43% corresponding to the increase of the PCMs thickness.

On the other hand, the change of the exergy efficiencies of the PCMs at low temperature is shown in Figure 5.17. The exergy efficiency of n-eicosane is the highest value, which changes between 45.19% and 50.81%, while the thickness of the PCMs layer increases from 1 mm to

10 mm. However, the exergy efficiency of the formic acid has the lowest rate with an increase from 43.55% to 50.81% corresponding to the change in the PCMs thickness.

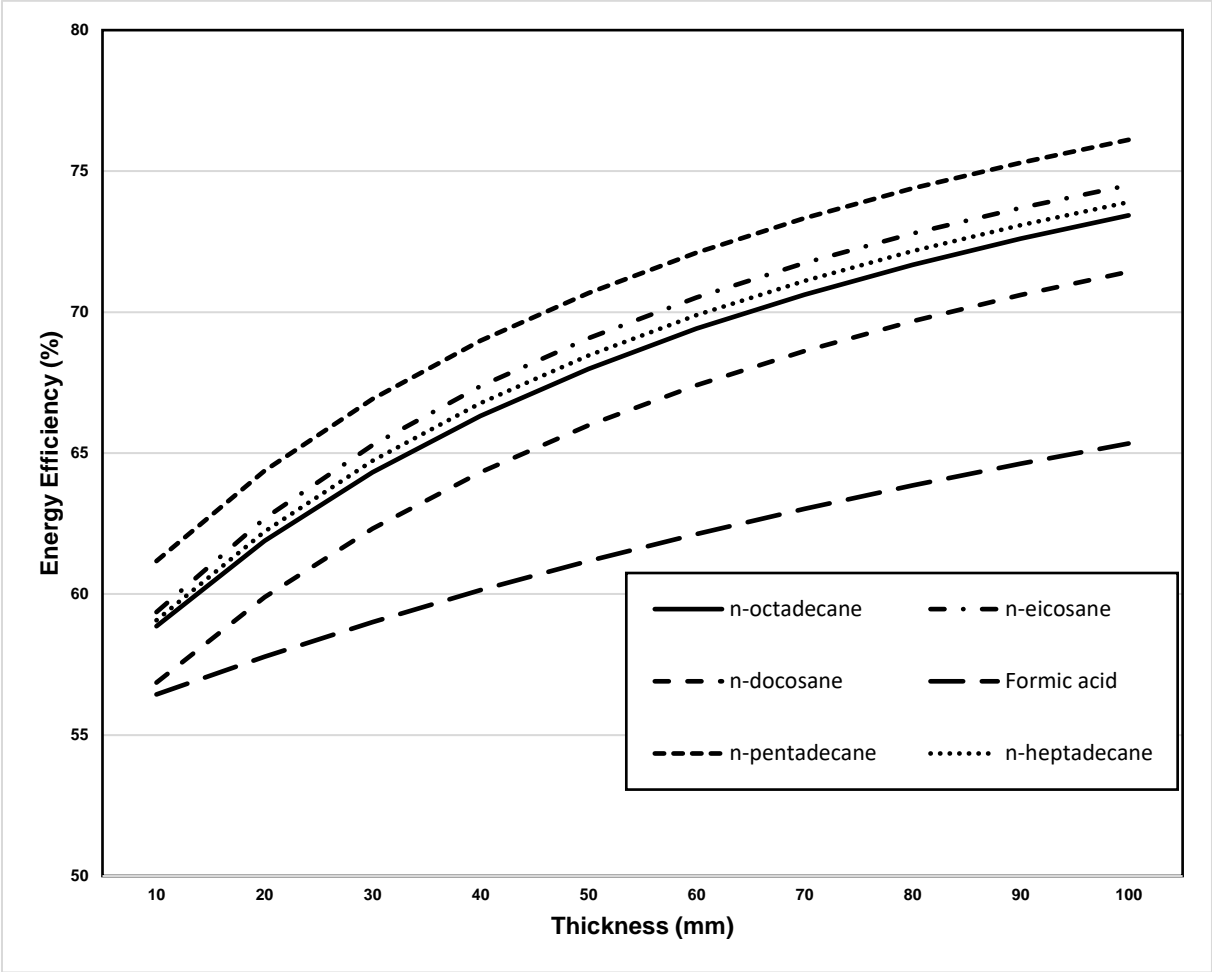


Figure 5.16. The effect of the PCMs thickness on energy efficiency at low temperature.

There is no doubt that, the PCMs layers that are located on the same direction of the heat transfer rate increases the thermal resistance of the surface and decreases the heat transfer rate between the inside and the outside of the robot. However, the latent heat capacity is another highly significant property of the PCMs, where the thermal energy storage takes place and reduces the heat transfer rate. One of the main parameters that affects the thermal energy storage performance during a particular operation is the melting point of the PCMs because only latent heat thermal energy storage takes place when a phase change is obtained. Because of this reason, it is clear that the thermal performance of the PCMs that have different melting points varies depending on the ambient conditions. Furthermore, a phase change material that has a good thermal performance at high ambient temperature may not be a reasonable solution for the thermal protection at low temperature. Therefore, it can be seen in Figure 5.17, formic acid and n-docosane have a lower thermal performance at low ambient temperature.

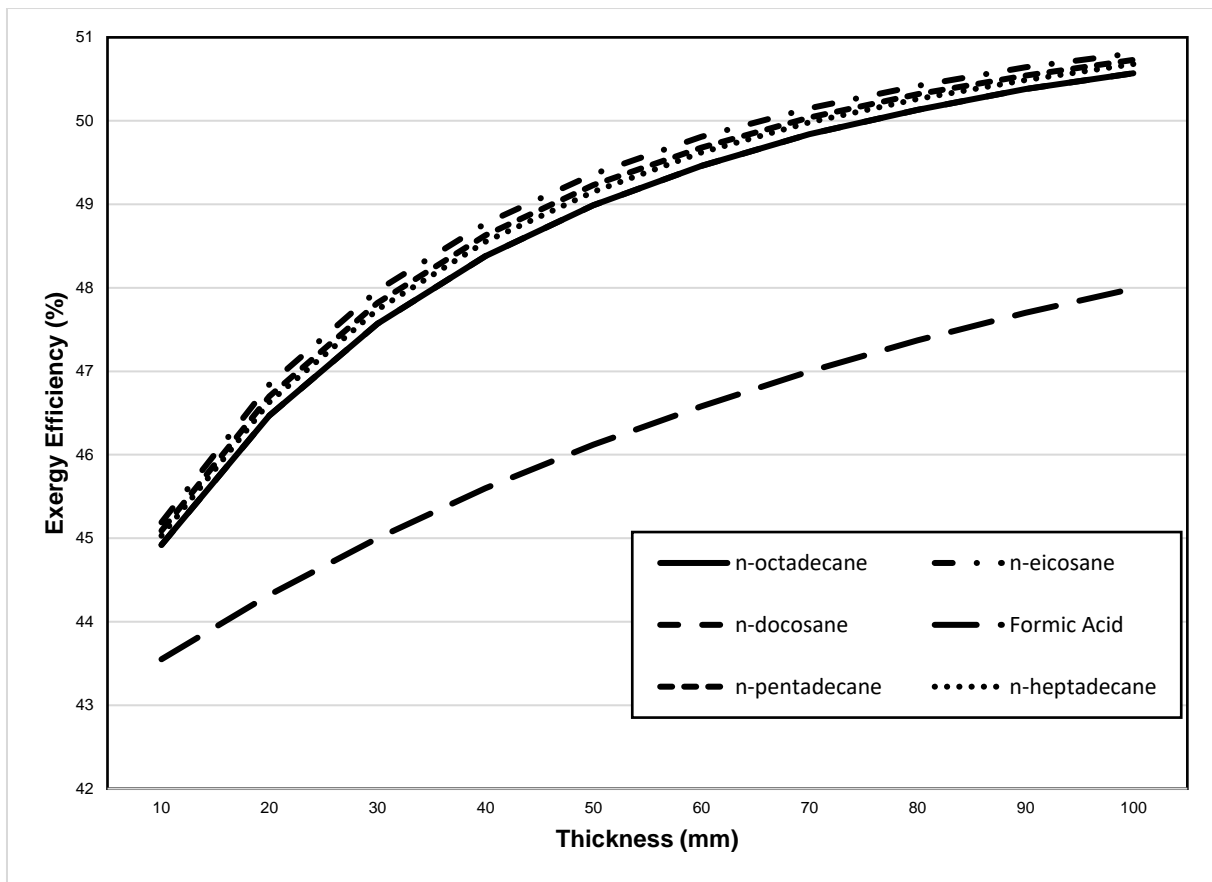


Figure 5.17. The effect of the PCMs thickness on energy efficiency at low temperature.

Another theoretical analysis is studied to define the duration of the melting process of the PCMs when the ambient temperature varies. Figure 5.18 shows the temperature change of the PCMs by time in minutes when the ambient temperature is 40 °C. It can be seen that n-octadecane and n-eicosane reach their particular melting temperature in almost the same duration. However, during the phase change process, the temperature of the n-octane stays almost constant at 28 °C, while the temperature of the n-eicosane is around 36 °C during the same phase change process. The temperature increase of the n-docosane is gradually higher than the other two PCMs. In almost 7 minutes, n-octadecane reaches its melting point, and the phase change process takes place for around 377 minutes. During the phase change from solid to liquid, the temperature of the n-octane stays almost constant. After 377 minutes, n-octadecane reaches 40 °C just in 41 minutes when the all PCM content transforms to the liquid phase. However, it takes nearly 32 minutes to increase the temperature of the n-eicosane to the melting temperature. After the melting point, all n-eicosane content of the system changes to the liquid phase in 390 minutes, but just in 14.59 minutes, the n-eicosane reaches 40 °C ambient temperature. Finally, the temperature of the n-docosane increases from 25 °C to 40 °C in 51

minutes without a completed phase change process, since the melting temperature of the n-docosane is higher than the assumed ambient temperature.

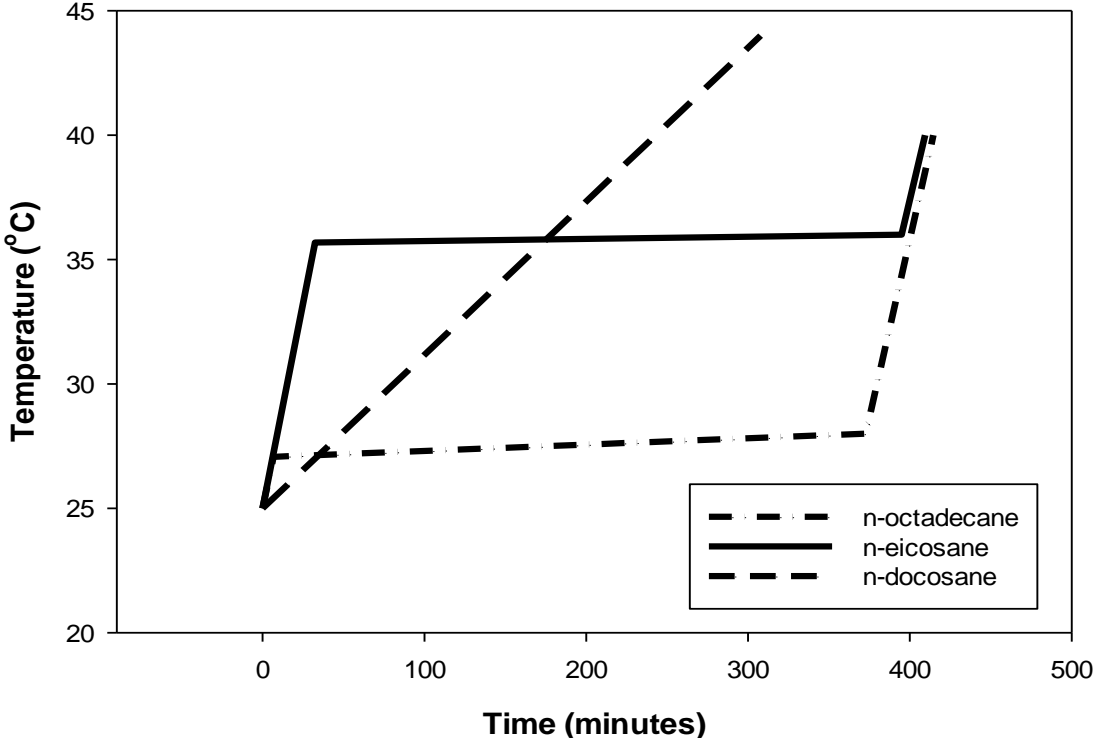


Figure 5.18. The temperature increase of the PCMs by time at high temperature.

Figure 5.19 compares three different PCMs in terms of the temperature increase in time when the ambient temperature is $-25\text{ }^{\circ}\text{C}$. It is clear that the n-hexadecane keeps the robot at a higher temperature for 161 minutes, while the formic acid keeps the robot at a lower temperature in 292 minutes. This comparison is significant because it means that there should be criteria while selecting the suitable PCM for a particular project, which is that selecting the PCM for a service time or higher inside temperature. However, the temperature of the formic acid decreases from $25\text{ }^{\circ}\text{C}$ to $7.8\text{ }^{\circ}\text{C}$ in 37 minutes, after that the melting process takes place and the formic acid completes the phase change in 292 minutes. Then, it reaches $-25\text{ }^{\circ}\text{C}$ just in 6 minutes. On the other hand, the temperature of the n-pentadecane declines to $10\text{ }^{\circ}\text{C}$, which is the melting point of the n-pentadecane, in 23 minutes and phase change process of the n-pentadecane takes 165 minutes in total. After the melting process, n-pentadecane reaches $-25\text{ }^{\circ}\text{C}$ in 8 minutes. Finally, the temperature of the n-hexadecane decreases from $25\text{ }^{\circ}\text{C}$ to $20\text{ }^{\circ}\text{C}$ in 7 minutes, after that, the melting process of the n-hexadecane is 161 minutes. When the melting process of the n-hexadecane is completed, the temperature of the PCMs decreases to $-25\text{ }^{\circ}\text{C}$ in 24 minutes.

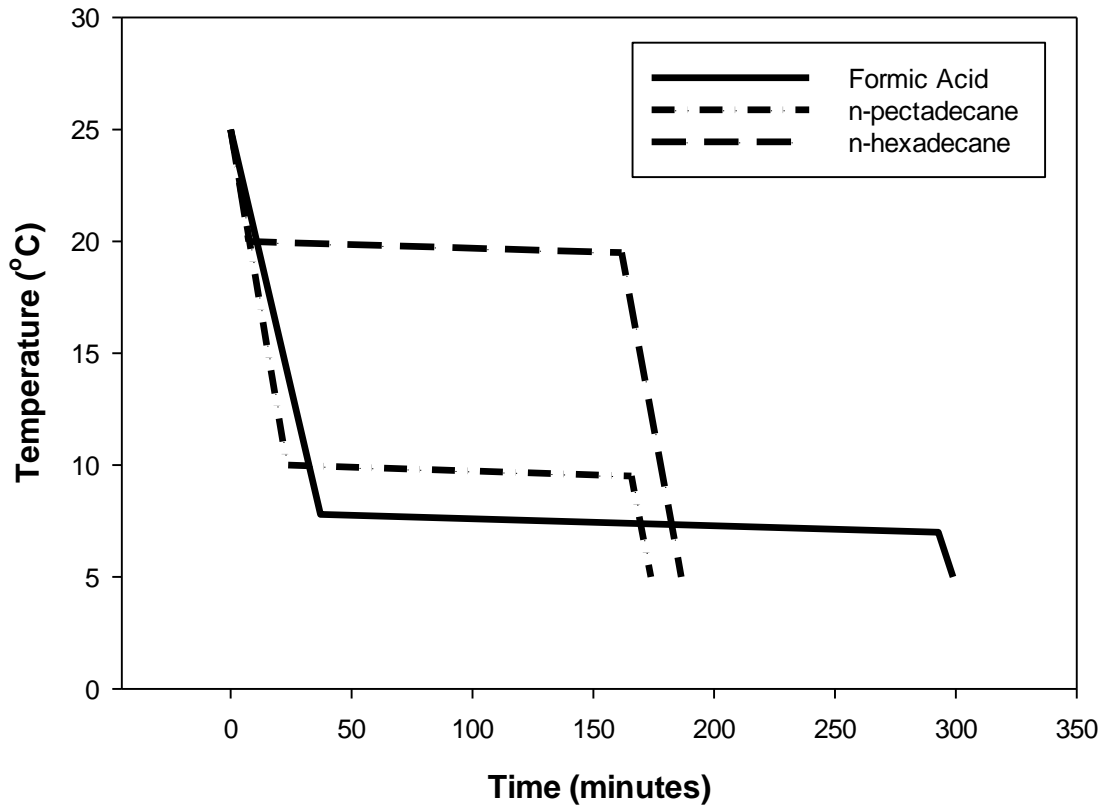


Figure 5.19. The temperature increase of the PCMs by time at low temperature.

5.1.3. Air Heating/Cooling Thermal Management System Theoretical Results

The air heating/cooling system is developed and theoretically analyzed in this thesis. The air heating/cooling system is a thermal management system that consists of an air compressor, compressed air pressure regulator, and vortex tube. The vortex tube is a tube that separates the compressed air into cold and hot air streams. The vortex tube does not include any moving parts and can be used with various gases. The idea of the forced air thermal management is that the cold stream is used for the enclosure cooling application, while the hot air stream is exhausted, and when the heating operation is required, the hot air stream is used for the heating purpose. However, the theoretical analyses of the air heating/cooling thermal management system are completed to compare the thermal performance of the system with different gases. Two main parameters of the vortex tube are analyzed in the theoretical study, which are the pressure of the inlet stream and cold/hot air mass ratio of the vortex tube.

Figure 5.20 compares the energy efficiencies of four different gases in terms of the change in the inlet pressure from 1 bar to 10 bar at high temperature. In this case, the system provides a cooling load to the robot, when the ambient temperature is 40 °C. It can be clearly seen that carbon dioxide has the highest thermal performance as the working fluid of the vortex tube. The energy efficiency of the system varies between 3.54% and 42.03%, while the inlet

pressure increases from 1 bar to 10 bar. On the other hand, the change in the energy efficiency of the thermal management system is obtained similarly for the air, neon, and nitrogen. The thermal performance of the air increases from 2.80% to 28.69 %, while the energy efficiency of the system changes between 2.81% and 28.69% with the working gasses of neon and nitrogen. However, since the thermal performance of the vortex tube rises corresponding to the increase in the inlet pressure, the higher energy performance of the thermal management system is obtained when the pressure is increased.

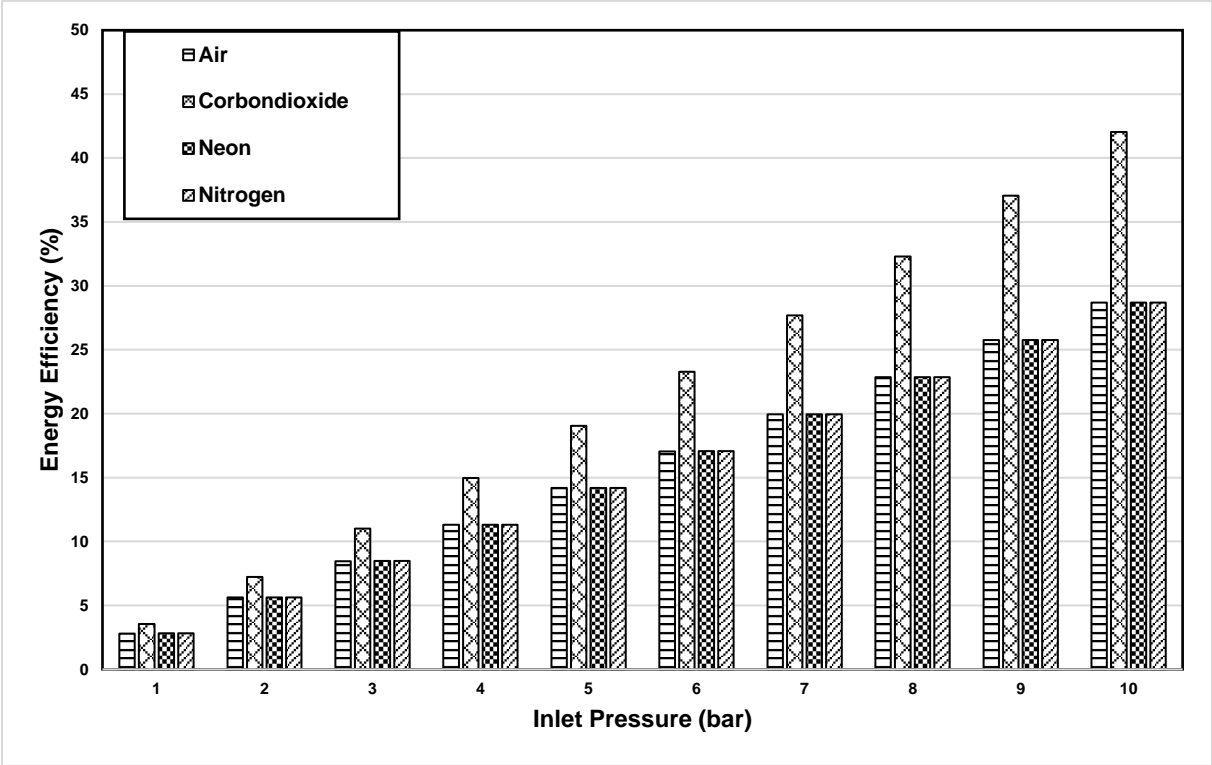


Figure 5.20. The effect of the inlet pressure on the energy efficiency of the air heating/cooling thermal management system at high temperature.

In Figure 5.21, the air heating/cooling thermal management system is analyzed from the exergy efficiency point of view with different working gasses at high temperature. The exergy efficiency of the system helps in showing the performance of the thermal management system in the reference to the environment. Because of this reason, it is highly significant to analyze the exergy efficiency of the system. The exergy efficiency of the system with air increases from 2.20% to 8.66%, when the ambient temperature is 40 °C and the inlet pressure changes from 1 bar to 10 bar. The exergy efficiency is a comparison factor that related to the ambient and surface temperatures of the robot. When the temperature difference between the ambient temperature and surface temperature of the robot increases, the exergy efficiency of the thermal management system decreases. However, the main purpose of a thermal management system

in a high-temperature environment should be decreasing the inside and the surface temperatures of the robot, meaning that the increase of the temperature difference is a desired situation. On the other hand, the exergy efficiency of carbon dioxide is higher than other working gas options. The exergy efficiency varies between 2.42% and 12.51% when the inlet pressure of the carbon dioxide increases gradually. Finally, the exergy efficiencies of neon and nitrogen have a similar percentage increment, which rise from around 2% to 9%.

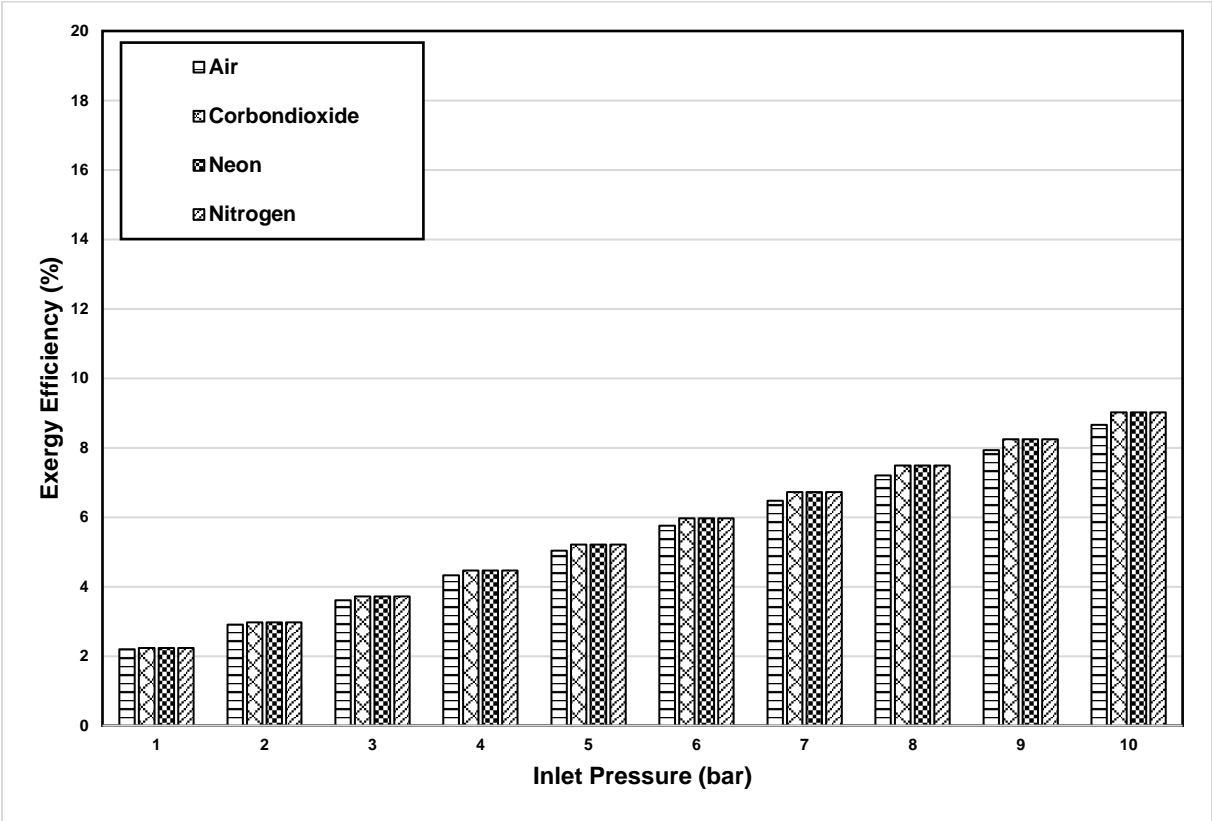


Figure 5.21. The effect of the inlet pressure on the exergy efficiency of the air heating/cooling thermal management system at high temperature.

When the ambient temperature is very low at $-25\text{ }^{\circ}\text{C}$, the energy efficiency rates of the thermal management are also analyzed to compare the thermal performance of the system with different working fluids. Figure 5.22 compares four different gases in terms of their energy efficiencies regarding the increase of the inlet pressure of the compressed stream. The purpose of the thermal management system in this analysis is to increase the inside and surface temperatures of the robot. Therefore, the compressed heat stream of the vortex tube is given to the inside of the robot, while the cold stream of the system is exhausted to the surrounding environment. There is no doubt that carbon dioxide provides the highest energy efficiency as a working gas, which increases between 3.23% and 35.71%. However, the energy efficiency of air varies between 2.45% and 24.91% at -25°C environment temperature, when the pressure of

the compressed air goes up from 1 bar to 10 bar. On the other hand, the thermal performances of neon and nitrogen are also similar to the performance of air. The energy efficiency of the neon and nitrogen changes between around 2% and 24%, because of the inlet pressure increase. It also should be mentioned that the energy performances of the air, neon, and nitrogen vary with the energy efficiencies that are very close to each other. Since the compressed air is a relatively cheaper process than the consumption of the neon and nitrogen, the air should be considered as a better solution. However, in some cases when the cooling or heating load is not enough for the particular applications, the carbon dioxide may be a better solution for the thermal management. Furthermore, out of the air, other gases require an additional storage tank, which may not be suitable for some specific applications of the mobile research robots.

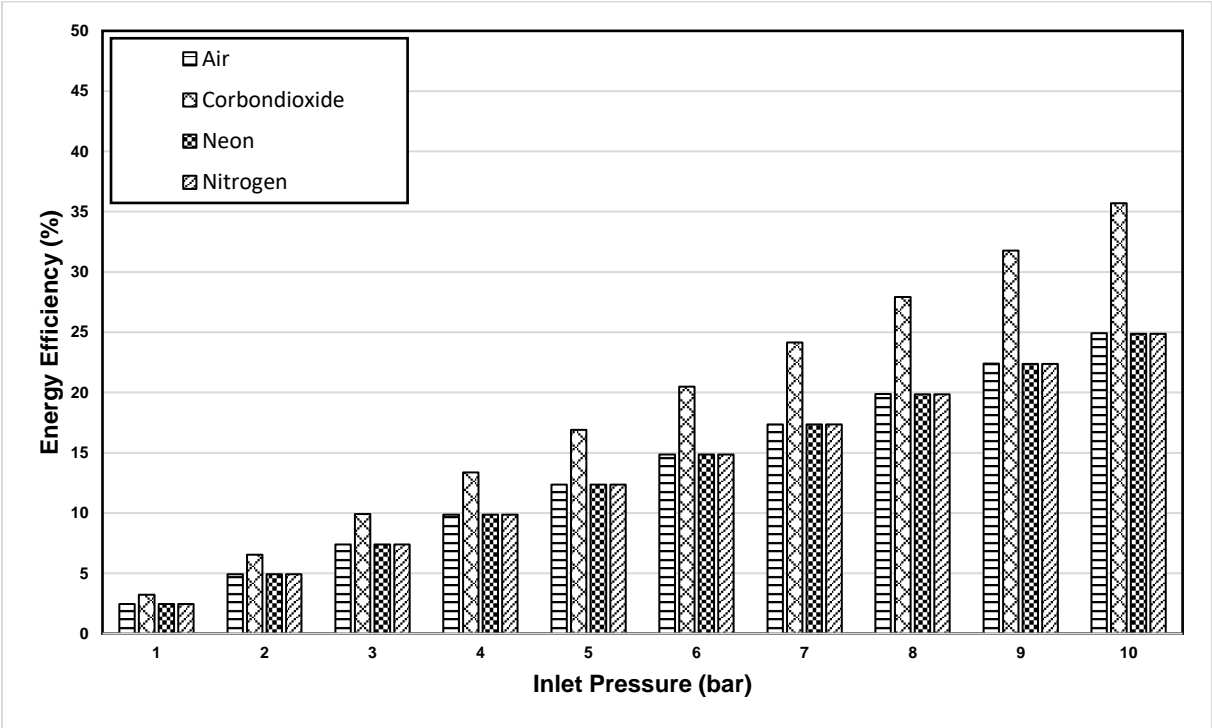


Figure 5.22. The effect of the inlet pressure on the energy efficiency of the air heating/cooling thermal management system at low temperature.

The exergy efficiencies of the system at low temperature with different inlet pressures are analyzed in Figure 5.23. Since the ambient temperature is very low, the thermal management system aims to increase the temperature difference between the inside of the robot and ambient condition that is the reference for the exergy efficiency analyses. The carbon dioxide shows higher exergy efficiency value, comparing to other three gases. The exergy efficiency of the system with carbon dioxide increases from 1.97% to 5.15%, while the inlet pressure rises from 1 bar to 10 bar. On the other hand, the exergy efficiency of the air as a working fluid changes between 1.86% and 5.15%, while the exergy efficiency of the neon

increases from 1.86% to 5.14%. Finally, the exergy efficiency of nitrogen varies very similar to neon, which rises from 1.80% to 4.98%.

Since vortex tube provides two separate streams, the mass ratio of these streams is also another important parameter that directly affects the thermal performance of the thermal management system. The cold and hot mass ratios are ratios between the total mass of the cold or hot streams and the total mass of the pressured air from the inlet of the tube. The cold and hot mass frictions of the tube is adjustable by a valve on the hot stream. When the mass ratio of the cold stream increases, the mass of the hot stream decreases. However, Figure 5.24 shows the effect of the cold mass friction on the energy efficiency of the thermal management system for four different gasses, which are air, carbon dioxide, neon, and nitrogen, respectively. In Figure 5.24, the energy efficiency of the carbon dioxide that has the highest increase from 4.83% to 48.32%. while the cold mass friction changes between 0.1 and 1. On the other hand, the energy efficiency of the air varies between 3.52% and 35.26%. Finally, the energy efficiency change of the nitrogen and neon is again similar to each other, because of the thermal properties of these two working fluids. The energy efficiency of these two gases increases from almost 3% to 35%, corresponding to the change in the cold mass friction of the vortex tube.

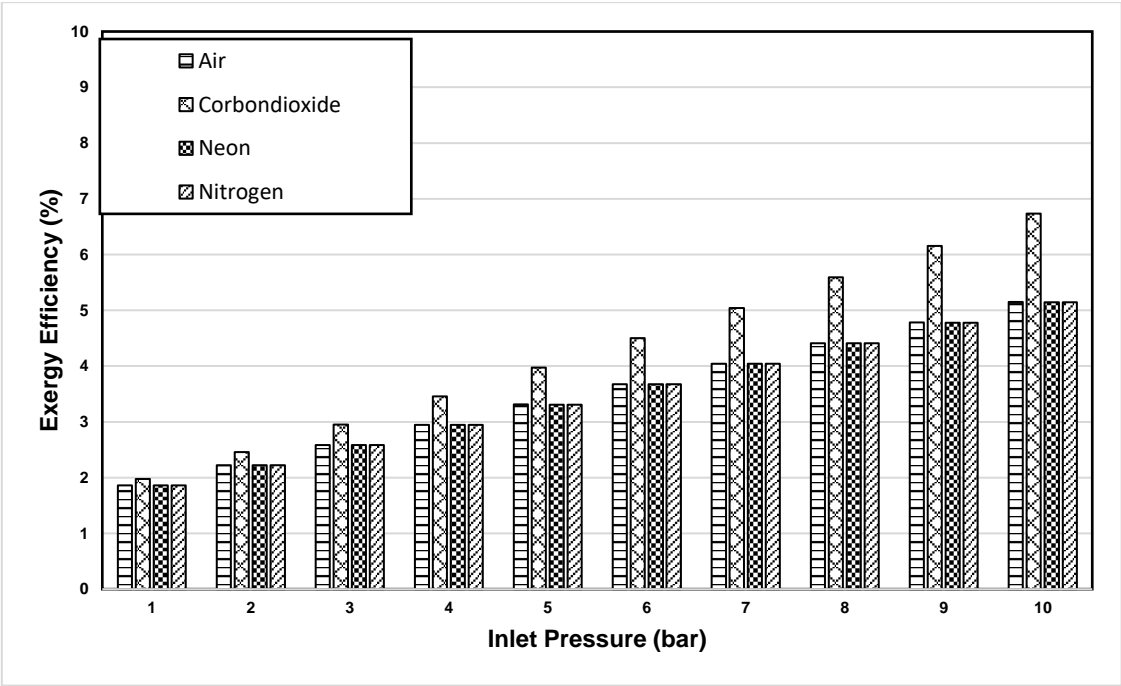


Figure 5.23. The effect of the inlet pressure on the exergy efficiency of the air heating/cooling thermal management system at low temperature.

Figure 5.25 demonstrates the effect of the cold mass friction on the exergy efficiencies of different gases. The exergy efficiency of the system is lower than the energy efficiency because of the large temperature difference between the inside and the outside of the robot. The

exergy efficiency of air increases from 0.88% to 8.80%, while the cold mass friction changes between 0.1 and 1 in Figure 5.25. It is an expected situation that the exergy efficiency is very low at the cold mass friction of 0.1 because of the low cooling load corresponding to the low mass flow rate of the cold stream. This can be seen for the other working gas options, where the energy efficiency of the carbon dioxide rises from 1.26% to 12.66%. However, the carbon dioxide again has the highest rate of the exergy efficiency. On the other hand, the exergy efficiency of neon varies between 0.92% and 9.24%. The exergy efficiency of the nitrogen changes similarly to the neon, and increases from 0.91% to 9.14%.

When the ambient temperature is lower than the inside of the robot, the thermal management system has to provide enough heating load to the inside of the robot to keep the electronic components at a reasonable operating temperature. In this case, the hot mass fraction of the thermal management system should be analyzed. As similar to the cold mass friction analyses, the hot air mass friction is increased from 0.1 to 1, and the change in the energy efficiencies is shown in Figure 5.26.

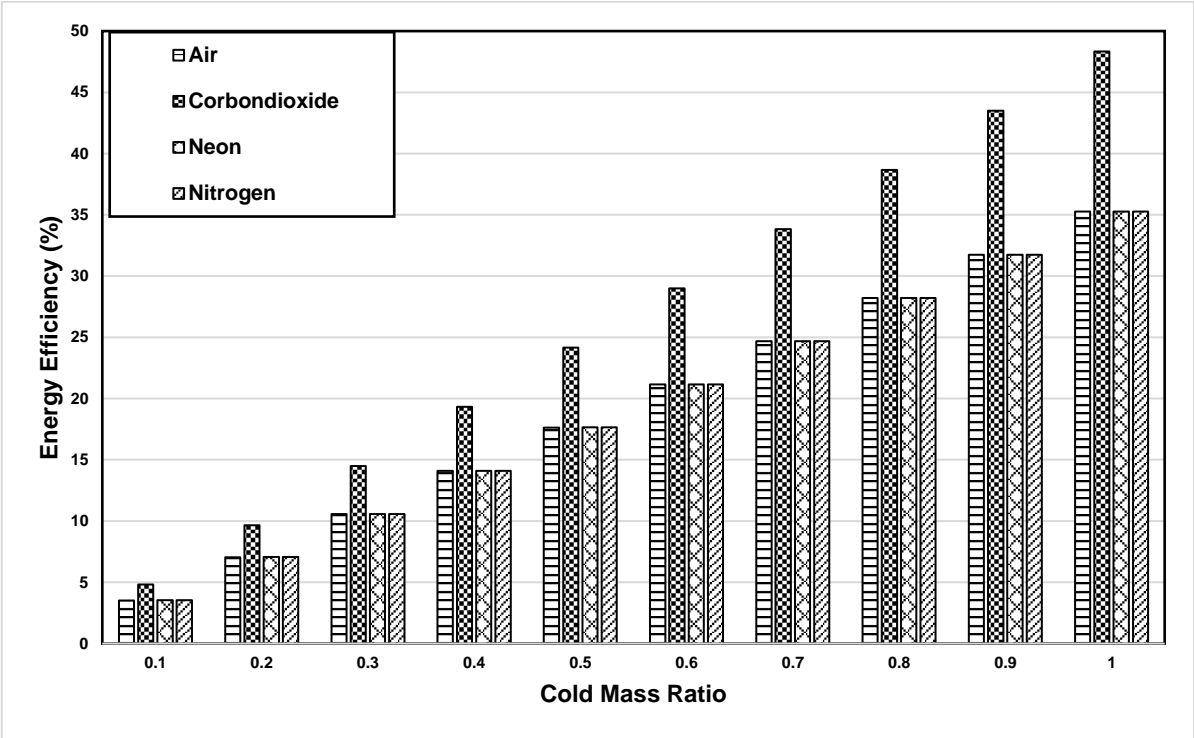


Figure 5.24. The effect of the cold mass ratio on the energy efficiency with different gases.

In Figure 5.26, there is no doubt that the increase of the hot mass friction has an upward change in the energy efficiency of the system. The carbon dioxide has the highest energy performance, while the energy efficiency of other gases decreases from highest to low as air,

neon, and nitrogen, respectively. The energy efficiency of carbon dioxide as a working fluid increases gradually from 4.23% to 42.43%, while the hot mass friction varies between 0.1 and 1. This dramatic increase in the energy efficiency also proves that the hot mass friction has a highly significant effect on the thermal performance of the thermal management system. On the other hand, the energy efficiency values for the air changes between 3.07% and 30.72%, corresponding to the change in hot mass friction ratio. However, the energy efficiency of the neon is 3% when the hot air mass friction is 0.1, but it also rises to 30.1% when the hot air mass friction reaches 1. Finally, the energy efficiency of the nitrogen increases from 3.06% to 30.69%.

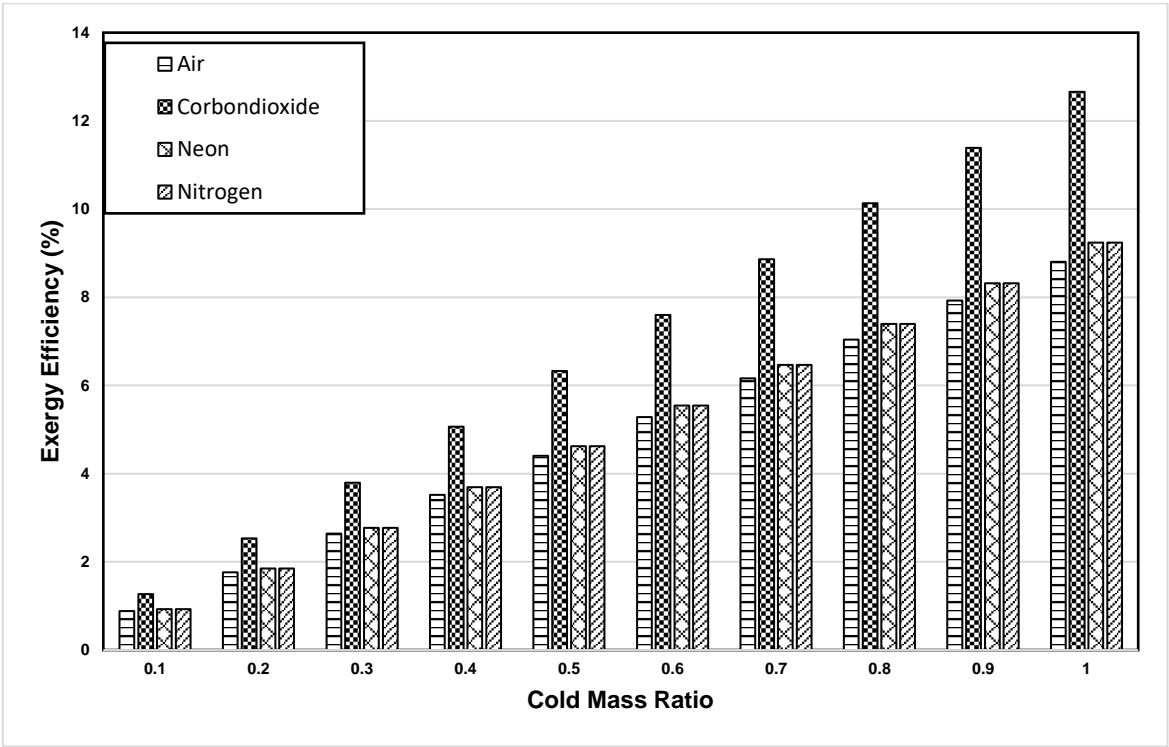


Figure 5.25. The effect of the cold mass ratio on the exergy efficiency with different gases.

Figure 5.27 analyses the effect of the hot stream mass ratio from an exergy efficiency point of view, while the hot stream mass ratio changes between 0.1 and 1. It can be easily seen that the exergy efficiency of the carbon dioxide is gradually higher than other working gas options for the thermal management system. The exergy efficiency of carbon dioxide increases from 0.62% to 6.21%, which are the highest exergy efficiencies. However, air also provides better exergy efficiency values than neon and nitrogen. The exergy efficiency of air rises from 0.45% to 4.5%, while the mass ratio of the hot air changes between 0.1 and 1. The exergy efficiency of neon rises from 0.44% to 4.12%, while the exergy efficiency of the nitrogen varies between 0.43% and 4.08%.

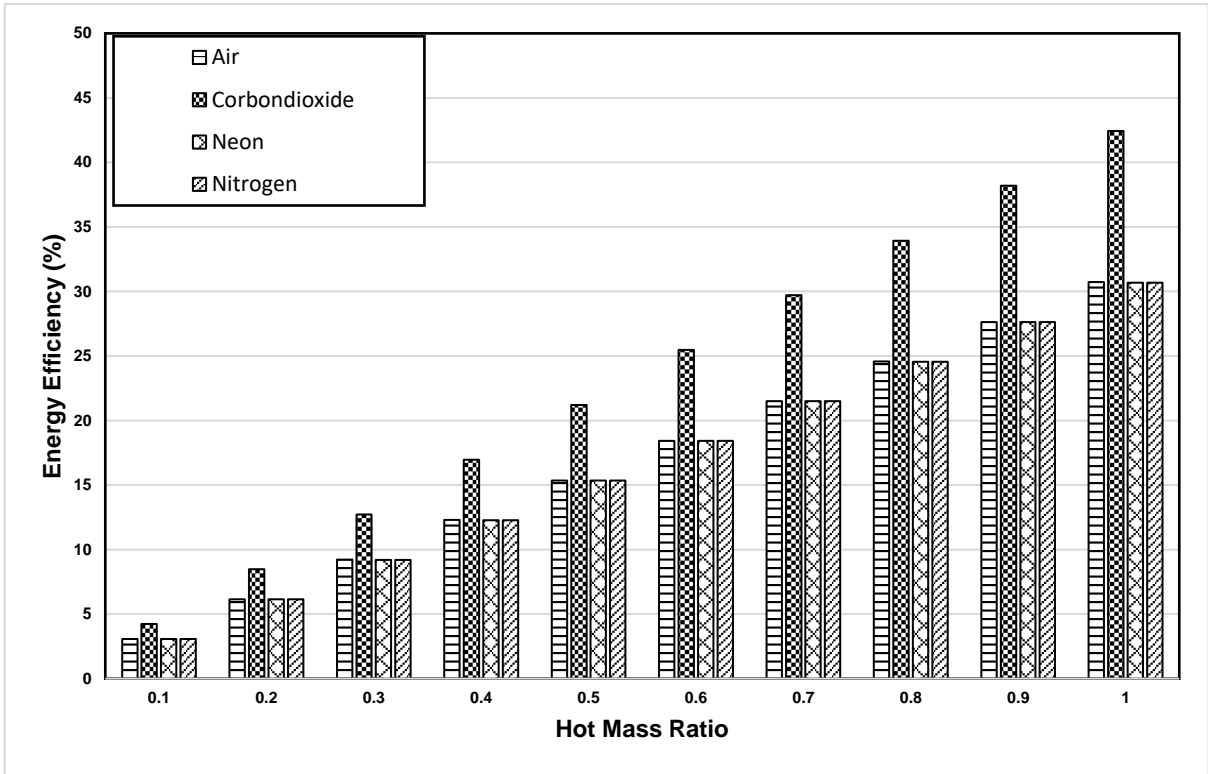


Figure 5.26. The effect of the hot mass ratio on the energy efficiency of the system.

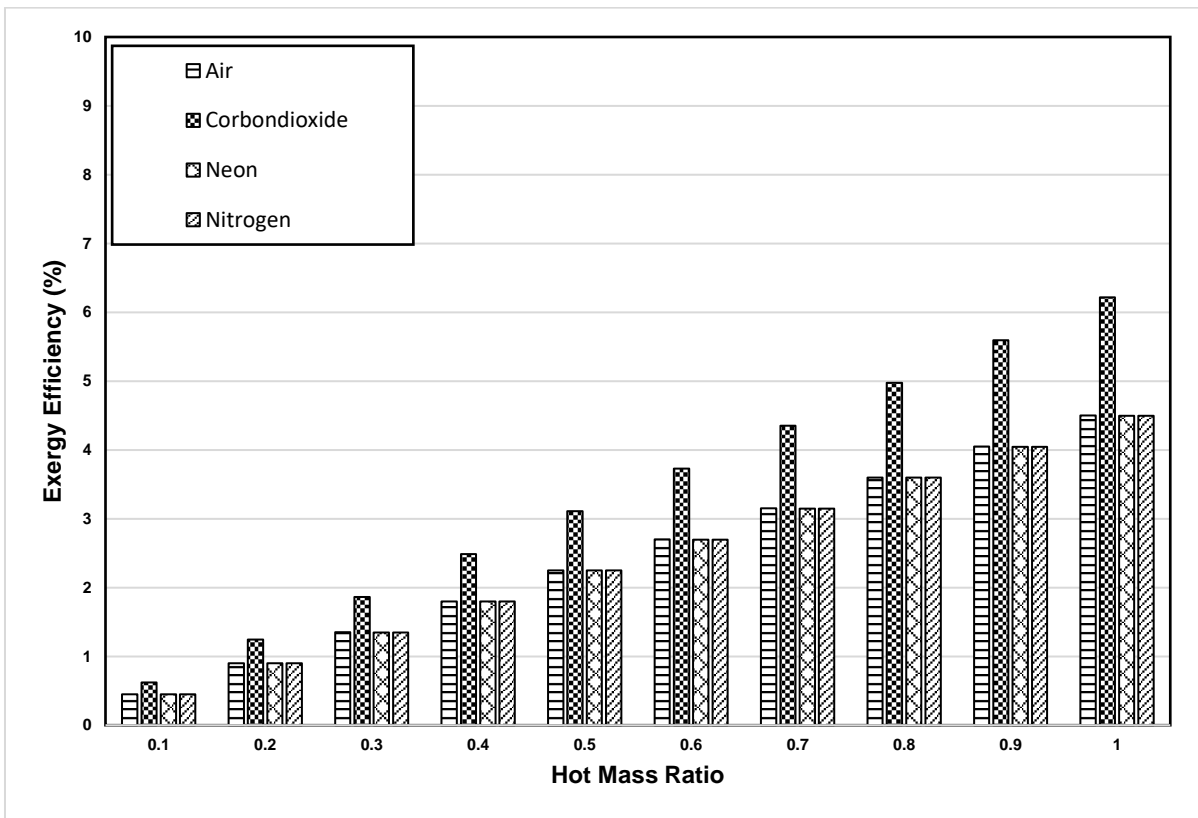


Figure 5.27. The effect of the hot mass ratio on the exergy efficiency of the system.

5.2. Experimental Results

In this thesis, three different thermal insulating materials and an air cooling/heating system are developed and tested in the small climatic chamber of ACE Wind Tunnel at both low and high temperatures. Therefore, the results of the experimental study are mainly divided into two sections namely experimental results at low temperature and experimental results at high temperature. At both temperatures, stone wool, fiberglass and extruded polyurethane insulating materials and the air cooling/heating thermal management system are tested to gain a clearer understanding of the thermal performance of these materials. Finally, the robot is tested without a thermal protection at high temperature, and the results are given in this section.

5.2.1. Experimental Results at Low Temperature

During the experiment, the room is cooled to -25°C and the temperature distribution data of the robot is collected. The first tested thermal insulation is the stone wool insulating material. The stone wool thermal insulating material is tested at -25°C for 17 minutes. The temperature distributions on different surfaces of the robot are given in Figure 5.28 when the robot is thermally protected by the stone wool insulating material. The data of the surface temperatures of the robot is collected from the bottom, left, right, top, and back sides of the robot. Moreover, the humidity probe, which is also able to measure the temperature, recorded the inside temperature of the robot, which is also given in Figure 5.28.

In Figure 5.28, the temperature changes on different points of the robot and the room are showed in terms of their distributions in time. The temperature of the climatic chamber is kept at -25°C during the experiment; however, the fluctuation of the room temperature can be easily seen in Figure 5.28. The room temperature in 17 minutes stays almost constant at -25°C , with some fluctuations that decrease to a minimum -25.2°C and increases to maximum -24.8°C . On the other hand, the inside temperature of the robot changes above 0°C during the test. It is also important that the initial inside temperature of the robot is 2.46°C at the beginning of the experiment. Because of the assembly of the insulating material and lifting the robot to provide a free rotation for the tires, the robot stays in the room for around 1 and 3 minutes without a protection, which is enough to cool down the surface temperature before the experiment. Because of this reason, the initial inside temperature of the robot is 2.46°C and decreases to 0.66°C in 17 minutes.

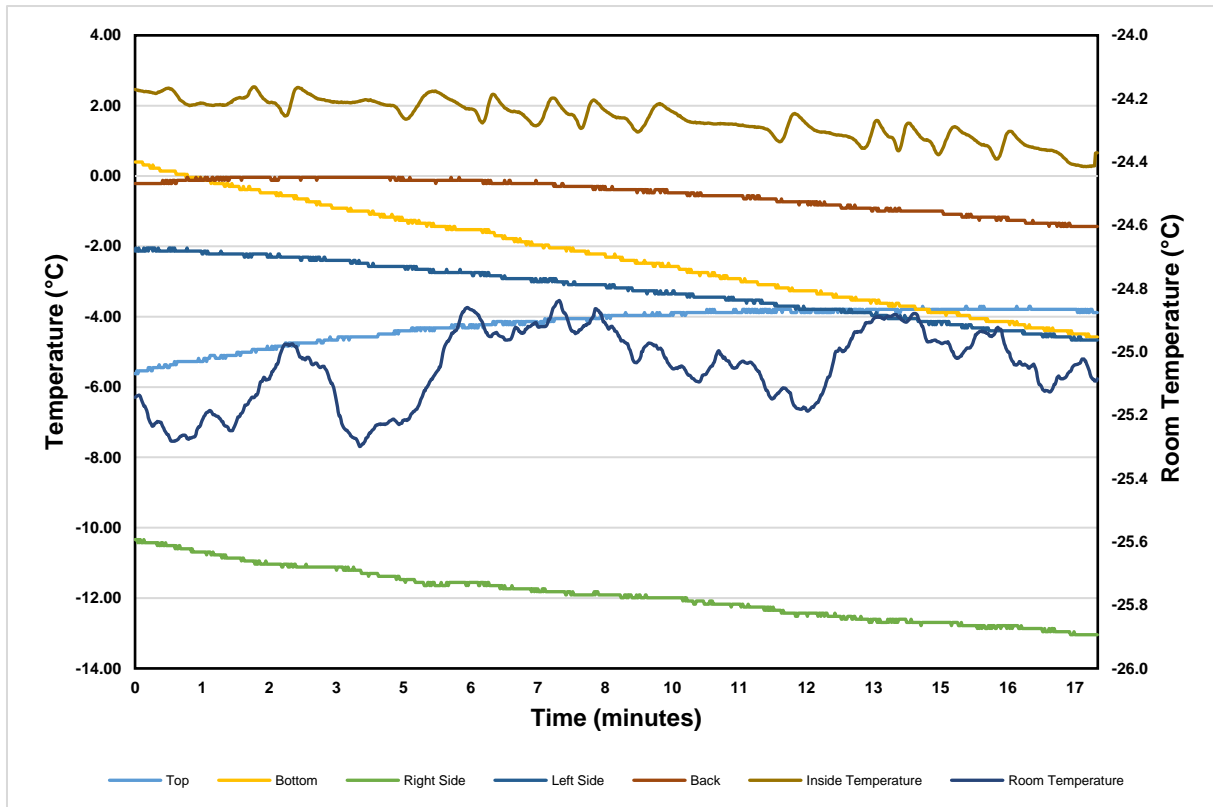


Figure 5.28. The experimental temperature distributions of the inside of the robot for stone wool thermal insulating material at low temperature.

There is another significant observation in the experiment, which is the reason of the temperature difference between the right and left sides of the robot even though they have the same surface area. The reason for this temperature difference between these two surfaces is the thermocouple cables that go out from the robot on the right surface. Because of the thermocouple cables, a gap between the thermal insulating material and the robot is observed, which significantly reduces the thermal resistance on the surface. Therefore, the temperature of the right side decreases from -10.34°C to -13.04°C , which are the recorded lowest temperatures on the robot, while the temperature of the right side changes between -2.13°C and -4.66°C in 17 minutes. Although the top and bottom surfaces have the same surface area, their temperature distributions are also different. The main reason for this situation is that the motor and battery of the robot are placed on the bottom surface. Therefore, the temperature of the bottom is obtained as higher than the temperature of the top surface because of the heat generation on both the motor and battery. The temperature of the bottom surface decreases from 0.40°C to -4.58°C , while the temperature of the top surface increases from -5.62°C to -3.88°C . Finally, the temperature of the back surface of the robot also decreases from -0.21°C to -1.43°C , which is the surface that is placed very close to the motor.

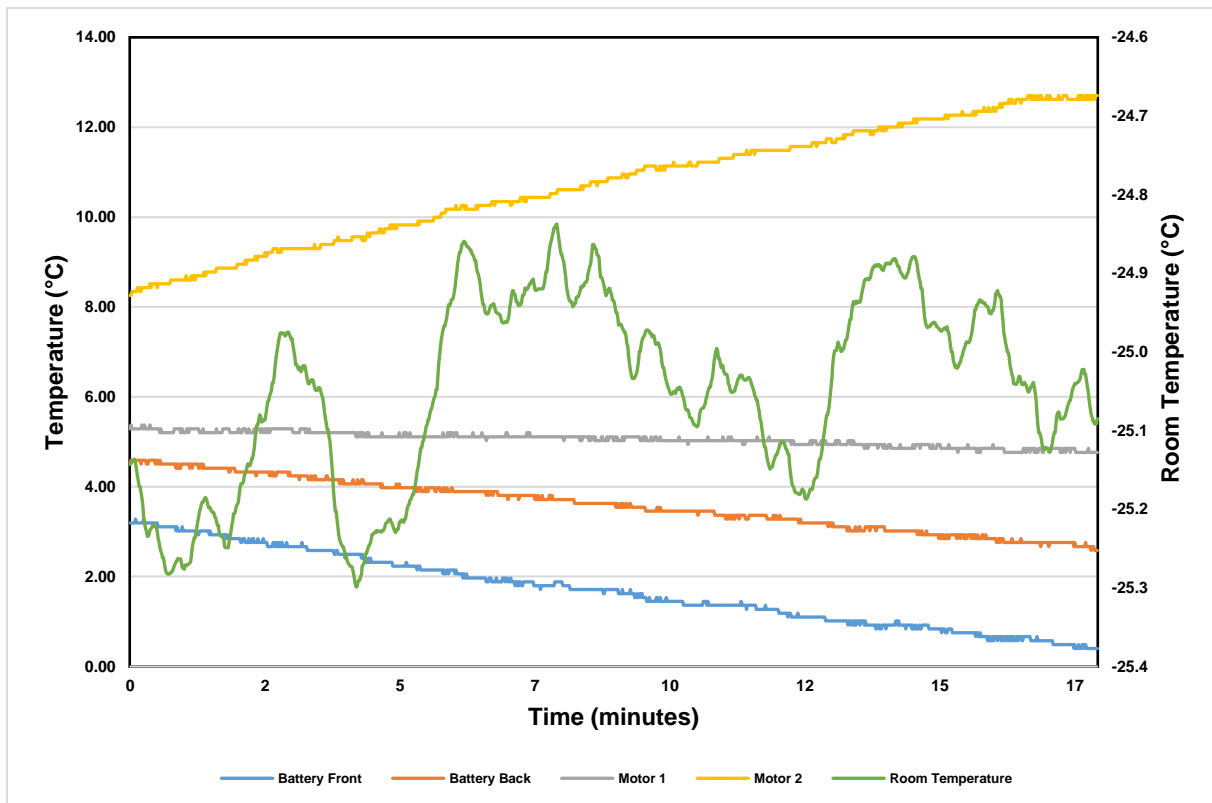


Figure 5.29. The experimental temperature distributions of the battery and the motor of the robot for stone wool thermal insulating material at low temperature.

The temperature changes on the battery and motor of the robot are also recorded for stone wool insulating material at -25°C and demonstrated in Figure 5.29. The temperature data of the battery is collected from two points on the battery. One of them is the front side of the battery, and the other one is the back side of the battery. It can be seen in Figure 5.29 that the temperature of the front side of the battery changes between 3.19°C and 0.40°C , while the temperature of the back side of the battery decreases from 4.50°C to 2.58°C . Because of the heat generation on the battery, it is a remarkable point that the temperature change on the battery is lower than the surfaces of the robot. On the other hand, two thermocouples collected the temperature data from two different points on the motor. The outer surface of the motor consists of two different materials, one of them is metal that is numbered as 1, and another one is a type of plastic component that is numbered as 2. Therefore, the temperature difference between the temperature recording points of motor 1 and motor 2 can be seen in Figure 5.29. Since different materials have different thermal conductivity values, the temperature of the motor increases differently at these two points. The temperature of the point of the motor 1 slightly decreases to 4.76°C from 5.29°C , while the temperature of motor 2 increases from 8.25°C to 12.71°C as a reason of the heat generation on the motor. Therefore, the effect of the different materials on the heat transfer rate is clear for the motor.

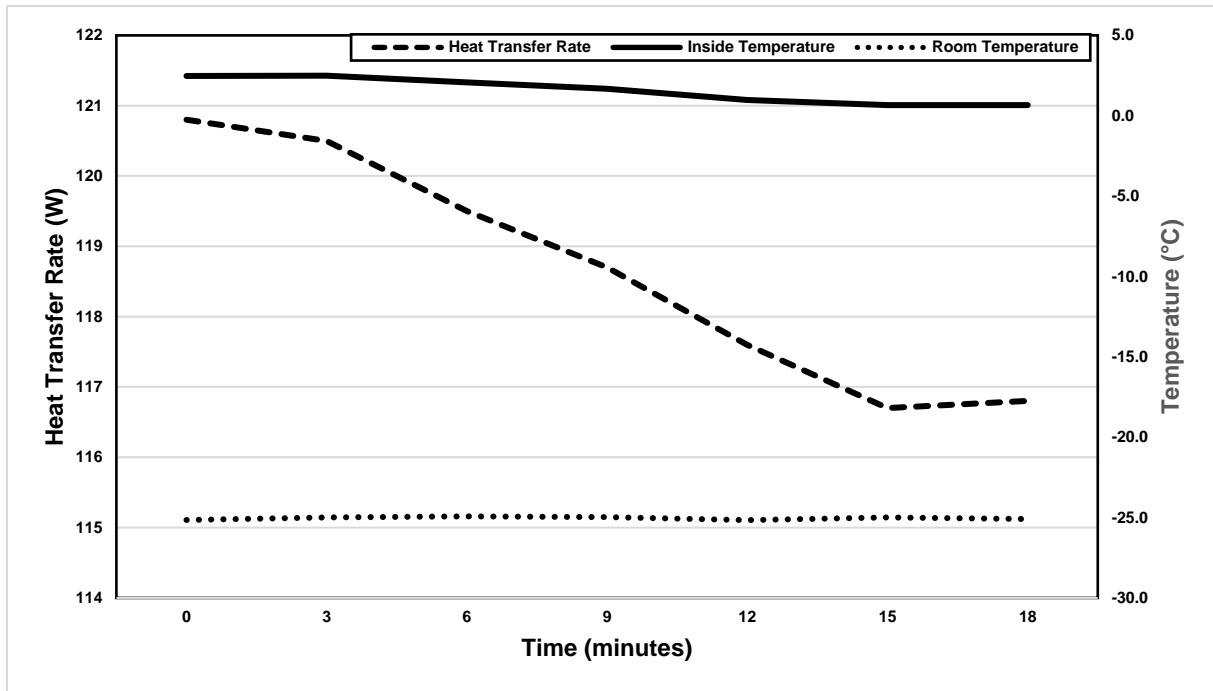


Figure 5.30. The experimental heat transfer rates of the robot for stone wool insulation at low temperature.

The heat transfer rate between the inside of the robot and the climatic chamber is analyzed in Figure 5.30. Figure 5.30 shows the change of the heat transfer rate of the robot on the first Y-axis: the inside and outside temperatures of the robot are represented on the secondary Y-axis. There is no doubt that the heat transfer rate of the robot decreases when the inside temperature of the robot approximates the ambient temperature. When the temperature difference between the robot and outside is getting closer to each other, the heat transfer rate decreases corresponding to this temperature difference. From the beginning of the experiment to around 4th minutes, the heat transfer rate decreases slightly from 120.8W to 120W. After that, the heat transfer rate decreases considerably to 116.7W. In last two minutes, the heat transfer rate stays almost constant at 116.8W, when the inside temperature slowly changes between 0.659°C and 0.7°C.

Corresponding to the heat transfer rate of the robot, the energy and exergy efficiencies of the stone wool thermal insulating material are also analyzed at low temperature in Figure 5.31. It can be easily seen that the energy efficiency of the stone wool cover is almost constant during the experiment. The energy efficiency of stone wool insulating material decreases very slightly from 50.46% to 49.41%. On the other hand, the exergy efficiency of the thermal insulating material decreases, corresponding to the decrease of the surface temperatures of the robot.

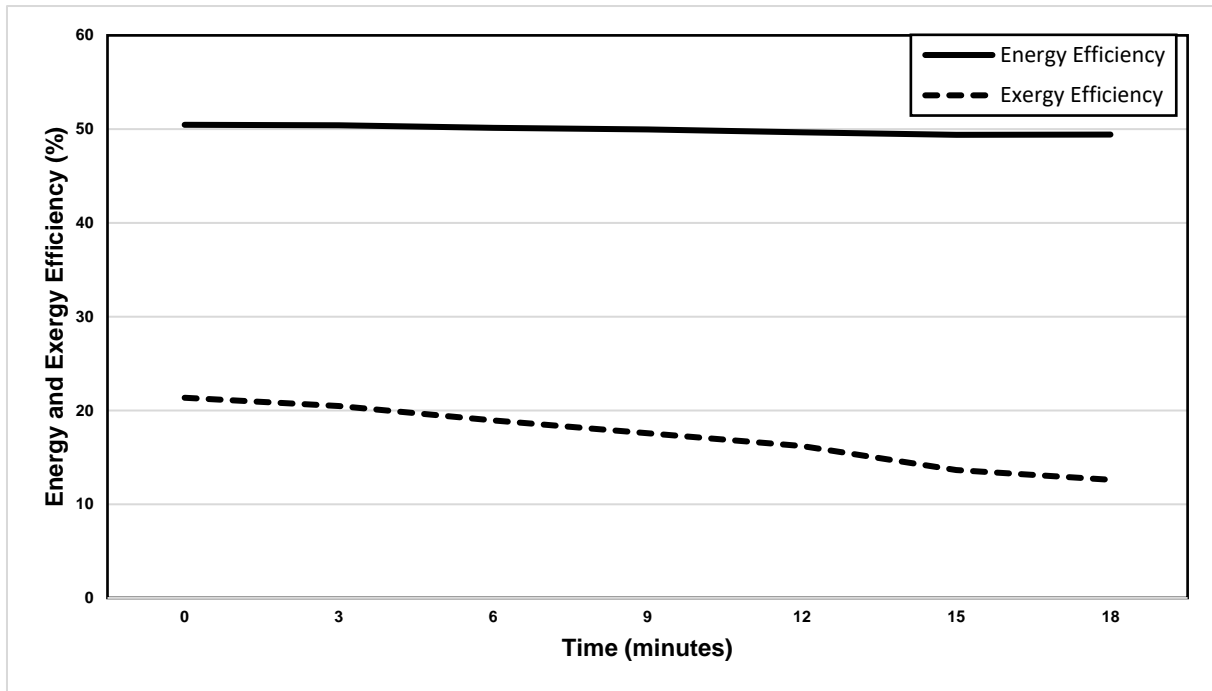


Figure 5.31. The energy and exergy efficiencies of the stone wool insulating material at low temperature.

The exergy efficiency analysis requires a comparison between the surface temperature and outside temperature to obtain the exergy performance of the insulating material. The exergy efficiency of the stone wool insulating material decreases from 21.35% to 12.6% in 17 minutes. Moreover, the uncertainties for the temperature results of the experiment is seen in Table 5.1.

Table 5.1. Uncertainties table for the results of stone wool insulation experiment at low temperature.

Measurement Parameter		Device	Accuracy
Temperature		Thermocouple K	$\pm 0.4\%$
Temperature		DAQ	$\pm 0.5^\circ\text{C}$
Time	Parameter	Value	Total Uncertainties (%)
5	Room Temperature	-24.93 ± 0.0997	0.1764
	Inside Temperature	2.07 ± 0.008306	
	Surface Temperature	-2.74 ± 0.01109	
	Heat Transfer Rate	119.5 ± 0.2109	
10	Room Temperature	-24.97 ± 0.0998	0.1777
	Inside Temperature	1.66 ± 0.00666	
	Surface Temperature	-3.18 ± 0.01272	
	Heat Transfer Rate	118.7 ± 0.211	
15	Room Temperature	-24.99 ± 0.09994	0.1807
	Inside Temperature	0.65 ± 0.002637	
	Surface Temperature	-4.23 ± 0.01692	
	Heat Transfer Rate	116.6 ± 0.2107	

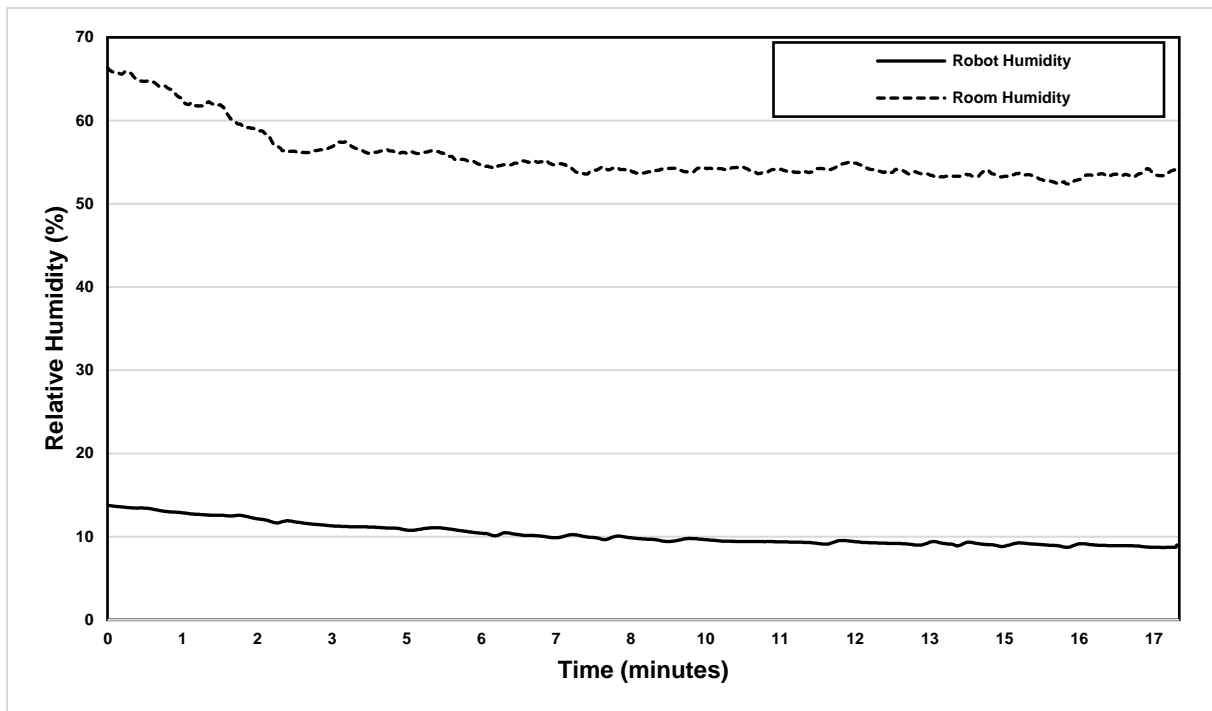


Figure 5.32. The comparison between the relative humidity percentages of the inside and outside of the robot with the stone wool insulating material at low temperature.

The relative humidity change of the inside of the robot and the climatic chamber is also recorded during the experiment. Figure 5.32 compares the inside and outside of the robot in terms of the relative humidity contents. To keep the relative humidity inside of the robot as possible as low, a desiccant pack is placed inside of the robot. Therefore, the relative humidity content of the inside of the robot decreases from 13.75% to 8.97%. In 8 minutes, the desiccant pack keeps the relative humidity at around 10%. The relative humidity decreases moderately to 8.7% in 11 minutes. The relative humidity of the climatic chamber decreases noticeably from 66.3% to 56% in 4 minutes, and then reduces slowly to 54.2% in 13 minutes with some fluctuations of 2%.

Figure 5.33 demonstrates the distribution of the surface temperatures of the robot in 17 minutes at -25°C when the fiberglass thermal insulating material is applied to the robot. The initial temperature of the inside of the robot is 3.10°C at the beginning of the experiment. The inside temperature of the robot decreases slightly to 2°C , however, the lowest inside temperature value is seen as 1.73°C in Figure 5.33. On the other hand, the lowest temperature readings for the fiberglass insulating material can be seen on the right side of the robot. The right side temperatures of the robot change between -2.66°C and -9.64°C with some fluctuations that reach minimum -9.73°C . On the other hand, the surface temperature of the left side of the robot reduces -0.65°C to -3.62°C , which is noticeably higher than the right side of the robot. The surface temperature of the bottom of the robot decreases moderately from -2.05°C to -5.27°C ,

while the temperature of the top surface varies between 5.11°C and 0.33°C. One of the main reasons of these temperature differences between the bottom and the top of the robot, even though they have the same surface area, is that the robot is moved on a pallet that soaks the low temperature and avoids the temperature increase of the bottom surface, when the robot is kept outside between the trials to increase the surface temperatures during the experiment. However, the surface temperatures of the backside of the robot are recorded between 0.31°C and -1.26°C. Moreover, the room temperature changes between -24°C and -25.4°C during this part of the experiment.

The surface temperature readings of the battery and motor of the robot are shown in Figure 5.34 at low temperature. When the robot is thermally protected by the fiberglass insulating material, the surface temperature of the front side of the battery decreases to 0.92°C from 2.58°C. On the other hand, the surface temperature of the backside of the battery reduces from 3.10°C to 2.23°C. Out of the battery temperature readings, the motor surface temperatures are also recorded with the fiberglass insulating material. The surface temperature of the motor drops from 5.28°C to 3.72°C on the first reading point, while the surface temperature changes between 10.52°C and 7.91°C on the second reading point.

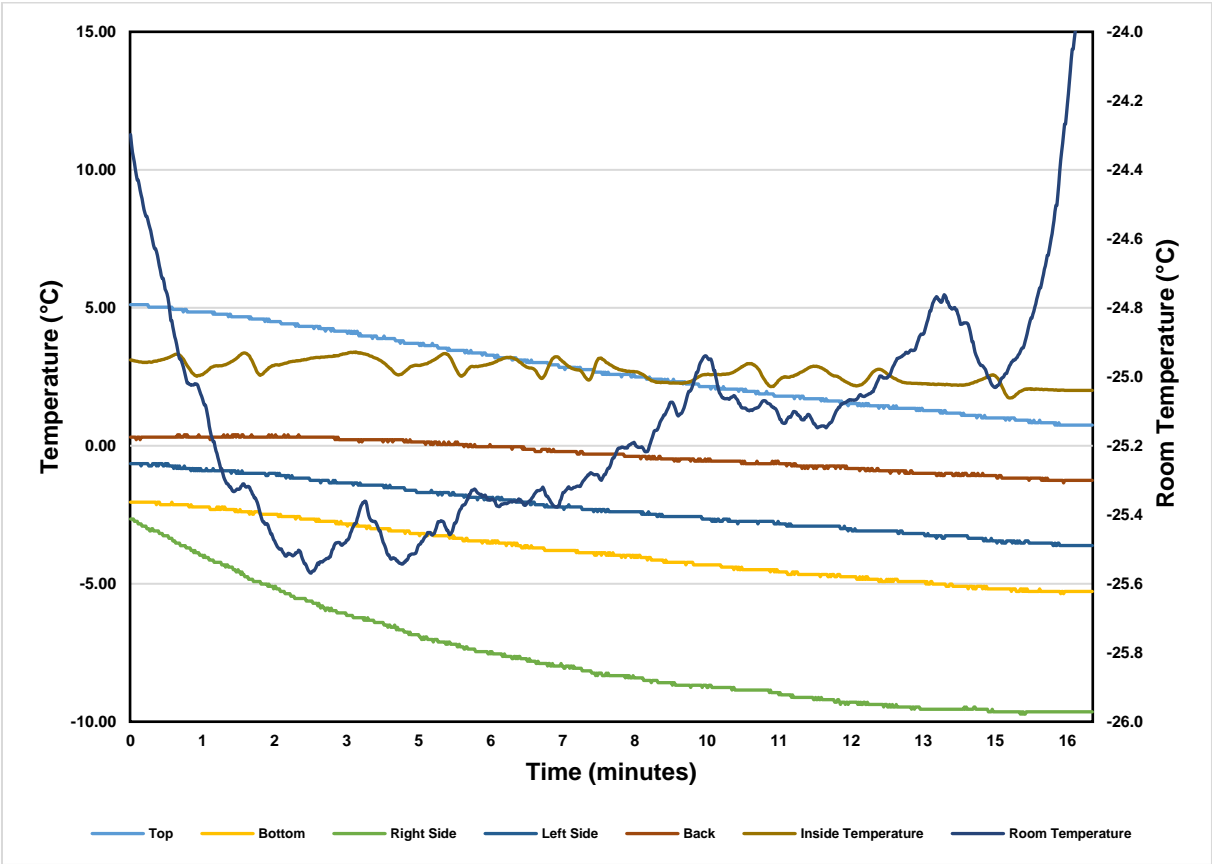


Figure 5.33. The experimental temperature distributions of the inside of the robot for fiberglass thermal insulating material at low temperature.

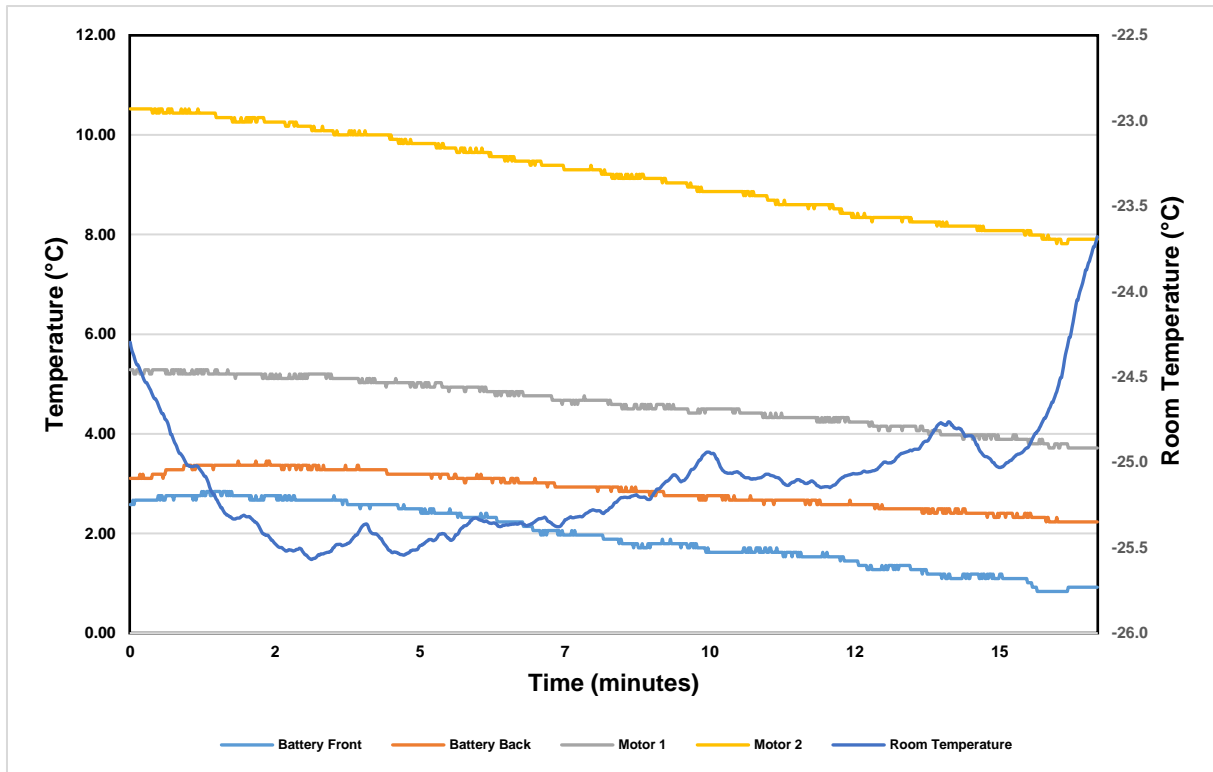


Figure 5.34. The experimental temperature distributions of the battery and the motor of the robot for stone wool thermal insulating material at low temperature.

The heat transfer rates between the robot and ambient conditions are shown in Figure 5.35 with temperature changes of the inside and outside of the robot. When the room temperature is -24.3°C , the heat transfer from the inside to the outside of the robot is 126W . The heat transfer rates change between 126W and 121.8W in 17 minutes. However, the maximum heat transfer rate is obtained as 128.7W in 4 minutes of the experiment. Furthermore, it can be seen that the heat transfer rate decreases corresponding to the decrease of the inside temperature of the robot, but there are still some points that cause to heat transfer rate increases. However, these changes in the heat transfer rates are very low to be considered. On the other hand, the comparison between the inside and outside temperature of the robot can be seen in the secondary Y-axis of Figure 5.35.

The energy and exergy efficiencies of the fiberglass thermal insulating material are defined and showed in Figure 5.36. It can be seen that the energy efficiency of the cover changes just below the 50%. The energy efficiency of the insulating material decreases slightly from 48.33% to 47.39 in 17 minutes. Therefore, it can be indicated that the energy efficiency of the fiberglass is almost constant when the ambient temperature is -25°C . On the other hand, the exergy efficiency of the thermal insulating material is lower than the energy efficiency. The exergy efficiency of the cover decreases from 24.21% to 15.08%. Moreover, the uncertainties for the temperature results of the experiment is seen in Table 5.2.

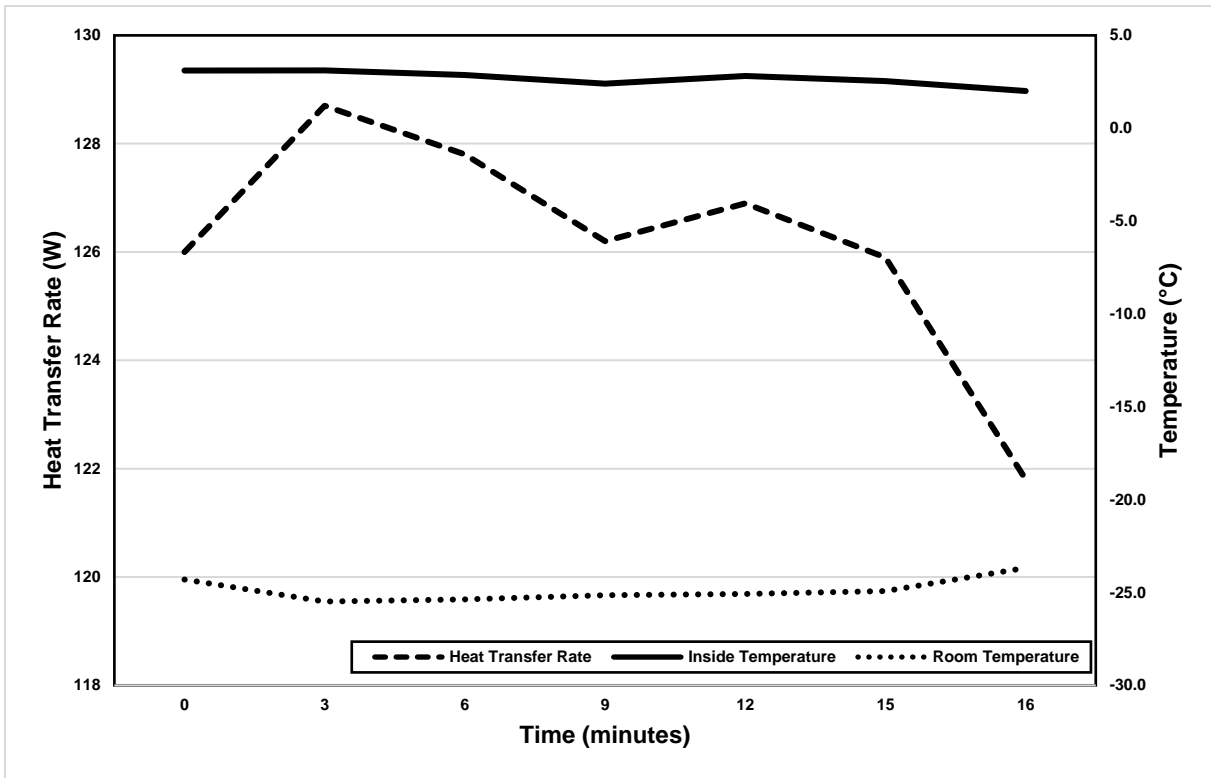


Figure 5.35. The experimental heat transfer rates of the robot for fiberglass insulation at low temperature.

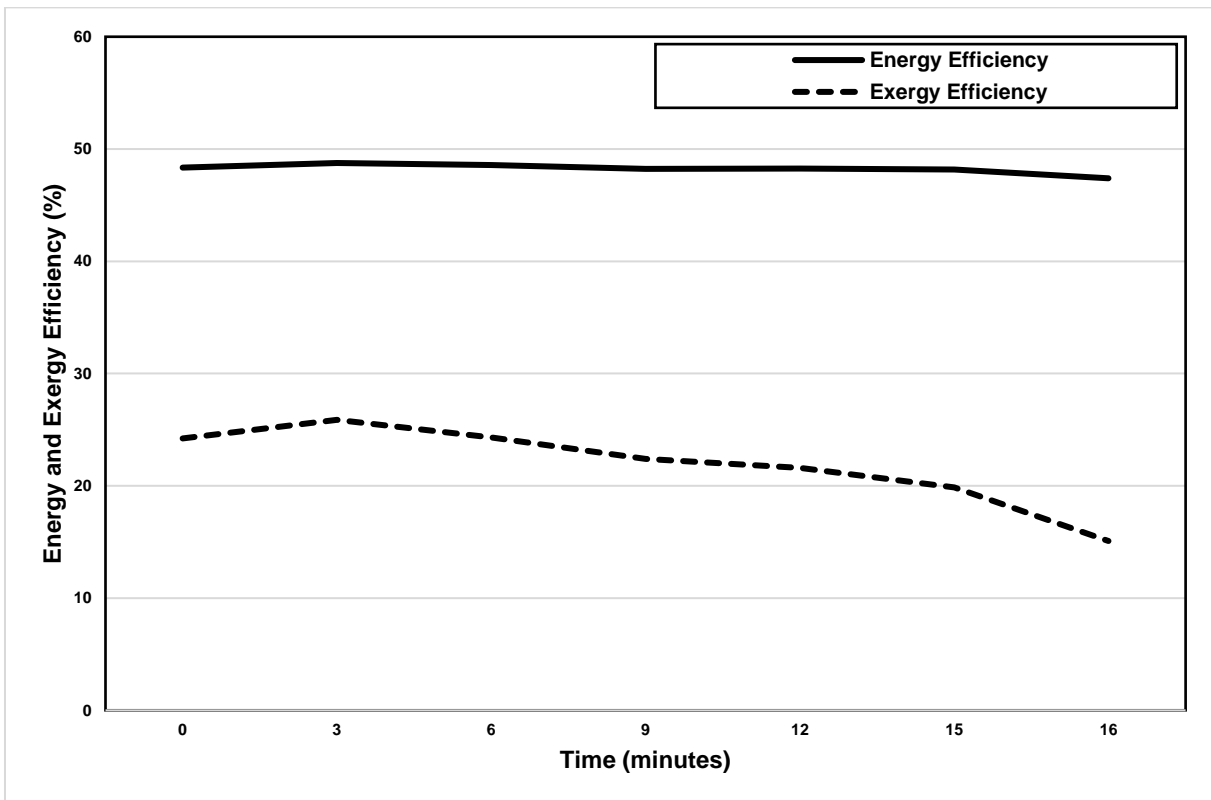


Figure 5.36. The energy and exergy efficiencies of the fiberglass insulating material at low temperature.

Table 5.2. Uncertainties table for the results of fiberglass insulation experiment at low temperature.

Measurement Parameter	Device	Accuracy	
Temperature	Thermocouple K	±0.4%	
Temperature	DAQ	±0.5°C	
Time	Parameter	Value	Total Uncertainties (%)
5	Room Temperature	-25.37±0.2348	0.1837
	Inside Temperature	2.87±0.01148	
	Surface Temperature	-1.87±0.00748	
	Heat Transfer Rate	127.8±0.2348	
10	Room Temperature	-25.16±0.1006	0.1841
	Inside Temperature	2.40±0.009624	
	Surface Temperature	-2.48±0.00992	
	Heat Transfer Rate	126.2±0.2324	
15	Room Temperature	-24.92±0.09968	0.1829
	Inside Temperature	2.53±0.01015	
	Surface Temperature	-3.44±0.01376	
	Heat Transfer Rate	125.9±0.2303	

Figure 5.37 demonstrates the changes in the relative humidity of both the inside of the robot and climatic chamber where the robot is operated in. It can be clearly seen that the relative humidity of the robot decreases gradually from 61.54% to 30.37% in 17 minutes. However, the relative humidity of the room reduces from 94.6% to 56.4% in 15 minutes. Then, the relative humidity of the room increases to just above 95% sharply. Although the relative humidity of the room reaches to 97.5%, the relative humidity of the inside of the robot is recorded as 30.38%.

The change of the surface temperature of the robot with the extruded polyurethane thermal insulating material is demonstrated in Figure 5.38. The robot is tested with the extruded polyurethane cover at -25°C room temperature for 15 minutes. During the experiment, the inside temperature of the robot is obtained from 4.38°C to 1.80°C with some fluctuations. However, the lowest inside temperature of the robot is recorded as 1.39°C. On the other hand, the temperature of the left side of the robot decreases from 0.57°C to -5.45°C, while the surface temperature of the right side declines from -0.64°C to -8.59°C. Therefore, the lowest surface temperature is seen on the right side as -8.59°C at the end of the experiment of extruded polyurethane insulation. The surface temperature of the bottom of the robot reduces from -2.57°C to -5.71°C, while the temperature of the top surface changes between 5.55°C and -1.26°C. Moreover, the surface temperature of the back side of the robot decreases gradually from 1.80°C to -2.05°C. Finally, the temperature of the climatic chamber varies between -25.4°C and -24.4°C.

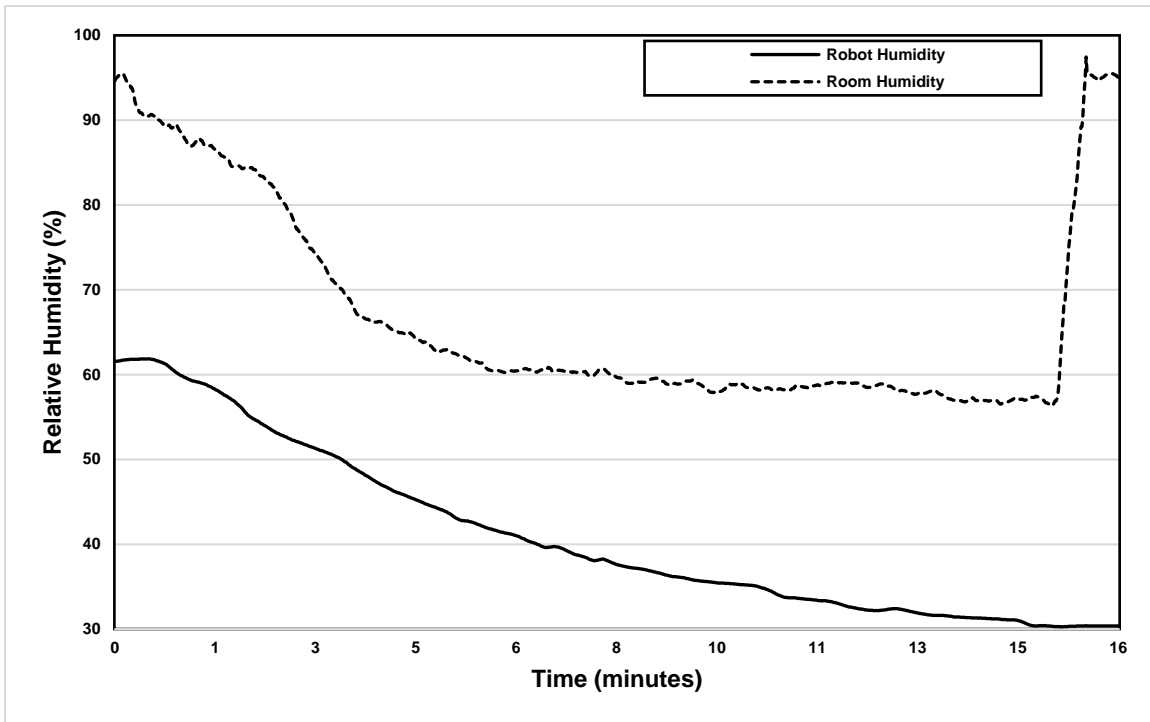


Figure 5.37. The comparison between the relative humidity percentages of the inside and outside of the robot with the fiberglass insulating material at low temperature.

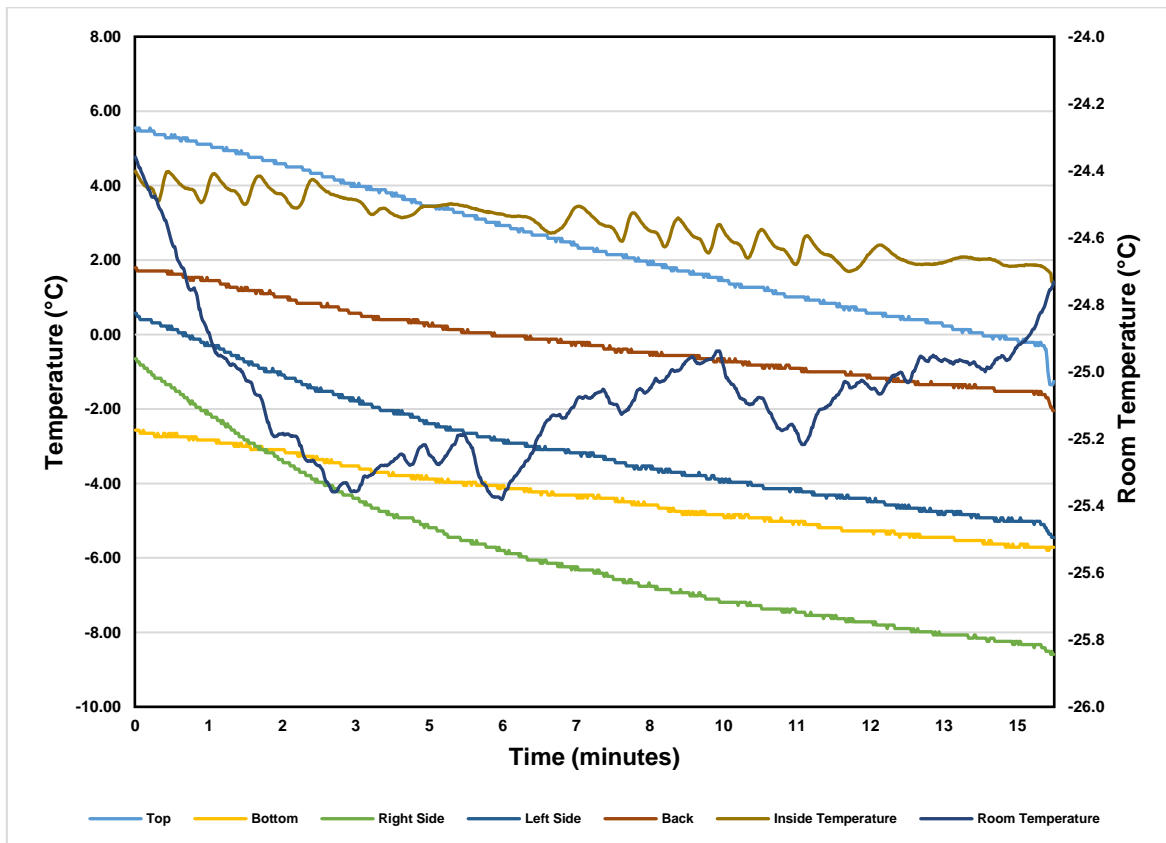


Figure 5.38. The experimental temperature distributions of the inside of the robot for extruded polyurethane thermal insulating material at low temperature.

The collected data of the surface temperature distributions of the battery and motor is shown in Figure 5.39 at low temperature. When the extruded polyurethane thermal insulating material is applied to the robot, the inside temperature decreases from 4.38°C to 1.39°C in 15 minutes. The surface temperature of the front side of the battery reduces dramatically from 2.31°C to -1.52°C, while the temperature of the backside of the battery decreases from 3.45°C to 0.84°C. However, there are two more temperature readings from the motor of the robot. The readings of the point motor 1, which is the metal component of the motor, change between 4.41°C and 2.67°C. The other temperature readings from the motor, which are numbered as 2, are the motor surface that is a plastic component. The temperatures of the point motor 2 decrease from 7.64 °C to 7.38°C, however, the temperature of the motor increases to 8.5°C in 15 minutes.

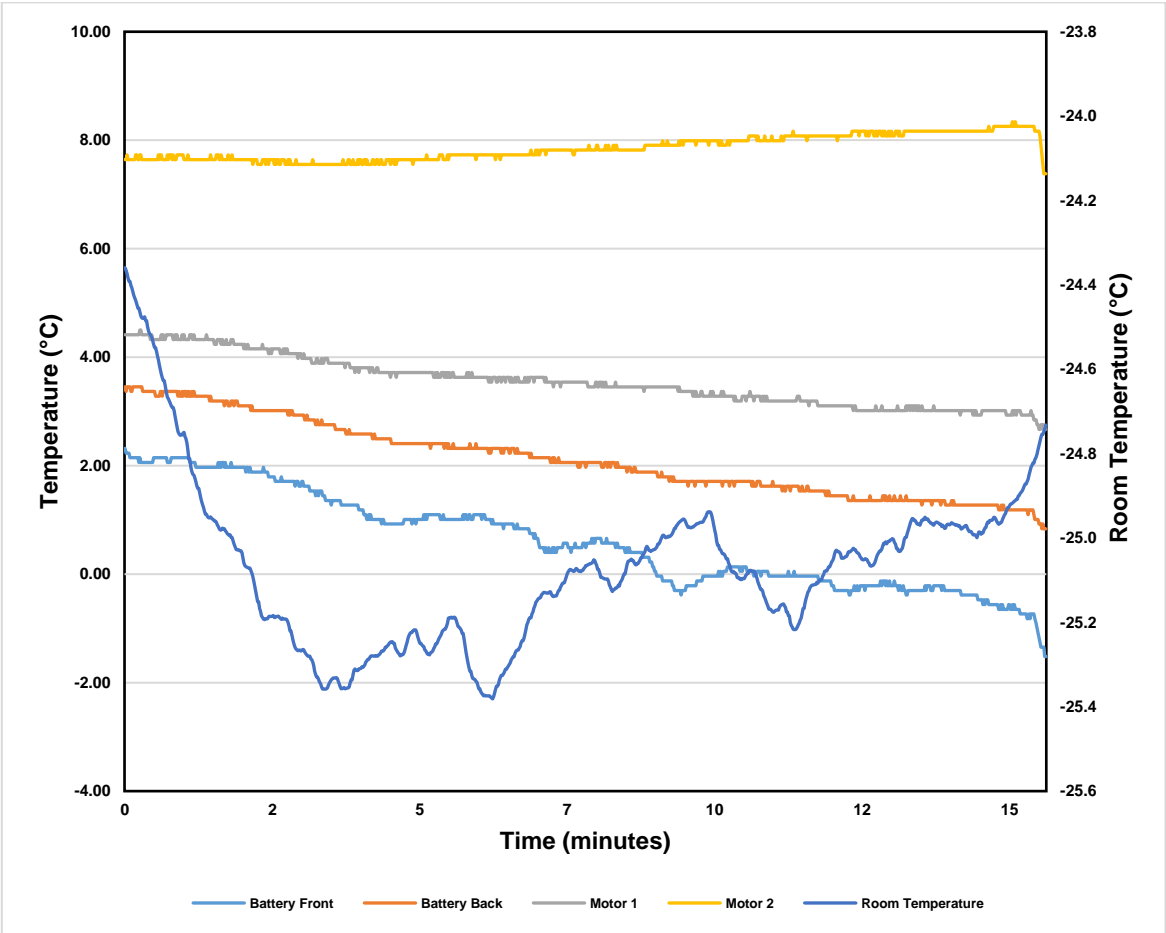


Figure 5.39. The experimental temperature distributions of the battery and the motor of the robot for extruded polyurethane thermal insulating material at low temperature.

The heat transfer rate between the inside of the robot and the climatic chamber is defined for the extruded polyurethane insulating material at low temperature and shown in Figure 5.40. When the inside temperature is 4.38°C and the room temperature is -24.4°C, the heat transfer between the inside and outside of the robot is obtained as 173.9W. In 3 minutes, the heat transfer

rate increases to 176.1W, while the temperatures are 4.16°C for the inside, and -25.3°C for the room. The heat transfer rate decreases gradually to 162.9W in 12 minutes. Therefore, in 15 minutes, the highest heat transfer rate between the inside and outside of the robot is obtained as 177.1W, and the lowest heat transfer rate is 161.3W.

Corresponding to the heat transfer rate between the inside of the robot and outside, the energy efficiencies of the extruded polyurethane thermal insulating material are shown in Figure 5.41. The energy efficiencies of the extruded polyurethane are obtained as just above 30%. The energy efficiency of the material decreases slightly from 31.83% to 30.75%. Therefore, the energy efficiency of the extruded polyurethane is recorded as almost steady. Moreover, the extruded polyurethane cover is also analyzed from the exergy efficiency point of view. In terms of the exergy analyses of the material, the exergy efficiency of the cover goes down from 23.35% to 18.91% at low temperature. The surface temperature is a vital parameter for the exergy analyses and changes between 0.57°C and -5.45°C. Moreover, uncertainties in the temperature recordings of the experiment are seen in Table 5.3.

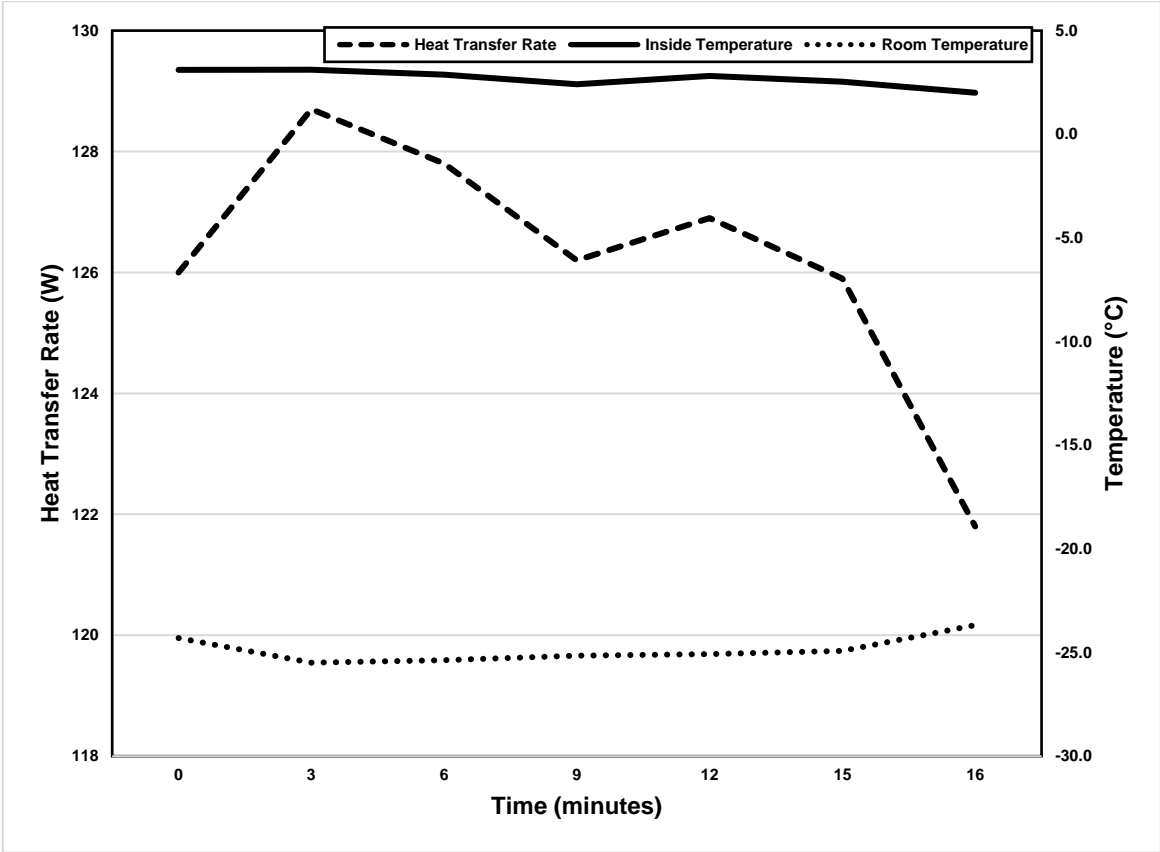


Figure 5.40. The experimental heat transfer rates of the robot for the extruded polyurethane insulation at low temperature.

Table 5.3. Uncertainties table for the results of extruded polyurethane insulation experiment at low temperature

Measurement Parameter		Device	Accuracy
Temperature		Thermocouple K	$\pm 0.4\%$
Temperature		DAQ	$\pm 0.5^\circ\text{C}$
Time	Parameter	Value	Total Uncertainties (%)
5	Room Temperature	-25.36 ± 0.1014	0.2224
	Inside Temperature	3.30 ± 0.01321	
	Surface Temperature	-2.74 ± 0.01109	
	Heat Transfer Rate	173 ± 0.3849	
10	Room Temperature	-25.03 ± 0.1001	0.2254
	Inside Temperature	2.35 ± 0.00984	
	Surface Temperature	-3.70 ± 0.01481	
	Heat Transfer Rate	167.9 ± 0.3785	
15	Room Temperature	-24.92 ± 0.0996	0.2273
	Inside Temperature	1.84 ± 0.00736	
	Surface Temperature	-5.01 ± 0.02005	
	Heat Transfer Rate	165.4 ± 0.376	

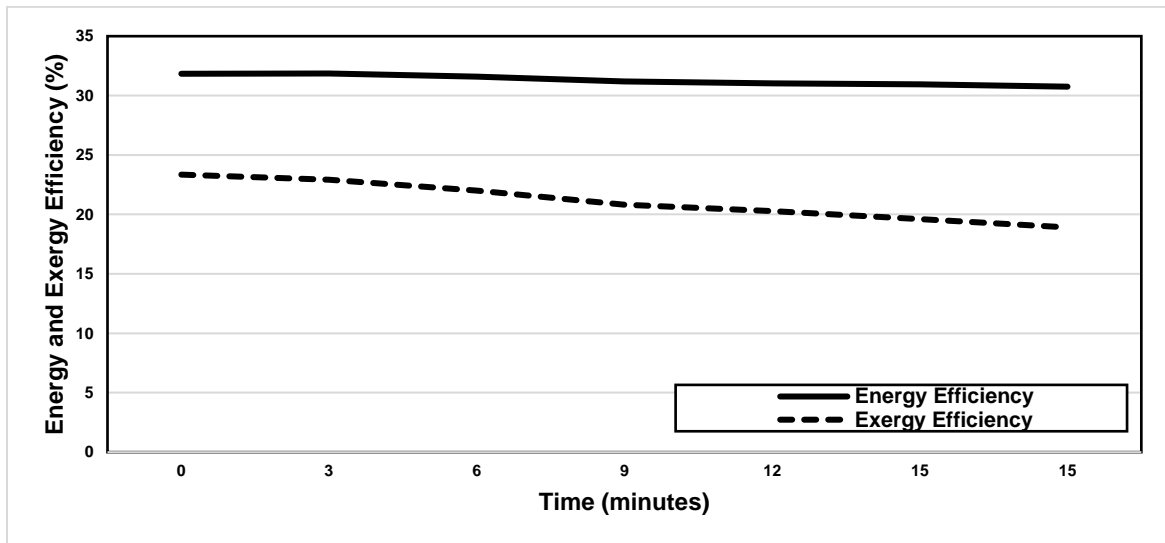


Figure 5.41. The energy and exergy efficiencies of the extruded polyurethane insulating material at low temperature.

In Figure 5.42, the comparison between the relative humidity of the inside and outside of the robot with the extruded polyurethane insulating material is shown at low temperature. It can be seen that the relative humidity content of the inside of the robot is always lower than the relative humidity content of the climatic chamber. The relative humidity content of the inside of the robot decreases moderately from 65.25% to 31.06% in 15 minutes. On the other hand, the relative humidity of the room reduces gradually from 93.1% to 60% in 10 minutes. After that, it can be seen that the relative humidity content of the climatic chamber stays almost constant and reaches 58.9% in 15 minutes.

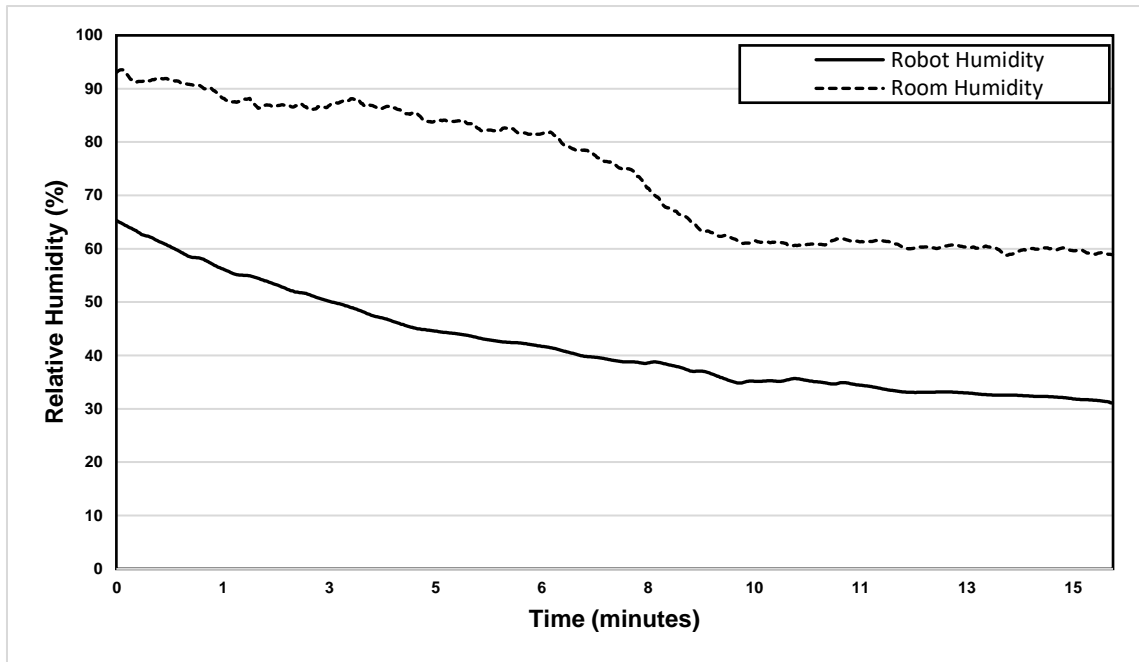


Figure 5.42. The comparison between the relative humidity percentages of the inside and the outside of the robot with the extruded polyurethane insulating material at low temperature.

When the air heating thermal management is operated inside the robot, the temperature distributions on the different surfaces of the robot are given in Figure 5.43. During the experiment of the air heating thermal management system, the fiberglass thermal insulating material is also applied to the robot. The air heating process is run at 7 bar air pressure. It can be clearly seen that there is a moderate increase on all the surfaces of the robot and for the inside temperatures as well. The inside temperature of the robot increases gradually from 3.67°C to 11.78°C in 32 minutes. On the other hand, the initial temperature of the right side of the robot is the lowest recorded temperature during the testing. The surface temperature of the right side of the robot rises considerably from -7.13°C to 3.69°C, while the temperature of the left side varies between -3.34°C and 5.22°C.

However, the surface temperatures at the bottom of the robot increase significantly from -5.79°C to 1.54°C. Comparing to the surface temperature of the bottom, the top surface temperatures of the robot change between -2.63°C and 2.69°C. On the other hand, the temperature of the backside of the robot increases from -1.50°C to 4.61°C. Moreover, the temperature of the climatic chamber varies between -25.4°C and -24.6°C during the experiment for the air heating thermal management system in 32 minutes. It can be easily seen, in Figure 5.43, that temperatures of all the surfaces increase when the air heating thermal management system is operated.

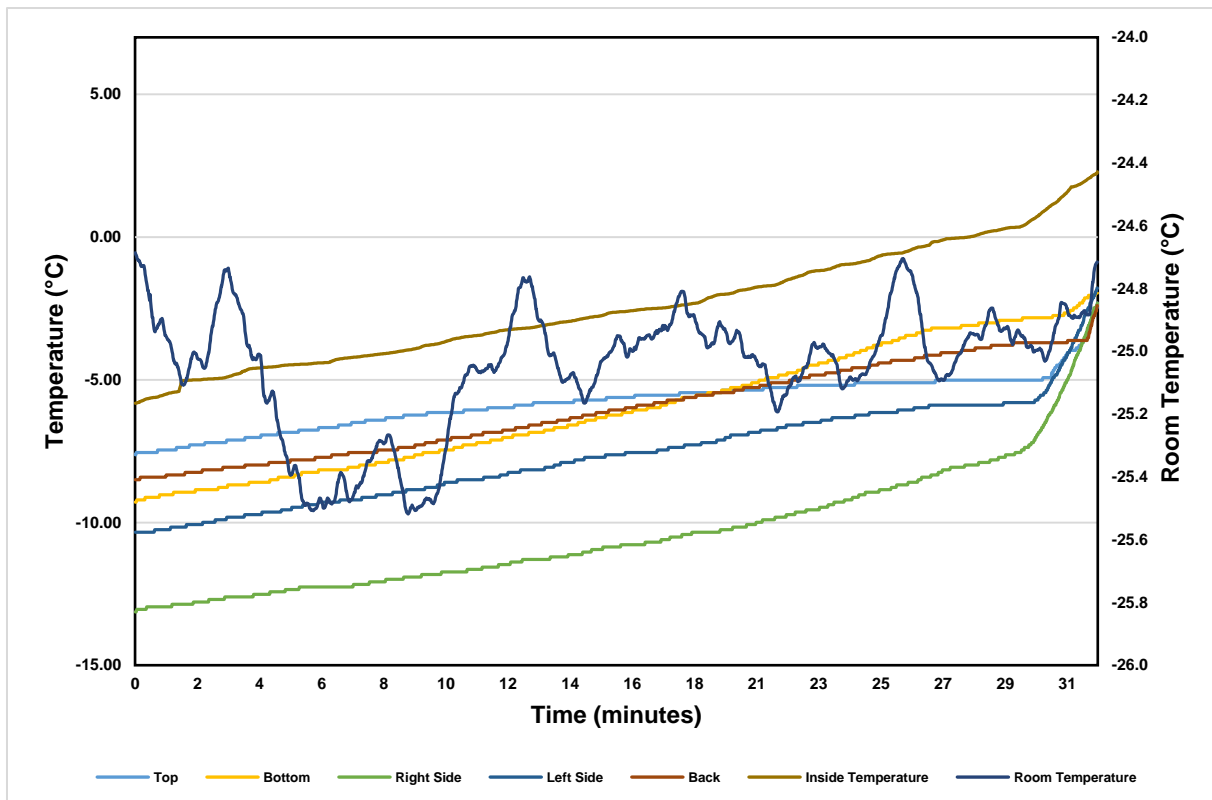


Figure 5.43. The experimental temperature distributions of the inside of the robot with the air heating thermal management system at low temperature.

Figure 5.43 shows the change in the surfaces temperatures of the battery and motor at low temperature to obtain the thermal performance of the air heating thermal management system. The surface temperatures of the front side of the battery increase from 2.25°C to 7.22°C, while the temperatures of the backside of the robot change between 3.82°C and 7.75°C. On the other hand, the temperature recordings from one of the surfaces of the motor rise from 5.57°C to 9.23°C in 32 minutes. Moreover, the temperature reading from the second surface of the motor also increases gradually from 8.49°C to 11.11°C.

In Figure 5.45, the total heating power providing by the air heating thermal management system is analyzed to obtain its change during the experiment. Moreover, Figure 5.45 also compares the inside and outside of the robot. It can be seen from the graph that the heating power of the thermal management system increases from 312.4W to 331.3W in 12 minutes. However, the heating power reduces sharply to 219W in the following 20 minutes. On the other hand, the increase of the initial temperature while the heating process can be seen as from 3.67 °C to 11.78°C in 32 minutes, while the room temperature changes around -25°C.

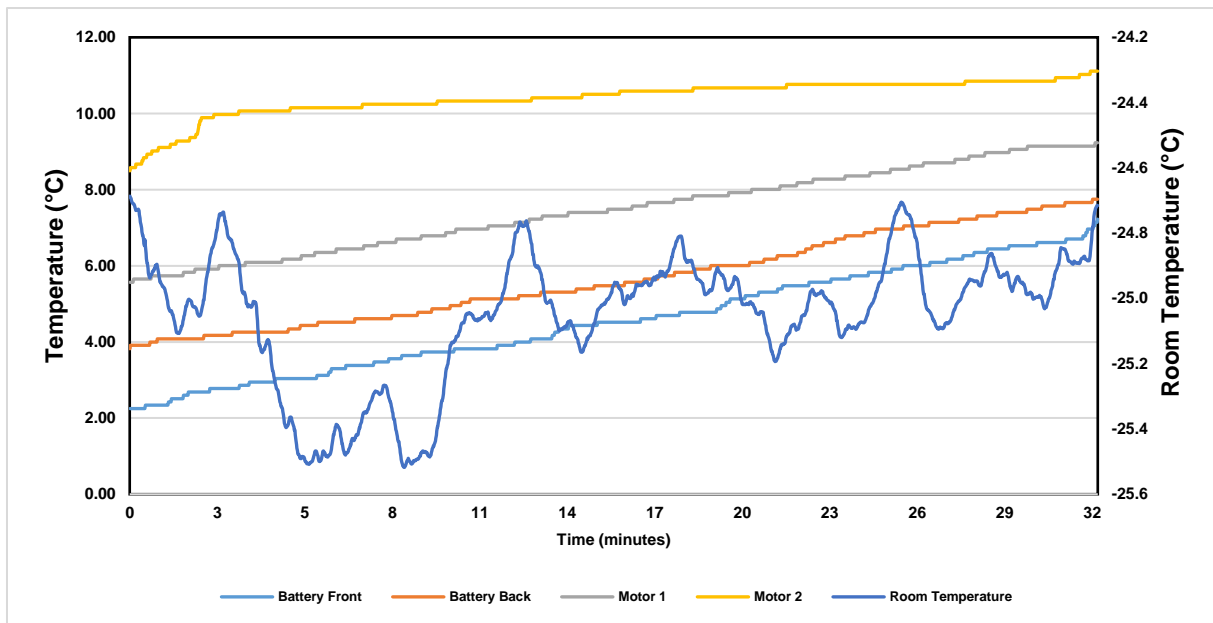


Figure 5.44. The experimental temperature distributions of the battery and motor of the robot for the air heating thermal management system at low temperature.

The energy and exergy efficiencies of the air heating thermal management are analyzed and shown in Figure 5.46. The energy efficiency of the thermal management system increases from 28.4% to 30.12% in the first 12 minutes. However, as a reason of the decrease of the heating power of the thermal management system, the energy efficiency reduces to 19.91% in 20 minutes. On the other hand, when the performance of the air heating thermal management system is analyzed from an exergy point of view, it can be seen that the exergy efficiency of the system is very low and stays just above the 5% during the operation. The exergy efficiency of the thermal management system increases to 3.86% from 3.51%, and then it reduces to 3.14% after 12 minutes.

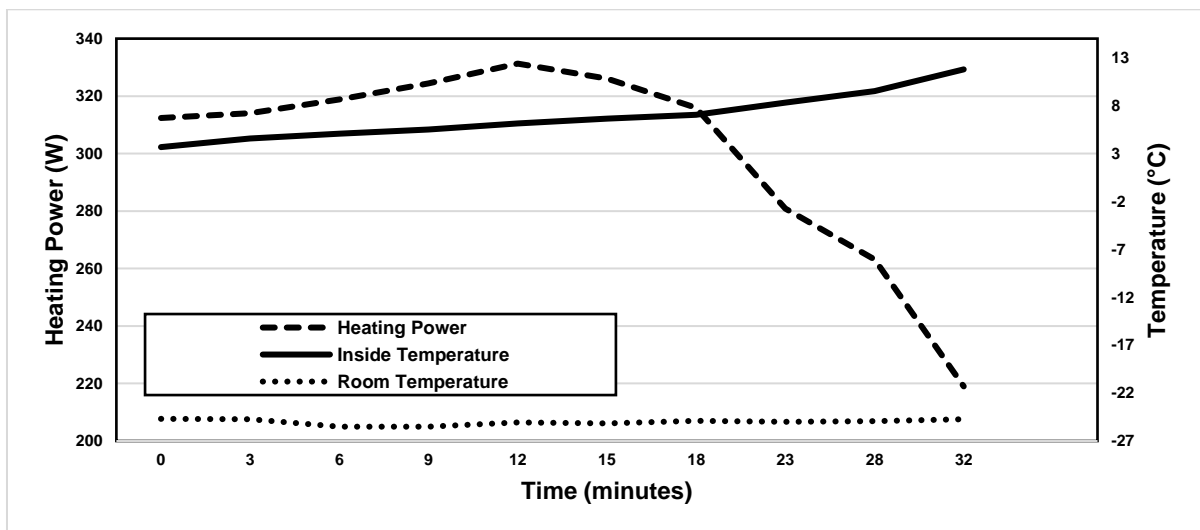


Figure 5.45. The experimental heat transfer rates of the robot for the extruded polyurethane insulation at low temperature.

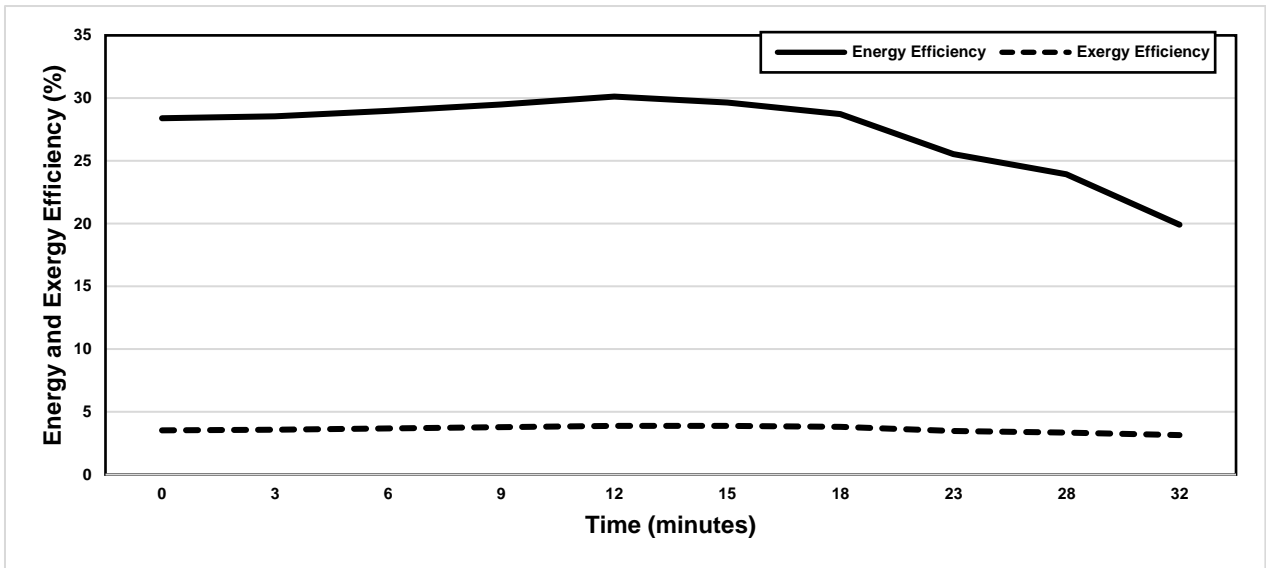


Figure 5.46. The energy and exergy efficiencies of air heating thermal management system at low temperature.

Finally, Figure 5.47 compares the inside and outside of the robot in terms of the relative humidity contents when the air heating thermal management system is taken place. There is no doubt that the relative humidity of the inside of the robot decreases from 56.14% to 11.97% as a reason of the increasing inside temperature of the robot. In 3 minutes, there is a sharp drop of the relative humidity content for both the inside and outside of the robot. On the other hand, the relative humidity of the climatic chamber reduces from 88.75% to 56.4% in 32 minutes.

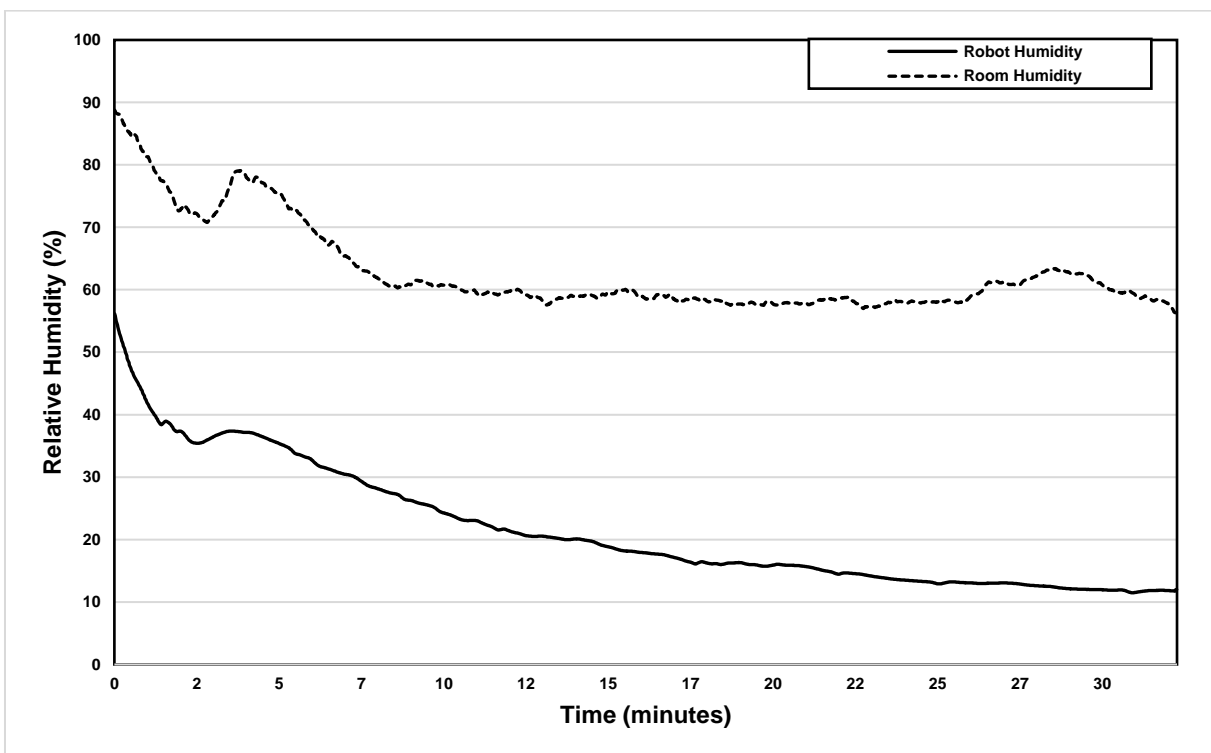


Figure 5.47. The comparison between the relative humidity percentages of the inside and outside of the robot with air heating thermal management system at low temperature.

5.2.2. Experimental Results at High Temperature

The second part of the experiment is for the testing of the thermal management materials and the system at high temperature. The temperature of the climatic chamber is adjusted to 40°C for the experiment. Stone wool, fiberglass, extruded polyurethane covers, air cooling thermal management system, and robot are tested at the high temperature, respectively. In Figure 5.48, the surface temperature distributions of the inside of the robot are demonstrated when the robot is operated with the stone wool thermal insulating material. The surface temperature of the bottom of the robot increases from 23.09°C to 24.84°C in 15 minutes, however, the temperature of the top surface of the robot varies between 28.24°C and 29.29°C. The highest surface temperature on the robot is obtained for the right side of the robot, which increases from 28.33% to 31.12%. On the other hand, the surface temperatures of the left side rise from 26.66°C to 27.72°C in 15 minutes. Moreover, the inside temperature of the robot increases slightly from 23.96°C and 25.81°C, while the temperature of the backside varies between 26.32°C and 27.11°C.

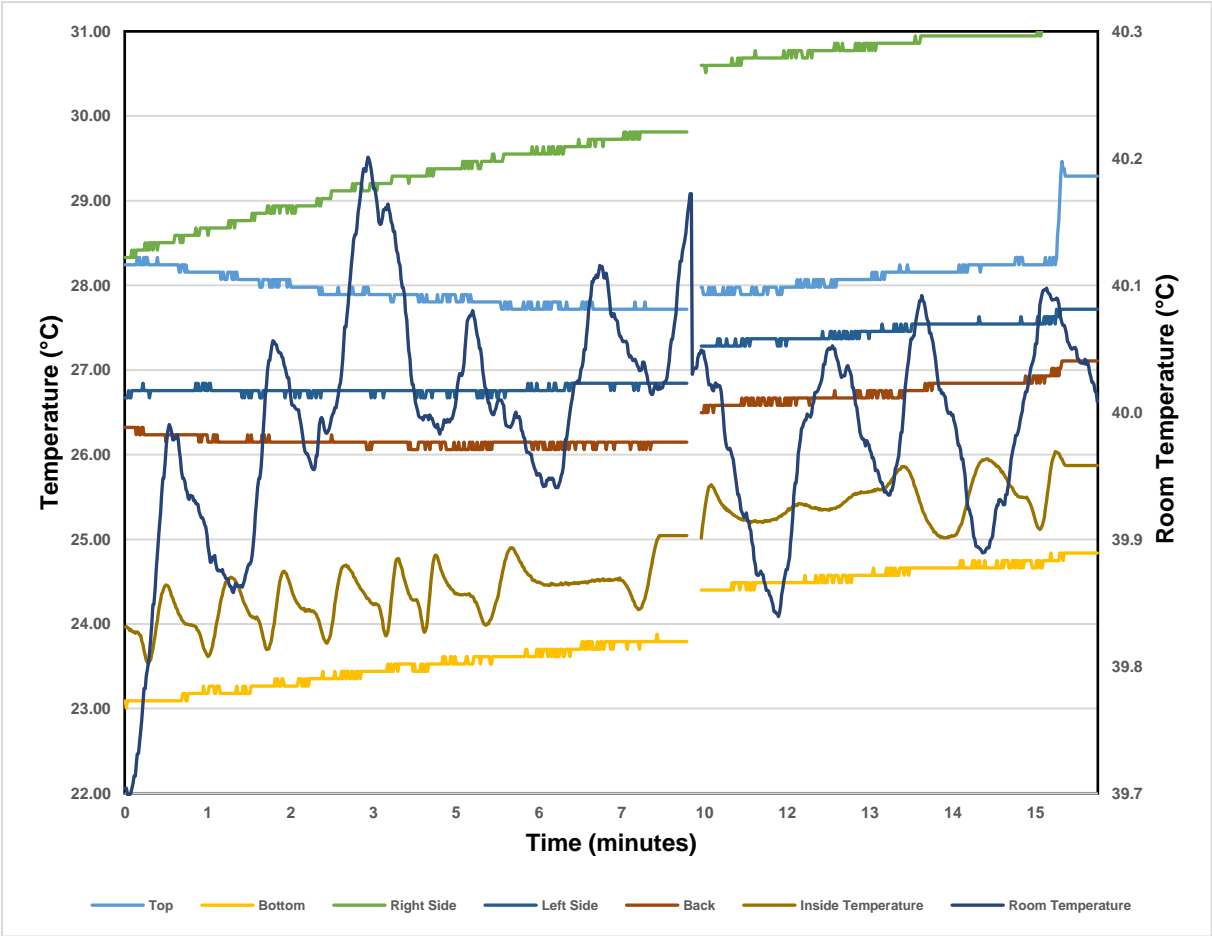


Figure 5.48. The experimental temperature distributions of the inside of the robot for stone wool thermal insulating material at high temperature.

However, Figure 5.49 shows the surface temperature changes of the battery and motor of the robot when the stone wool thermal insulating material is applied to the robot at 40°C room temperature. The surface temperatures of the battery are recorded from two sides, which are the front and back of the battery. The temperature of the front side of the battery increases slightly from 20.12°C to 21.21°C. On the other hand, the temperature of the backside of the battery rises from 19.42°C to 20.91°C in 15 minutes. Moreover, the temperature of the motor rises from 24.75°C to 26.50°C on the metal surface of the motor, and the second temperature reading from the plastic surface temperature of the motor goes up from 28.32°C to 30.86°C. Finally, the temperature of the room during the experiment varies between 39.7°C and 40.13°C.

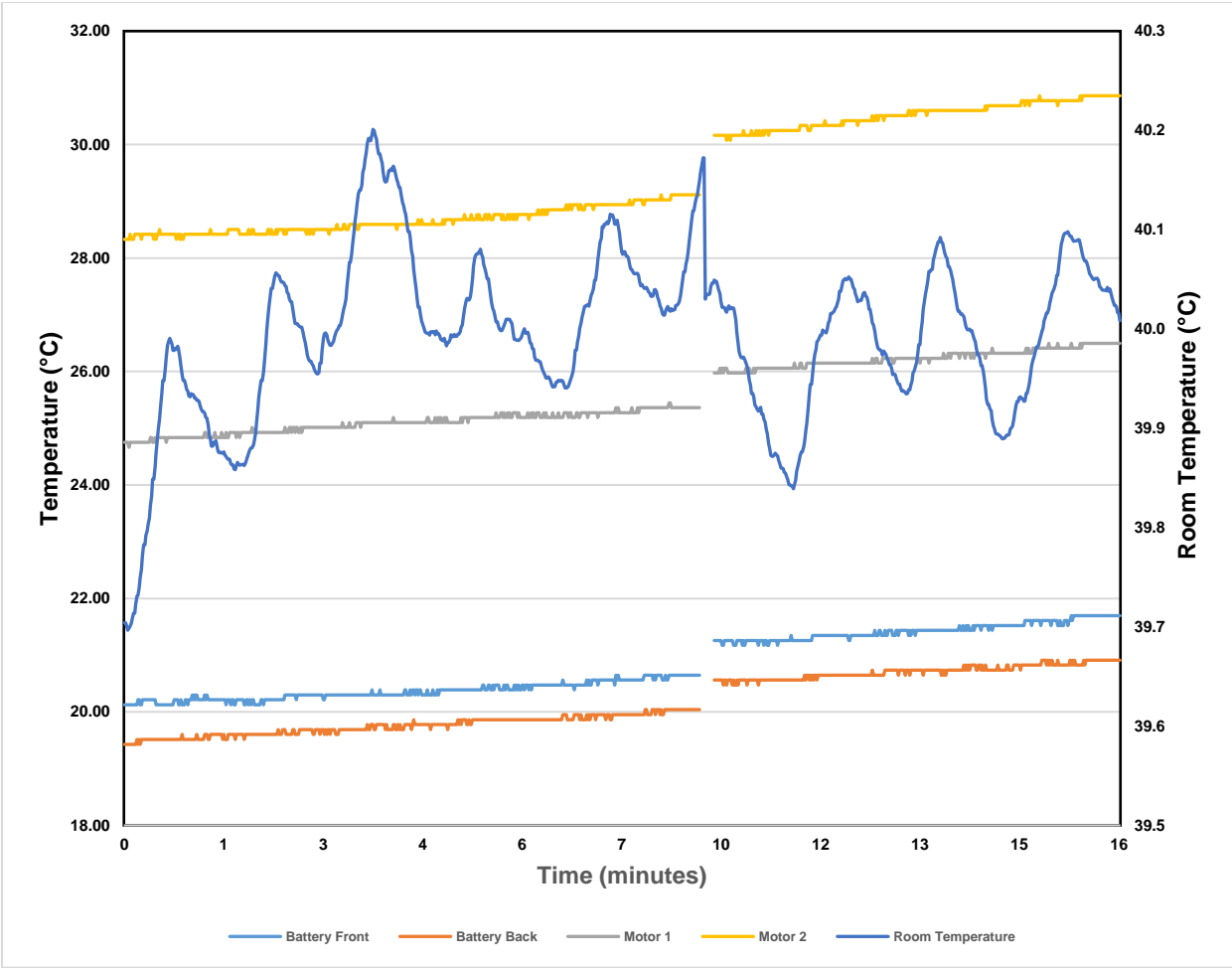


Figure 5.49. The experimental temperature distributions of the battery and motor of the robot for stone wool insulating material at high temperature.

Figure 5.50 demonstrates the heat transfer rate between the inside and outside of the robot with stone wool insulating material at 40°C room temperature. It can be seen that the room temperature stays almost constant at 40°C during the experiment in 16 minutes. However, the 15°C difference between the outside and inside of the robot is also remarkable in Figure 5.49. In three minutes, the heat transfer rate increases slightly from 97W to 98.5W and reaches

98.48W in 6 minutes. After that, the heat transfer rate decreases rapidly from 98.86W to 94.86W in three minutes. After 6 minutes, the heat transfer rate through the surface of the robot reaches to 93.43W.

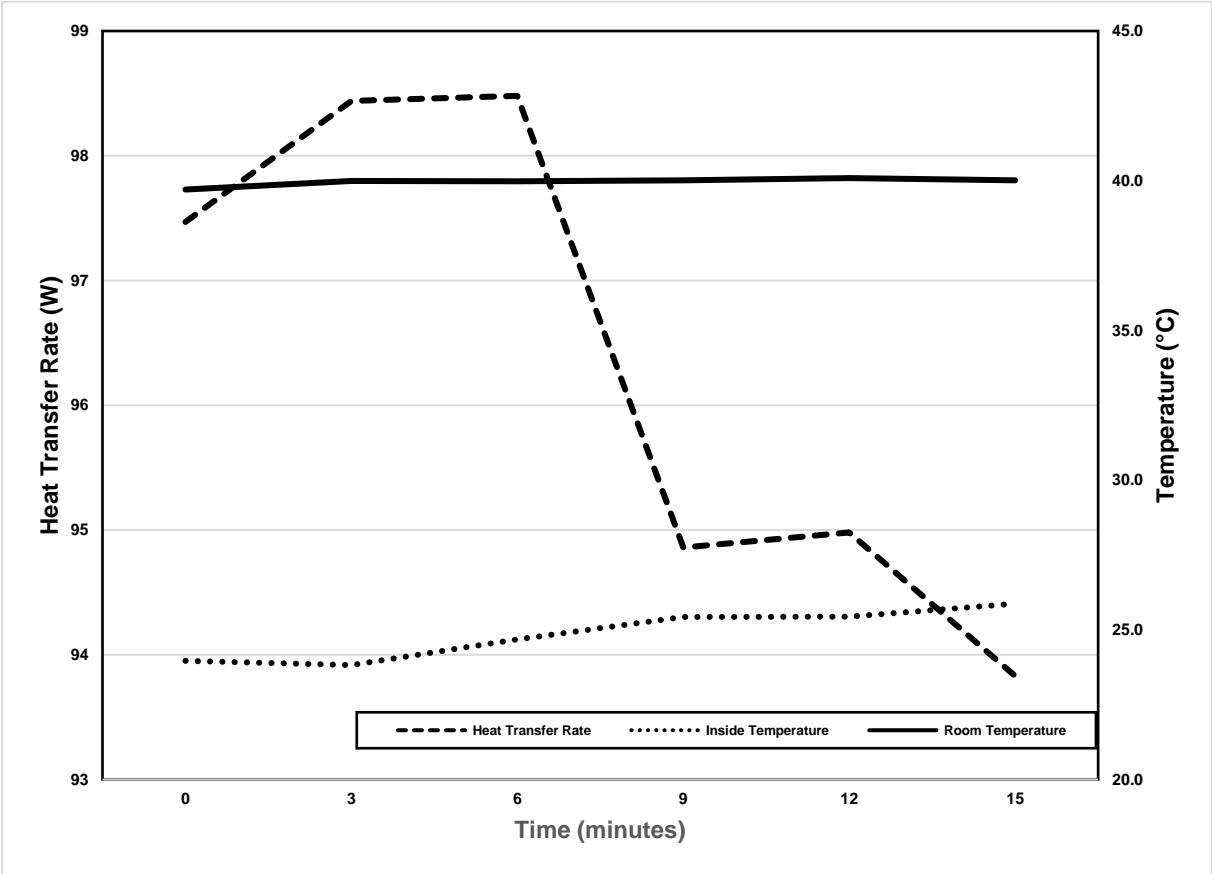


Figure 5.50. The experimental heat transfer rates of the robot for the stone wool insulating material at high temperature.

The energy and exergy efficiencies of the stone wool thermal insulating material are analyzed and shown in Figure 5.50. There is no doubt that the energy efficiency is higher than the exergy efficiency during the experiment in 15 minutes. The energy efficiency of the stone wool thermal insulating material decreases from 48% to 46.34%, when the room temperature changes around 40°C. On the other hand, the exergy efficiency of the stone wool thermal insulating material varies between 30% and 20% in 15 minutes. The exergy efficiency increases slightly from 24.86% to 25.84% in 3 minutes. The exergy efficiency of the thermal insulating material declines to 21.32% in 12 minutes. As it is discussed before, the changes in the energy and exergy efficiencies are related to the variation of the heat transfer rate between the inside and outside of the robot. Moreover, the uncertainties for the temperature results of the experiment are seen in Table 5.4.

Table 5.4. Uncertainties table for the results of stone wool insulation experiment at high temperature

Measurement Parameter		Device	Accuracy
Temperature		Thermocouple K	±0.4%
Temperature		DAQ	±0.5°C
Time	Parameter	Value	Total Uncertainties (%)
5	Room Temperature	39.99±0.1599	0.4461
	Inside Temperature	24.68±0.0987	
	Surface Temperature	26.76 ±0.107	
	Heat Transfer Rate	96.48±0.4304	
10	Room Temperature	40.02±0.1601	0.4576
	Inside Temperature	25.43±0.1017	
	Surface Temperature	27.28 ±0.1091	
	Heat Transfer Rate	94.85±0.4341	
15	Room Temperature	40.01±0.16	0.4649
	Inside Temperature	25.87±0.1035	
	Surface Temperature	27.72 ±0.1109	
	Heat Transfer Rate	93.81±0.4362	

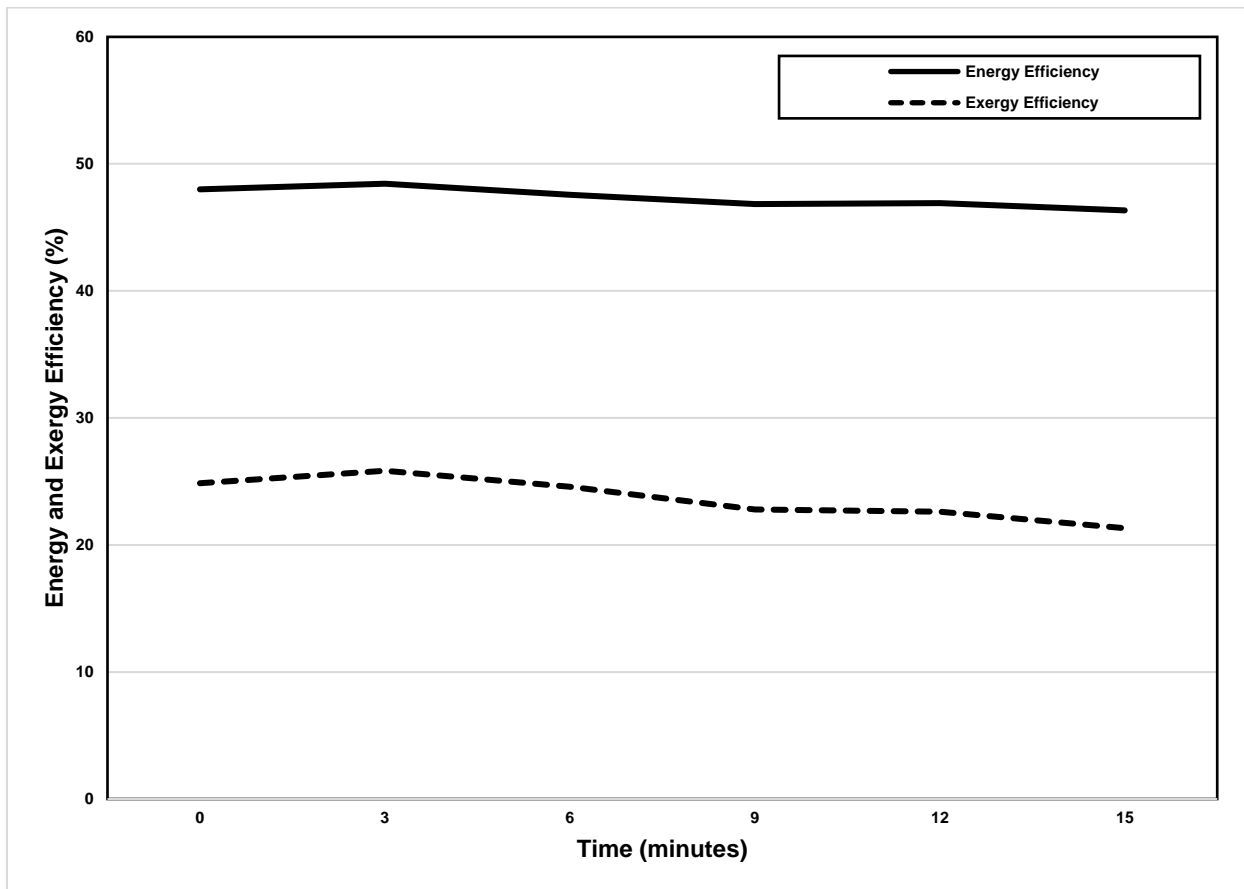


Figure 5.51. The energy and exergy efficiencies of the stone wool insulating material at high temperature.

Figure 5.52 compares the inside and outside of the robot in terms of the relative humidity contents. It can be seen that the relative humidity content of the robot decreases gradually from 11.46% to 5.08%, while the relative humidity content of the climatic chamber is lower than the inside of the robot and stays almost constant at 1.6%.

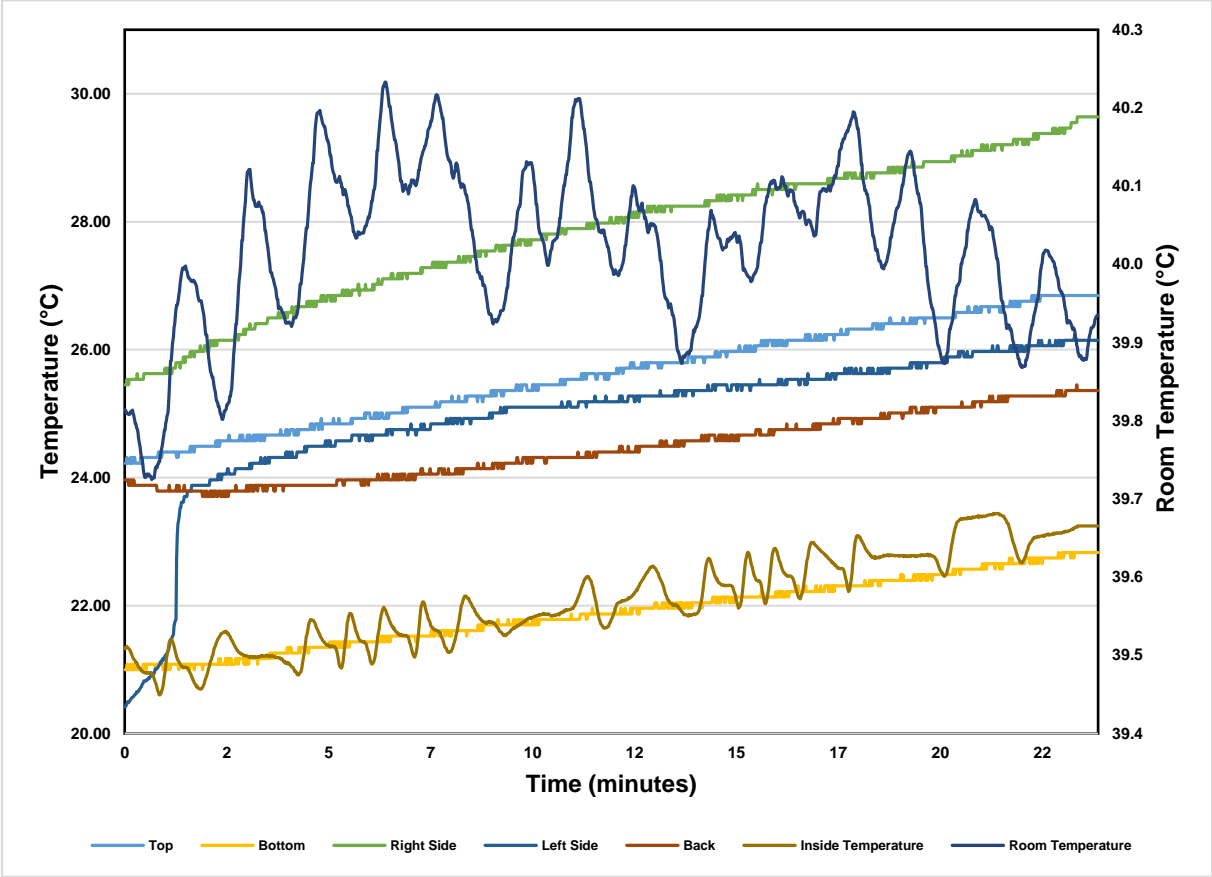


Figure 5.52. The comparison between the relative humidity percentages of the inside and outside of the robot with the stone wool insulating material at high temperature.

The surface temperature distributions of the robot with the fiberglass thermal insulating material are recorded and shown in Figure 5.53. The room temperature during the experiment varies between 39.8°C and 40.21°C in 23 minutes. However, the inside temperature of the robot increases from 21.32°C to 23.24°C, while the surface temperature of the backside of the robot changes between 23.96°C and 25.36°C. On the other hand, the highest surface temperature is seen on the right side of the robot, which raises from 25.45°C to 29.64°C. Comparing to the right side, the surface temperatures of the left side of the robot go up from 20.41°C to 26.15°C. Moreover, the surface temperature increases on the bottom of the robot, which is obtained from 21°C to 22.83°C, while the surface temperature of the top of the robot varies between 24.23°C and 26.65°C.

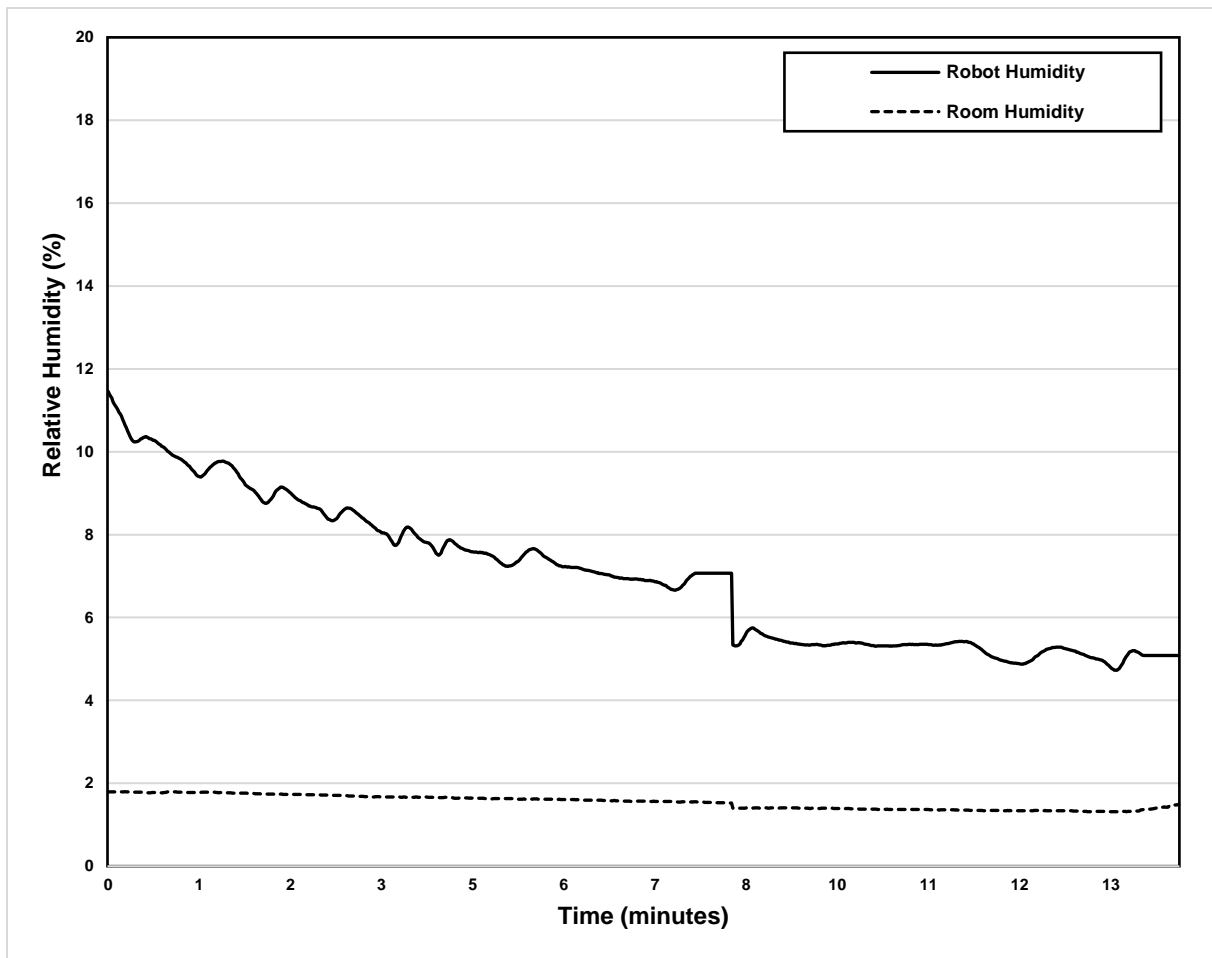


Figure 5.53. The experimental temperature distributions of the inside of the robot for the fiberglass thermal insulating material at high temperature.

In Figure 5.54, the change of the surface temperatures of the battery and the motor, at a high temperature, are demonstrated by time. The temperature increase of the front surface of the battery can be seen from 17.41°C to 19.16°C. However, the temperature of the back side of the battery increases slightly from 17.41°C to 18.55°C. On the other hand, the temperature readings of the motor are recorded from two different points. The first temperature data from the motor is collected from the metal surface of the robot, which rises from 22.31°C to 23.79°C. Finally, the temperature data recordings of the motor surface that is a plastic component increases from 24.49°C to 27.98°C.

Figure 5.55 shows the heat transfer rate between the inside and outside of the robot in 24 minutes at high temperature when the fiberglass thermal insulating material is applied on the robot. The heat transfer rate increases from 107.8W to 109W in three minutes. The heat transfer rate begins to decrease and reaches 103.7W in 20 minutes. The temperature difference between the inside and outside can be seen as almost 18°C.

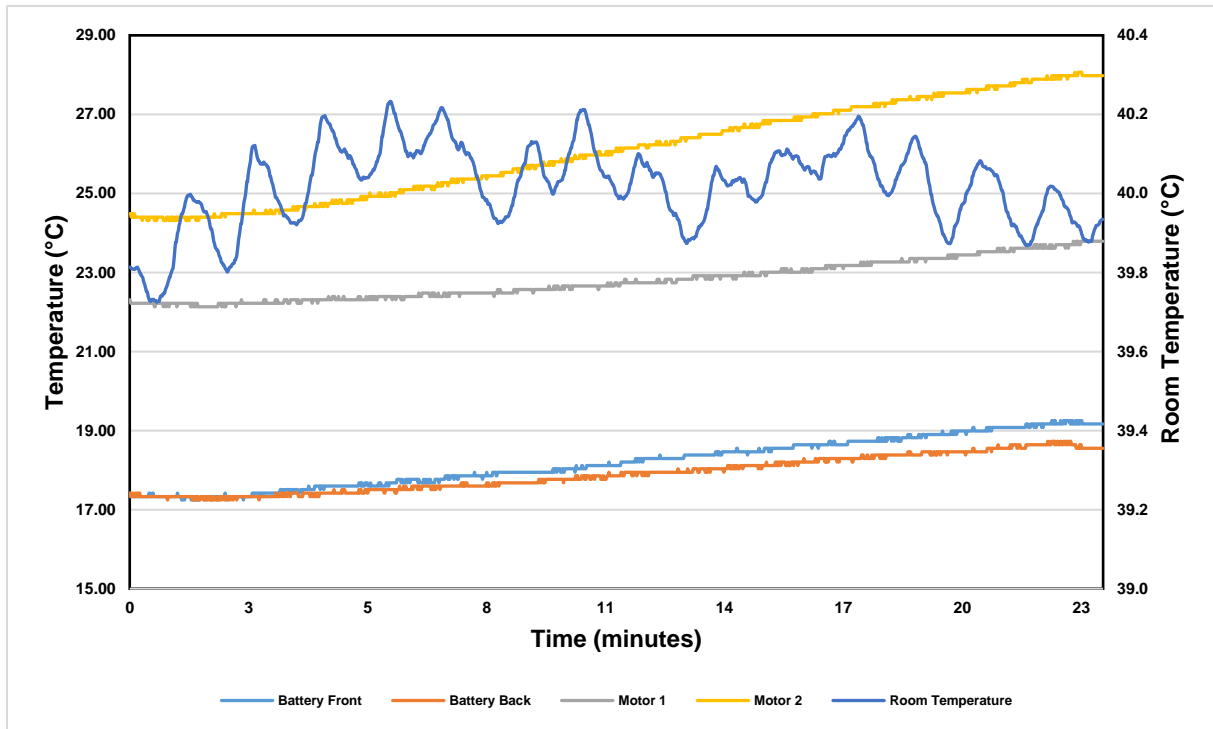


Figure 5.54. The experimental temperature distributions of the battery and motor of the robot for the stone wool insulating material at high temperature.

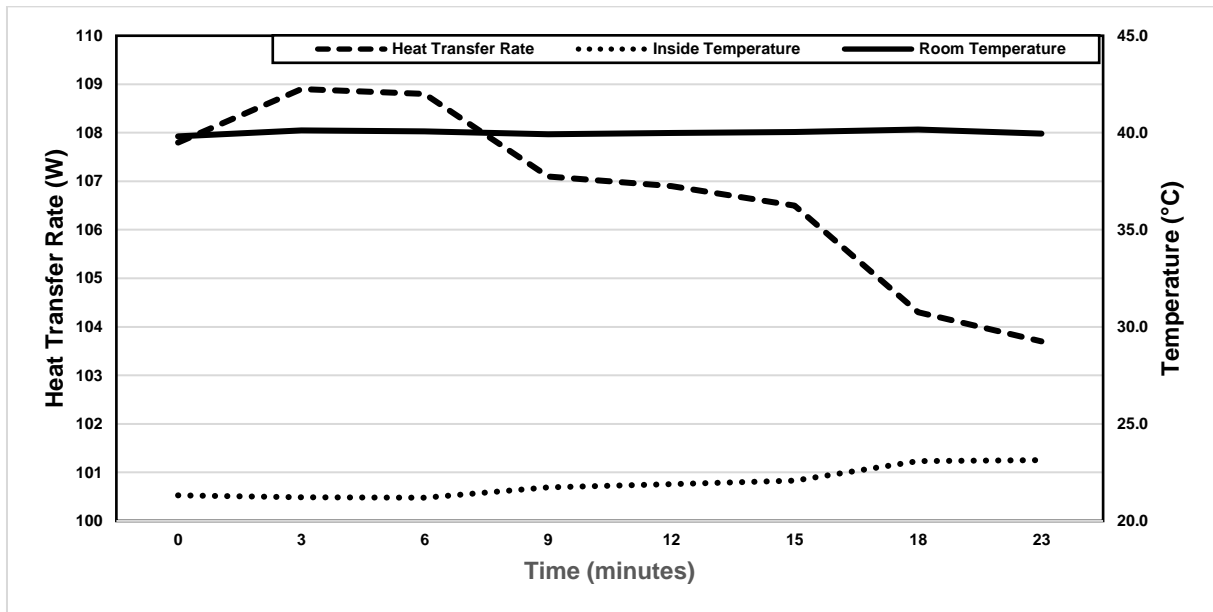


Figure 5.55. The experimental heat transfer rates of the robot for the fiberglass insulating material at high temperature.

The relative humidity of the inside of the robot and the climatic chamber are compared in Figure 5.57 when the temperature of the climatic chamber is 40°C, and the robot is thermally protected by the fiberglass thermal insulating material. It can be easily seen that the relative humidity content of the inside of the robot decreases quickly from 21.32% to around 7% in 11

minutes at high temperature. After that, the relative humidity of the inside reduces slightly from 7.23% to 6.01% in 21 minutes. However, the relative humidity of the inside of the robot stays almost constant just above 6% until the end of the experiment. On the other hand, the relative humidity of the climatic chamber is recorded as almost constant at 1.8%.

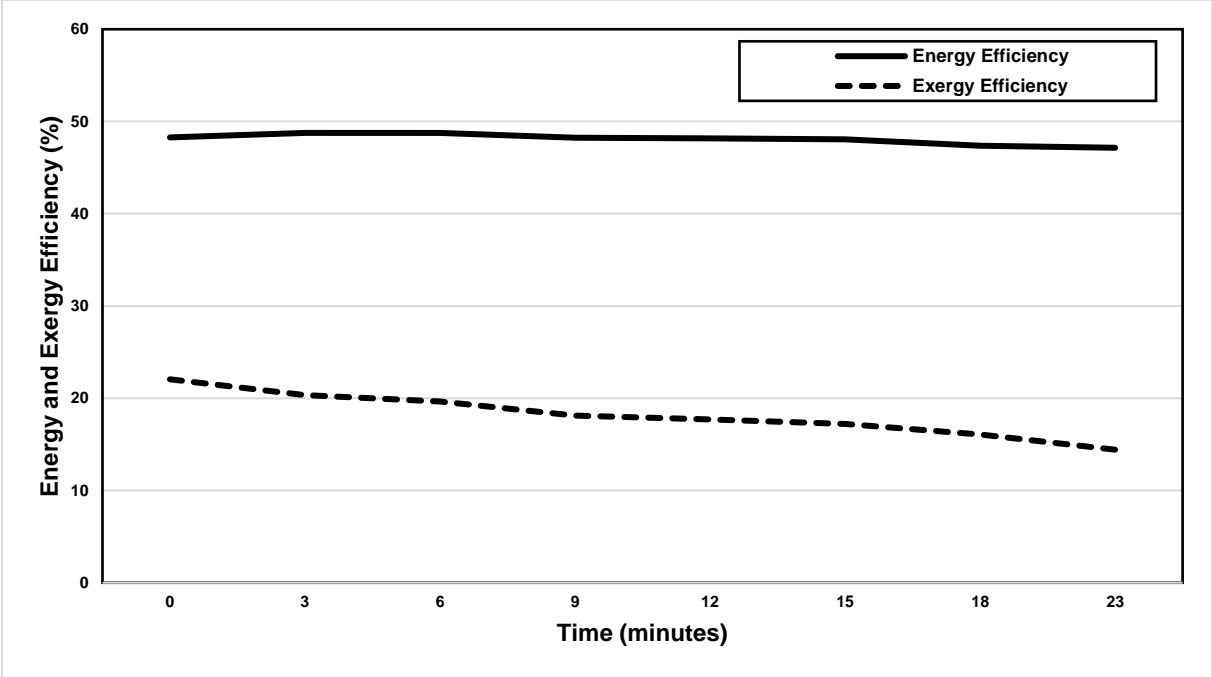


Figure 5.56. The energy and exergy efficiencies of the fiberglass insulating material at high temperature.

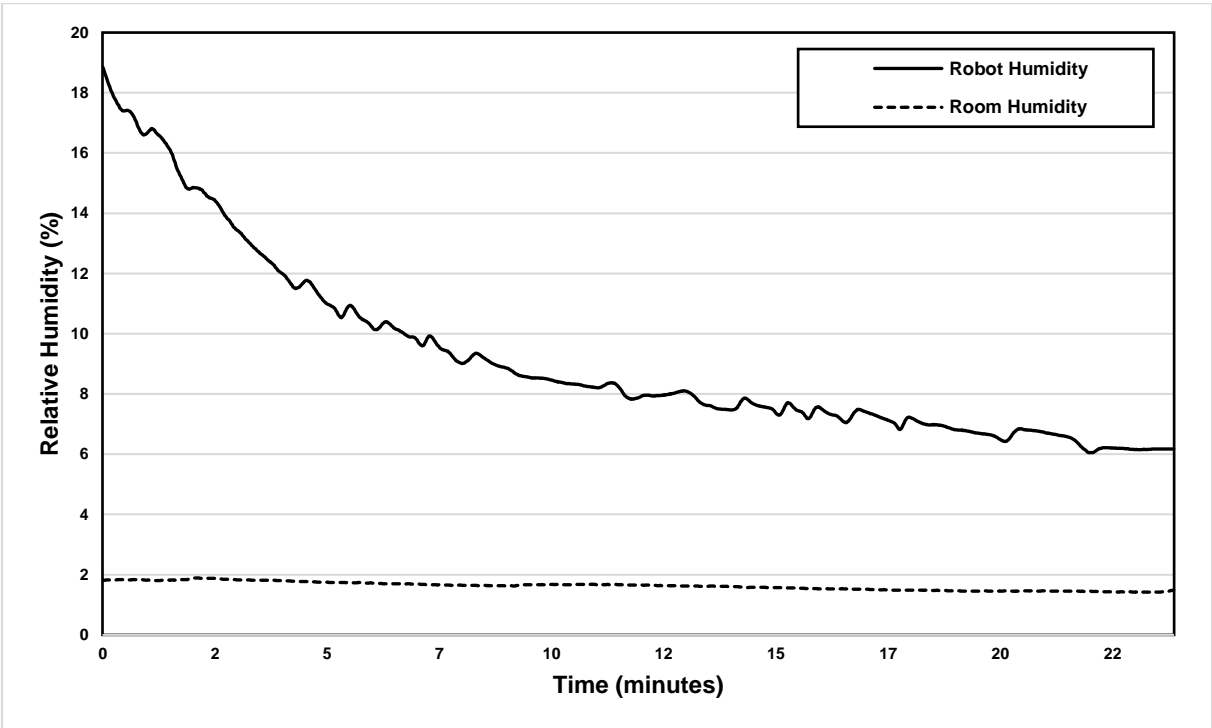


Figure 5.57. The comparison between the relative humidity percentages of the inside and outside of the robot with the fiberglass insulating material at high temperature.

Table 5.5. Uncertainties table for the results of fiberglass insulation experiment at high temperature

Measurement Parameter	Device	Accuracy	
Temperature	Thermocouple K	±0.4%	
Temperature	DAQ	±0.5°C	
Time	Parameter	Value	Total Uncertainties (%)
5	Room Temperature	40.06±0.1603	0.4197
	Inside Temperature	21.2±0.08571	
	Surface Temperature	24.58 ±0.0983	
	Heat Transfer Rate	108.8±0.4567	
10	Room Temperature	39.93±0.1597	0.4276
	Inside Temperature	21.73±0.0869	
	Surface Temperature	24.93 ±0.0997	
	Heat Transfer Rate	107.1±0.458	
15	Room Temperature	40.03±0.1601	0.4324
	Inside Temperature	22.07±0.0882	
	Surface Temperature	25.45 ±0.1018	
	Heat Transfer Rate	106.5±0.4606	

In Figure 5.58, the temperature distributions of the inside of the robot are seen when the extruded polyurethane insulating material is applied to the robot. The inside temperature increases from 21.83°C to 23.35°C, while the temperature of the backside of the robot changes slightly between 24.09°C and 25.08°C. On the other hand, the right side temperatures are higher than on other surfaces, which increase from 26.21°C to almost 30°C. The left side surface temperature rises from 21.69°C to 25.63°C. However, temperatures at the top of the robot go up from 24.46°C to 26.29°C. Comparing to the top of the robot, the bottom surface temperatures vary between 21.12°C and 22.25°C.

The surface temperature changes of the battery and motor of the robot during the testing of the extruded polyurethane cover are presented in Figure 5.59. The temperature of the front side of the battery rises from 17.11°C to 18.84°C in 16 minutes. However, the temperature of the back side of the battery increases from 17.74°C to 18.44°C at the same time, which varies very close to the front side of the battery. On the other hand, the temperature of the metal surface of the robot goes up from 22.75°C to 23.44°C. Comparing to the metal surface of the motor, the plastic surface temperature changes between 24.69°C and 27.05°C.

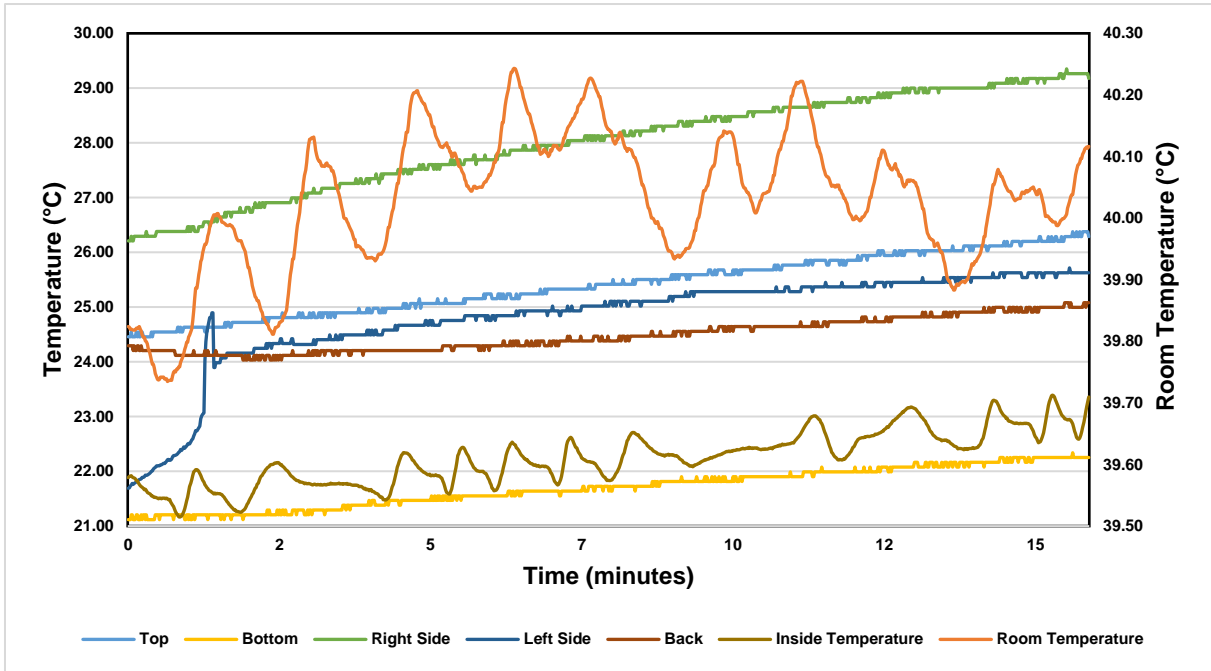


Figure 5.58. The experimental temperature distributions of the inside of the robot for the extruded polyurethane thermal insulating material at high temperature.

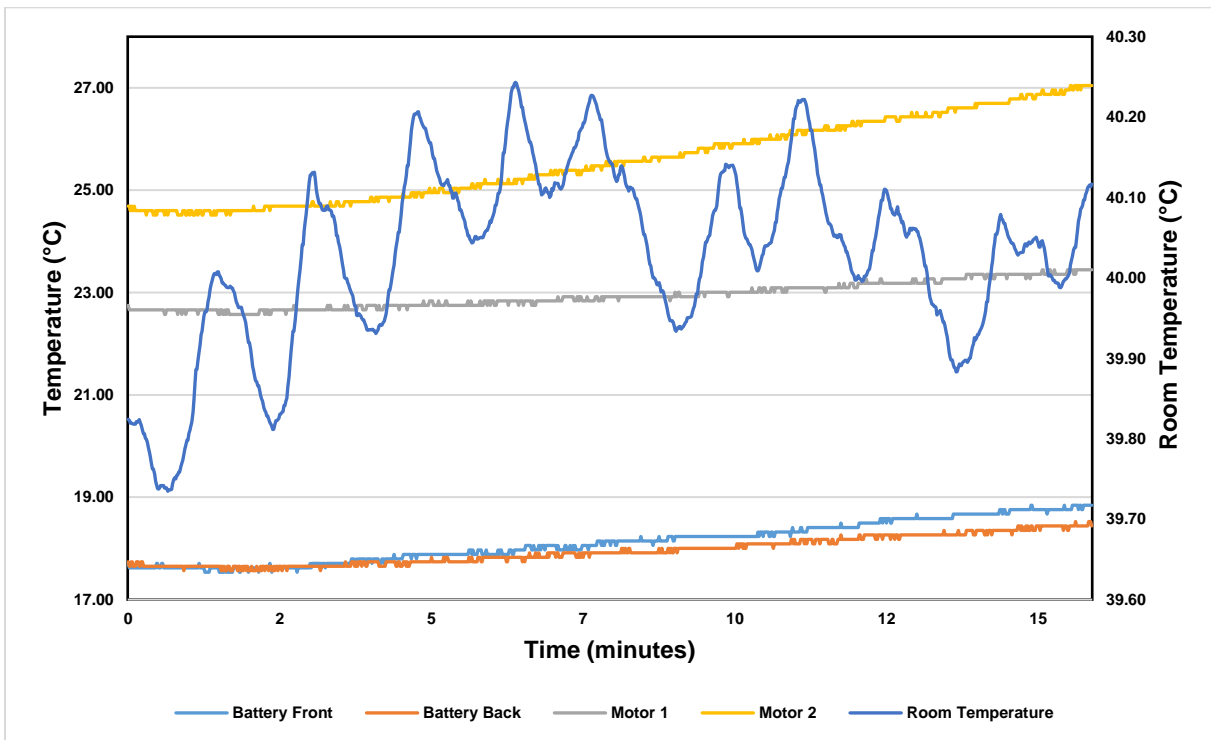


Figure 5.59. The experimental temperature distributions of the battery and motor of the robot for the extruded polyurethane insulating material at high temperature.

The heat transfer rates corresponding to the temperature difference between the inside and outside of the robot are shown in Figure 5.60. It can be seen that, in 3 minutes, the heat transfer rate gradually increases from 127.8W to 128.9W. After that, the heat transfer rate moderately decreases to 122.68W at the end of the experiment. Moreover, it can also be seen

in Figure 5.60, there is around 17°C temperature difference between the inside and outside of the robot.

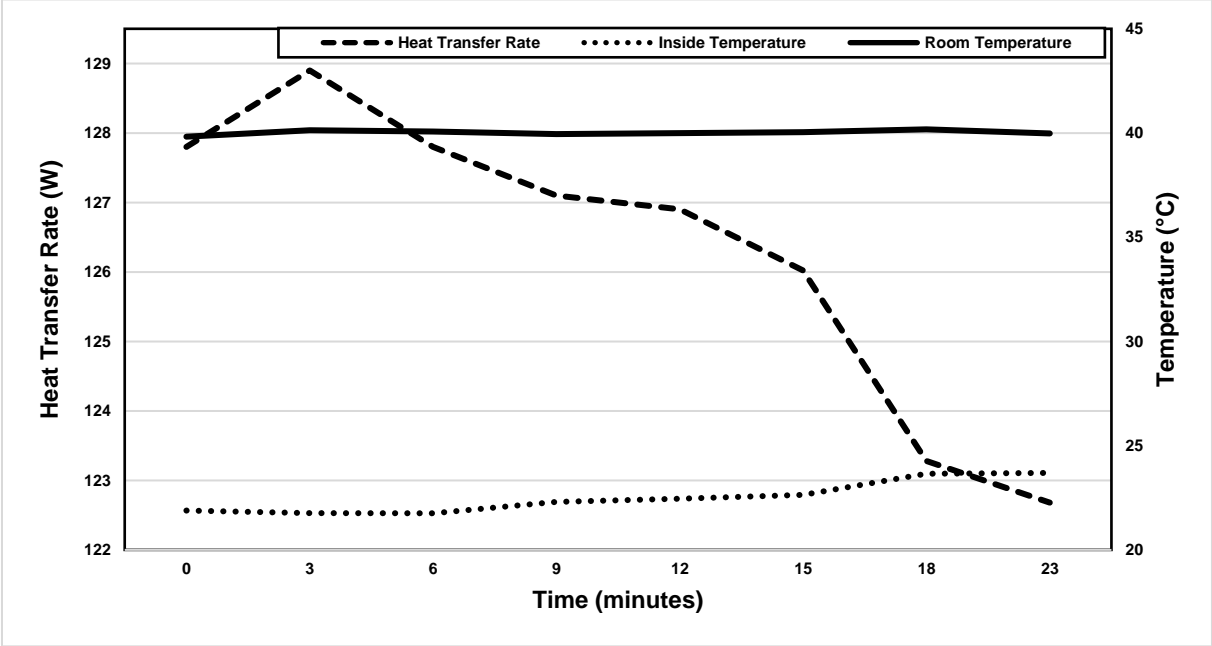


Figure 5.60. The experimental heat transfer rates of the robot for the extruded polyurethane insulating material at high temperature.

Figure 5.61 represents the energy and exergy efficiencies of the extruded polyurethane insulating material at high temperature in 16 minutes. The energy efficiency of the cover slightly decreases from 32.26% to 31.15%, while the exergy efficiency varies between 20.73% and 13.1%.

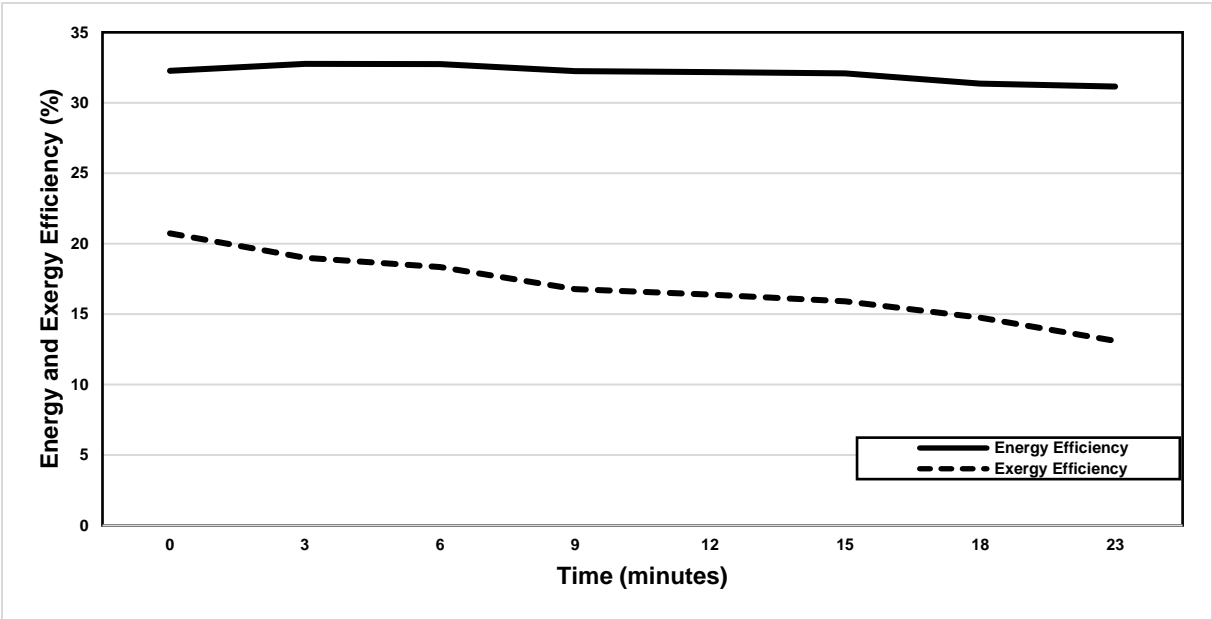


Figure 5.61. The energy and exergy efficiencies of the fiberglass insulating material at high temperature.

The comparison of the relative humidity of the inside and outside of the robot is seen in Figure 5.62 when the extruded polyurethane thermal insulating material is applied to the robot. It can be seen that the relative humidity of the room stays almost constant around 1.9%, while relative humidity of the inside of the robot gradually decreases from 17.97% to 6.66%.

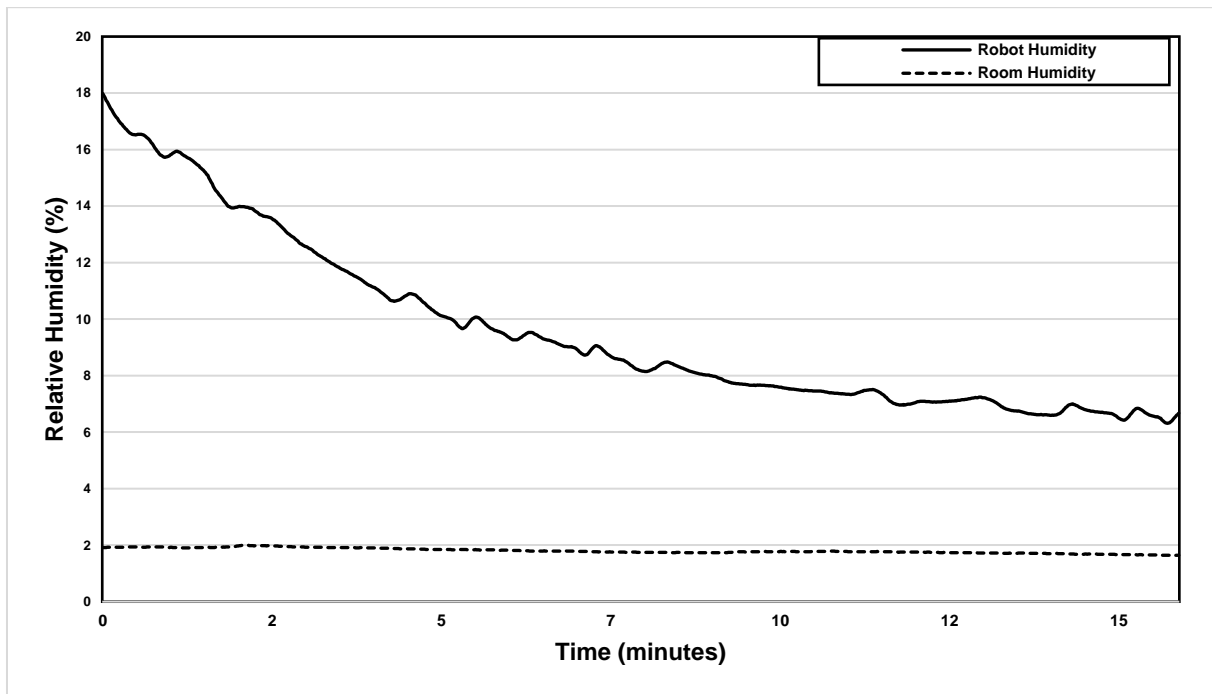


Figure 5.62. The comparison between the relative humidity percentages of the inside and outside of the robot with the extruded polyurethane insulating material at high temperature.

The air cooling thermal management system is operated inside of the robot at 40°C room temperature for 40 minutes. The surface temperatures of the robot are recorded and demonstrated in Figure 5.63. In addition, the robot is protected by the fiberglass insulating material when the air cooling thermal management system takes place in the robot. The inside temperature of the robot rises from 17.30°C to 19.02°C. The lowest recorded inside temperature is 16.96°C, and the highest is 19.34°C. On the other hand, the temperature of the right surface of the robot changes between 22.83°C and 26.23°C in 40 minutes, which are the highest recorded surface temperature values on the robot. At the same time, the surface temperature of the left side of the robot increases from 20.91°C to 23.18°C. The surface temperature of the bottom of the robot rises between 16.37°C and 20.96°C, comparing to the temperature of the top surface that increases from 24.05°C to 23.09°C. Finally, the temperature of the climatic chamber varies between 39.49°C and 40.37°C during the total duration of the experiment.

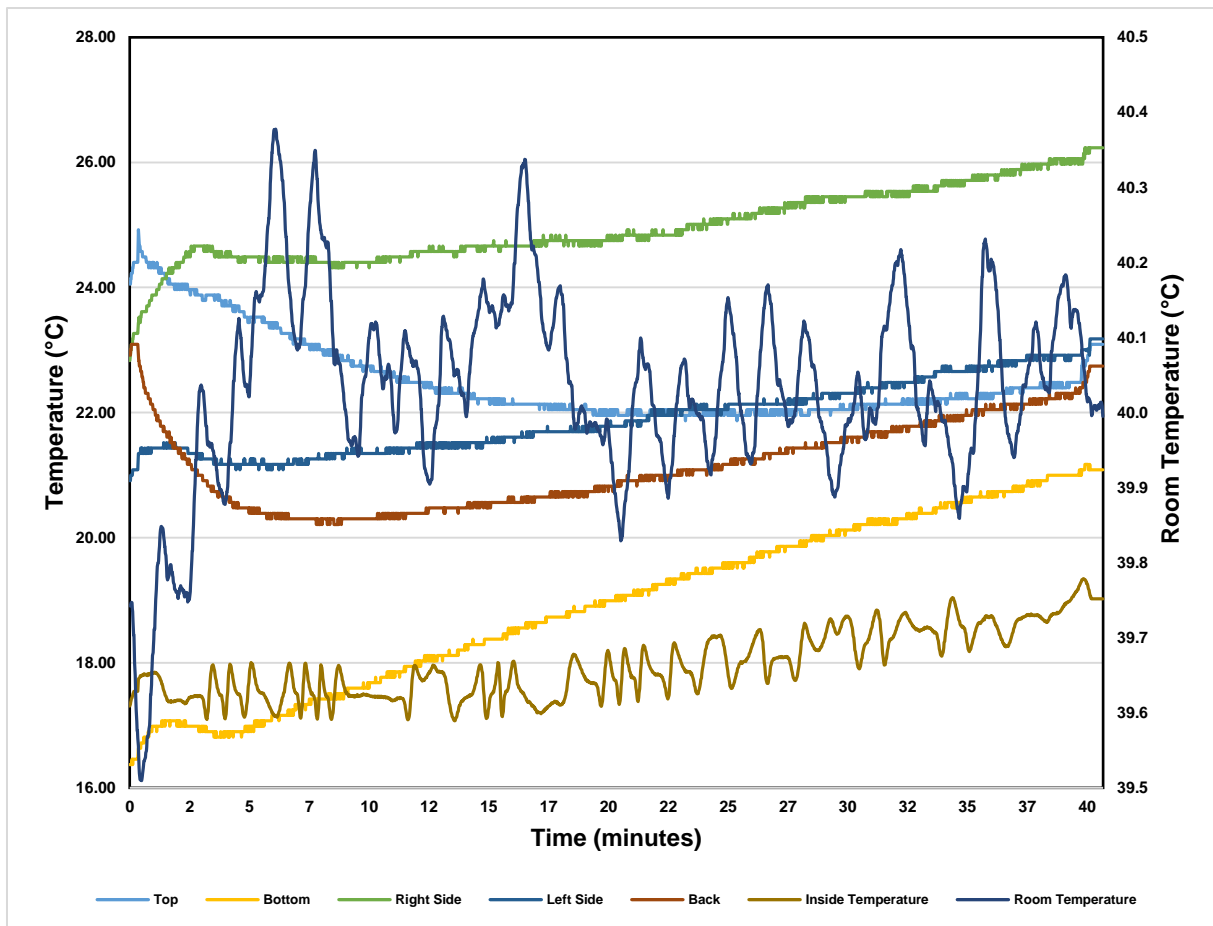


Figure 5.63. The experimental temperature distributions of the inside of the robot for the air cooling thermal management system at high temperature.

The temperature distributions on the surfaces of the battery and motor are recorded and represented in Figure 5.64 when the air cooling thermal management system is operated. The front surface of the battery has a temperature range between 13.49°C and almost 17°C, during the experiment. However, the temperature of the back side of the battery increases slightly from 13.66°C to 16.81°C. Moreover, there are two more temperature recordings for the motor of the robot. The first reading from the metal surface of the motor rises from 15.41°C to 16.86°C in 40 minutes. Finally, the second temperature reading is collected from the plastic surface of the motor, which increases up from 15.06°C to 24.05°C.

In Figure 5.65, the cooling power of the air cooling thermal management system is given in 40 minutes when the room temperature is 40°C. During the temperature drops from 12th to 15th minutes, and between 30th and 34th minutes, there is a gradual increase in the cooling power of the air cooling system. The cooling power of the air cooling thermal management system increases dramatically from 136.9W to 198.9W in the total time of the experiment.

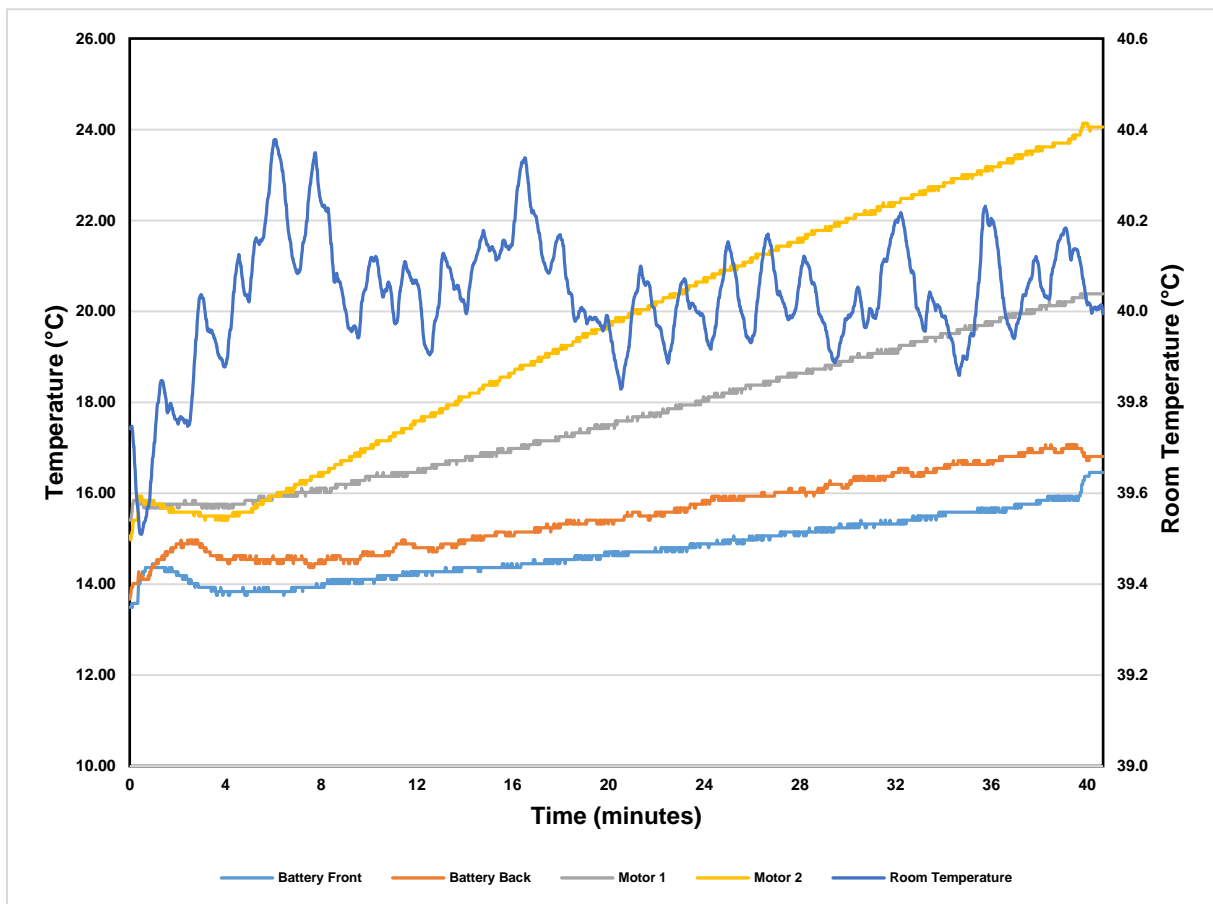


Figure 5.64. The experimental temperature distributions of the battery and motor of the robot for the air cooling thermal management system at high temperature.

The energy and exergy efficiencies of the air cooling thermal management system are analyzed, and the results are demonstrated in Figure 5.66 based on the change in the cooling power of the system in 40 minutes. The energy efficiency of the thermal management system increases gradually from 30.51% to 44.3%. However, corresponding to the decrease of the cooling power, there is an almost 1% decrease between 12th and 15th minutes, and between 30th and 34th minutes. On the other hand, the exergy efficiency of the thermal management system is lower than the energy efficiency of the system and rises slightly from 1.70% to 2.05%.

The relative humidity of the both inside and outside of the robot are also compared and shown in Figure 5.67. It can be seen that the relative humidity content of the inside of the robot decreases rapidly from 23.32% to 3.74%, while the relative humidity of the climatic chamber is almost constant at just above the 5%. However, the maximum relative humidity content of the inside of the robot is obtained as 24.5% during the experiment.

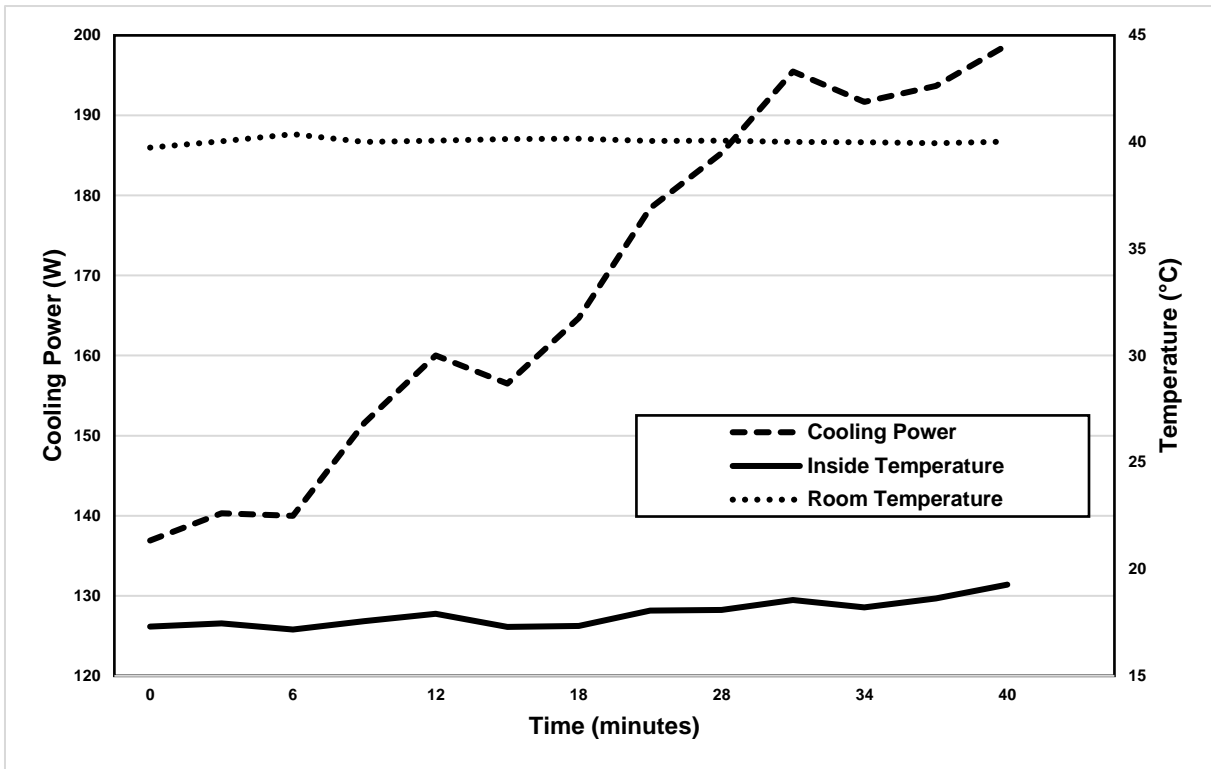


Figure 5.65. The change of the cooling power of the air cooling thermal management system in time at high temperature.

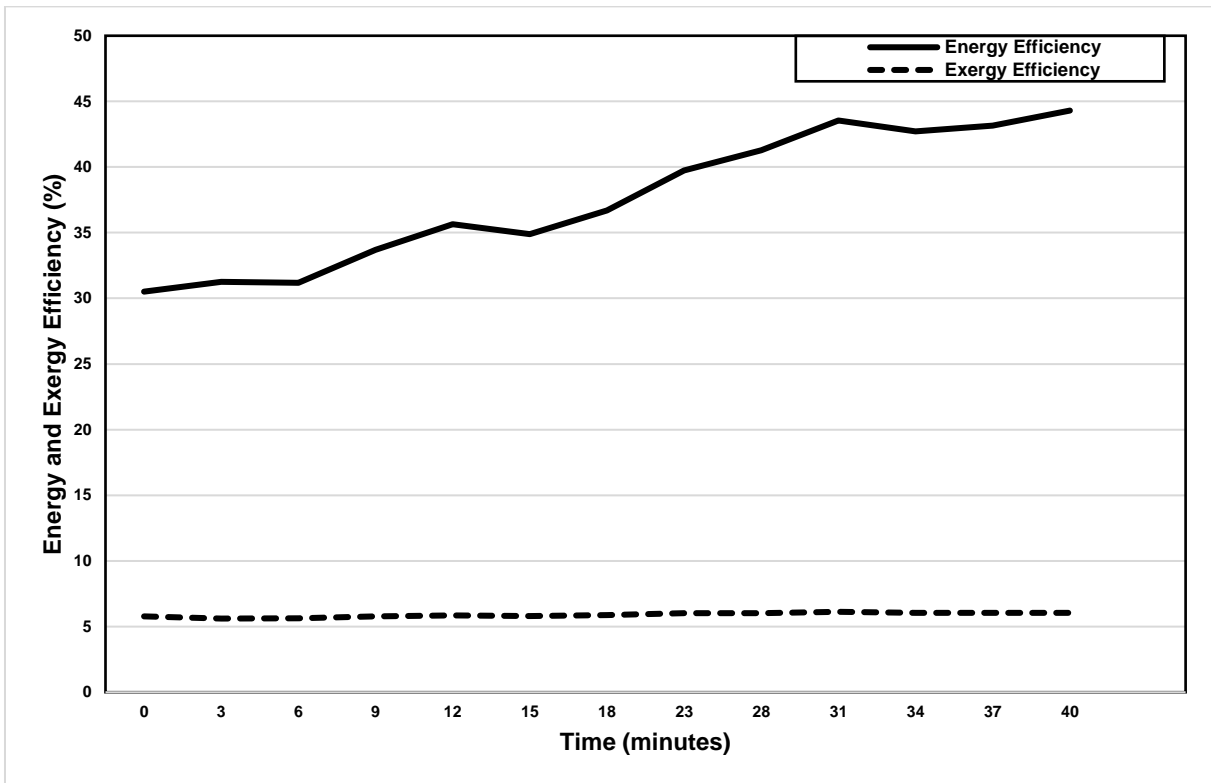


Figure 5.66. The energy and exergy efficiencies of the air cooling thermal management system at high temperature.

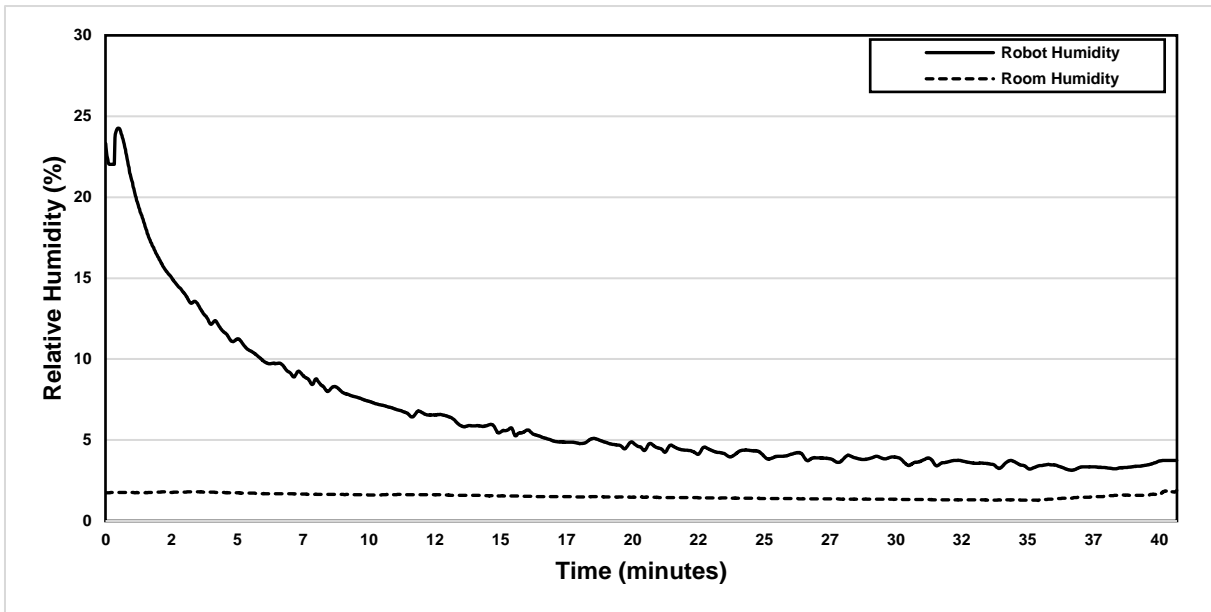


Figure 5.67. The comparison between the relative humidity percentages of the inside and outside of the robot with the air cooling thermal management system at high temperature.

Finally, the robot is tested without a thermal protection at 40°C to compare the temperature changes of the surface temperatures in Figure 5.68. It can be seen that there is a dramatic temperature increase on all surfaces of the robot in 14 minutes when the robot is not thermally protected. The inside temperature of the robot increases moderately from 26°C to 28°C, while the backside temperature of the robot rises from 28.59°C to 32°C.

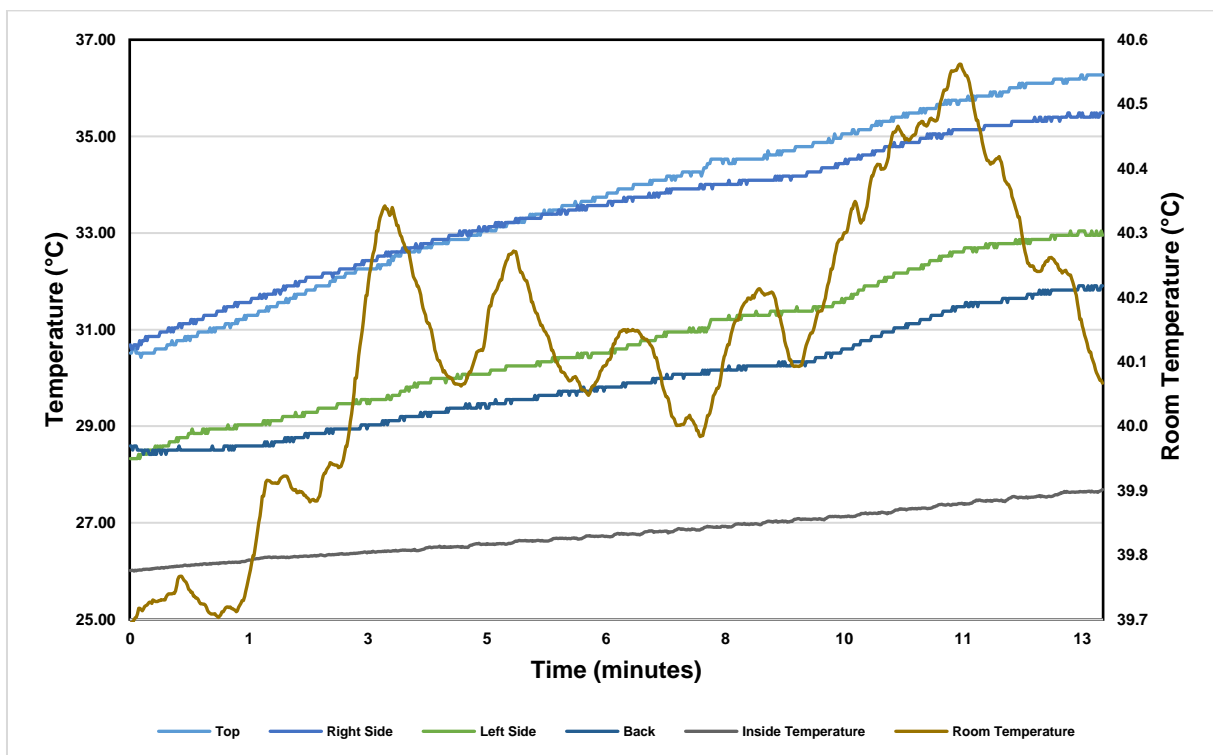


Figure 5.68. The experimental temperature distributions of the inside of the robot at high temperature.

The highest surface temperature readings are collected on the right side of the robot. The surface temperature of the right side of the robot changes between 30.69°C and 35.49°C, comparing to the surface temperature of the left side which increases from 28.33°C to 32.95°C. On the other hand, the temperature at the bottom of the robot has a slight increase between 25.0°C and 26.50°C. Moreover, the temperature of the room varies between 39.07°C and 40.1°C during the experiment.

Figure 5.69 demonstrates the temperature distributions on the surfaces of the battery and motor. The temperature of the front side of the battery increases from 22.22°C to 24.05°C, while the surface temperature of the backside of the battery varies between 21.70°C and 22.74°C. However, surface temperature recordings of the motor indicate that the temperature of the metal surface raises from 27.28°C to 28.24°C. On the other hand, the second temperature readings from the surface of the motor are the highest recorded temperatures in the robot. The temperature of the motor from the plastic surface stays almost constant in a range between 31.30°C and 21.90°C.

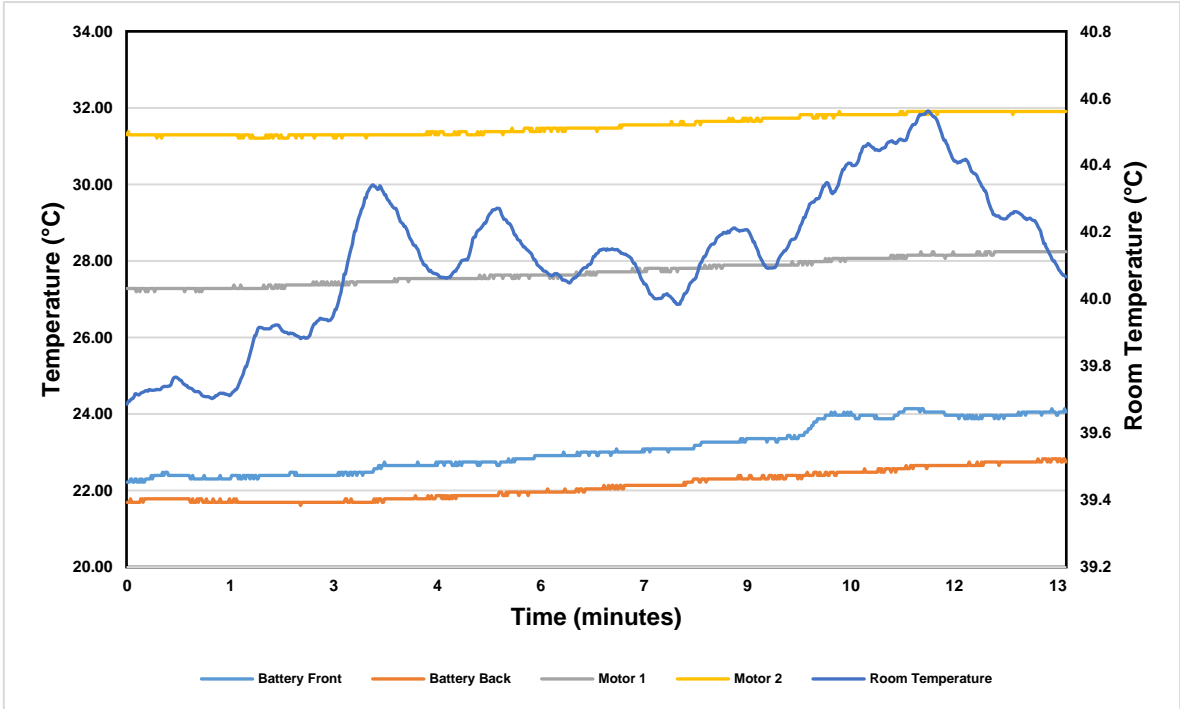


Figure 5.69. The experimental temperature distributions of the battery and motor of the robot at a high temperature.

In Figure 5.70, the heat transfer rate between the inside and outside of the robot is shown, when the room temperature is 40°C and the robot is not protected by a thermal management system. The heat transfer rate through the surface of the robot decreases moderately from 170.7W to 165.2W. It can be seen that when inside temperature approximates the room temperature, the heat transfer rate between these two points decreases.

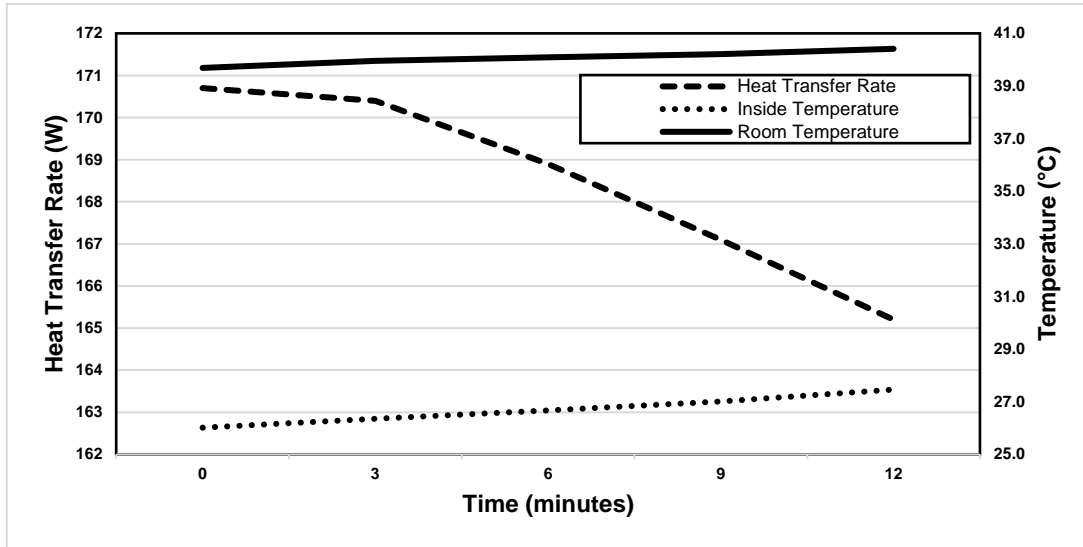


Figure 5.70. The experimental heat transfer rates of the robot at high temperature.

Since this thesis study consists of theoretical and experimental results, it is highly important to validate the theoretical results with the experimental findings. Because of this reason, Figure 5.71 represents the comparison of theoretical and experimental results at both low and high temperatures. It can be easily seen that the theoretical and experimental energy efficiency results are very close to each other. There is a 4% difference between the results for the stone wool insulating material. The energy efficiency of the stone wool is theoretically obtained as 53.98% at -25°C, and experimentally the energy efficiency can be seen as 49.91%. On the other hand, the energy efficiency of the fiberglass insulating material is 55.36% theoretically, and 48.24% experimentally at -25°C. Finally, the energy efficiency of extruded polyurethane is theoretically obtained 41.08%; however, the experimental energy efficiency is seen 31.31% at -25°C.

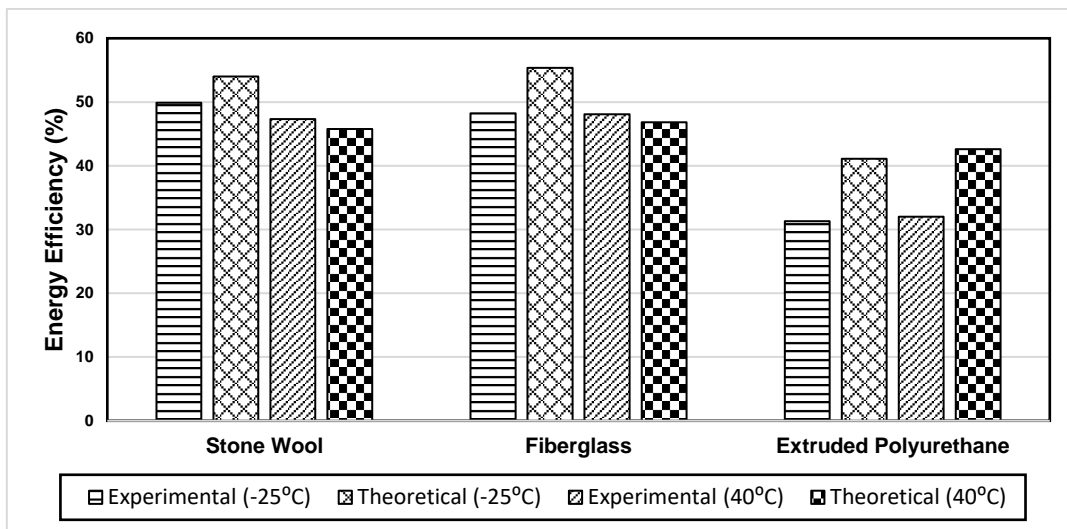


Figure 5.71. The comparison of experimental and theoretical energy efficiencies.

CHAPTER 6. CONCLUSIONS AND RECOMMENDATIONS

In this chapter, the main concluding remarks of this thesis are listed through the experimental and theoretical analyses. Moreover, the recommendations based on the results and progress of the study are also given in this chapter.

6.1. Conclusions

This thesis investigated various thermal management materials and methods for robots. Different thermal management systems and methods are analyzed to achieve a better thermal performance for electronic components of the robots. To compare these methods, theoretical and experimental analyses are performed for thermal insulating materials, phase change materials and air cooling/heating thermal management system. However, the following findings can be obtained for this study:

- According to the results of the theoretical studies, the vacuum insulation panels are have the highest thermal performance. The energy efficiencies of the vacuum insulation panels are 77.79% at -25°C and 63.02% at 40°C, and the exergy efficiencies are 66.07% at -25°C and 65.85% at 40°C. However, the lowest thermal performance is obtained for the mineralized wood fibers thermal insulating material.
- Depending on the results of the experimental studies, the stone wool thermal insulating material has the highest energy efficiencies, which are 49.91% at -25°C and 47.34% at 40°C. However, because of the high weight and rigid structure of the stone wool, it cannot be said that stone wool is the best insulating material for this case. On the other hand, its fire protection is better than other thermal insulating material options.
- The energy and exergy efficiencies of the fiberglass insulating material are also very close to the efficiencies of stone wool insulating material, which are around 48%. However, because of the lightweight and flexible structure of the fiberglass insulating material, it is highly recommended for the robotic applications.
- The extruded polyurethane is obtained as the thermal insulating material with the lowest energy and exergy efficiency values. The energy efficiencies are 31.31% at -25°C, and 31% at 40°C. However, it can be preferred for the applications where water vapor ingress is a significant factor of the operation.
- Air heating thermal management system shows a good thermal performance. However, it is highly recommended that the vortex tube should be operated with a high mass flow rate of hot stream because of the huge pressure losses.

- Air cooling thermal management system also has a good thermal performance, and achieved to keep the inside temperature at around 17°C when the ambient temperature is 40°C. However, it is very important that a water separator should be included in the system, because of the ice formation on the cold side of the vortex tube.

6.2. Recommendations

Different thermal management methods and materials are analyzed theoretically and experimentally in this thesis for the thermal management of the robots. The analyses and results are presented to provide possible solutions and evaluate thermal performance of these solutions.

The following recommendations can be listed for this thesis:

- The heat generation of the battery should be analysed for different internal resistances.
- The effect of the weather conditions on the heat transfer rate between the inside and outside of the robot should be investigated for both low and high ambient temperatures.
- Radiative heat transfer effect of the operating battery inside the robot should be investigated.
- 3-dimensional heat transfer should be developed to obtain more accurate results.
- The advanced material should be investigated which can work at extreme ambient temperatures.
- When an air/liquid thermal management system is operated, it is highly significant that the preferred liquid has to non-flammable to avoid any possible fire in the robot.
- The psychometric analyses should be performed to control the humidity depending on the change in the inside temperature of the robot.

REFERENCES

- [1] Yeh LT. Review of Heat Transfer Technologies in Electronic Equipment. *Journal of Electronic Packaging* 1995;117:333. doi:10.1115/1.2792113.
- [2] Bengel M, Pfeiffer K, Graf B, Bubeck A, Verl A. Mobile robots for offshore inspection and manipulation. 2009 IEEE/RSJ International Conference on Intelligent Robots and Systems 2009:3317–22. doi:10.1109/IROS.2009.5353885.
- [3] RISE Research Institutes of Sweden. IP-classification 2017.
- [4] Moore AL, Shi L. Emerging challenges and materials for thermal management of electronics. *Material Today* 2014;17:163–74. doi:10.1016/j.mattod.2014.04.003.
- [5] Murdock D a, Torres JER, Connors JJ, Lorenz RD. Active thermal control of power electronic modules. *IEEE Transactions on Industry Applications* 2006. doi:10.1109/TIA.2005.863905.
- [6] Garimella S V., Singhal V, Liu D. On-chip thermal management with microchannel heat sinks and integrated micropumps. *Proc IEEE* 2006;94:1534–48. doi:10.1109/JPROC.2006.879801.
- [7] Schmidt R. Challenges in Electronic Cooling - Opportunities for Enhanced Thermal Management Techniques - Microprocessor Liquid Cooled Minichannel Heat Sink. *Heat Transfer Engineering* vol. 25, 2004, p. 3–12. doi:10.1080/01457630490279986.
- [8] Krishnan S, Garimella S V. Thermal Management of Transient Power Spikes in Electronics—Phase Change Energy Storage or Copper Heat Sinks? *Journal of Electronic Packaging* 2004;126:308. doi:10.1115/1.1772411.
- [9] Wei X, Joshi Y. Optimization study of stacked micro-channel heat sinks for micro-electronic cooling. *Intersoc. Conf. Therm. Thermomechanical Phenom. Electron. Syst. IThERM*, vol. 2002–Janua, 2002, p. 441–8. doi:10.1109/ITHERM.2002.1012490.
- [10] Fedorov A ~G., Viskanta R. Three-dimensional conjugate heat transfer in the microchannel heat sink for electronic packaging. *International Journal of Heat Mass Transfer* 2000;43:399–415. doi:10.1016/s0017-9310(99)00151-9.
- [11] P. A. Johnson. Electronic chip-carrier heat sinks. US4679118 A, 1987.
- [12] P. G. Gabuzda SVT. Directed air management system for cooling multiple heat sinks. US4851965 A, 1989.
- [13] M. Anshel BGS. Electronic package with heat spreader member. US4914551 A, 1988.
- [14] Jaworski M. Thermal performance of heat spreader for electronics cooling with incorporated phase change material. *Applied Thermal Engineering* 2012;35:212–9. doi:10.1016/j.applthermaleng.2011.10.036.
- [15] M. Z. Eckblad PKB. Heat spreader, electronic package including the heat spreader, and methods of manufacturing the heat spreader. US6407922 B1, 2000.
- [16] Smalc M, Shives G, Chen G, Guggari S, Norley J, Reynolds IIRA. Thermal Performance of Natural Graphite Heat Spreaders. *ASME InterPACK*, 2005, p. 79–89. doi:10.1115/IPACK2005-73073.
- [17] H. Xie. Heat pipe lid for electronic packages. US5880524 A, 1999.
- [18] Zuo ZJ, North MT, Wert KL. High heat flux heat pipe mechanism for cooling of electronics. *IEEE Transactions on Components Packaging and Technology* 2001;24:220–5. doi:10.1109/6144.926386.
- [19] Ma HB, Wilson C, Borgmeyer B, Park K, Yu Q, Choi SUS, et al. Effect of nanofluid on the heat transport capability in an oscillating heat pipe. *Applied Physics Letters* 2006;88. doi:10.1063/1.2192971.
- [20] Rao Z, Wang S, Wu M, Lin Z, Li F. Experimental investigation on thermal management of electric vehicle battery with heat pipe. *Energy Conversion and Management* 2013;65:92–7. doi:10.1016/j.enconman.2012.08.014.
- [21] S. Tanaka, J. Sotani KN. Heat pipe type radiation for electronic apparatus. US5409055 A, 1995.
- [22] L.A. Nelson KSS. Heat pipe thermal mounting plate for cooling electronic circuit cards. US4118756 A, 1978.
- [23] Le Berre M, Launay S, Sartre V, Lallemand M. Fabrication and experimental investigation of silicon micro heat pipes for cooling electronics. *Journal of Micromechanics and Microengineering* 2003;13:436–41. doi:10.1088/0960-1317/13/3/313.
- [24] Weng YC, Cho HP, Chang CC, Chen SL. Heat pipe with PCM for electronic cooling. *Applied*

- Energy 2011;88:1825–33. doi:10.1016/j.apenergy.2010.12.004.
- [25] J.E. Murphy WTG. Electronic module with self-activated heat pipe. US4777561 A, 1988.
- [26] Tong B., Wong T., Ooi K. Closed-loop pulsating heat pipe. *Applied Thermal Engineering* 2001;21:1845–62. doi:10.1016/S1359-4311(01)00063-1.
- [27] Shahil KMF, Balandin AA. Graphene-multilayer graphene nanocomposites as highly efficient thermal interface materials. *Nano Lett* 2012;12:861–7. doi:10.1021/nl203906r.
- [28] Yu A, Ramesh P, Itkis ME, Bekyarova E, Haddon RC. Graphite nanoplatelet-epoxy composite thermal interface materials. *The Journal of Physical Chemistry* 2007;111:7565–9. doi:10.1021/jp071761s.
- [29] Mallik S, Ekere N, Best C, Bhatti R. Investigation of thermal management materials for automotive electronic control units. *Applied Thermal Engineering* 2011;31:355–62. doi:10.1016/j.applthermaleng.2010.09.023.
- [30] J. Liberty PJ. Thermally conductive interface materials and methods of using the same. US 5213868 A, 1993.
- [31] Sarvar F, Whalley D, Conway P. Thermal Interface Materials - A Review of the State of the Art. 2006 1st Electron. System Technology Conference, 2006, p. 1292–302. doi:10.1109/ESTC.2006.280178.
- [32] Goyal V, Balandin AA. Thermal properties of the hybrid graphene-metal nano-micro-composites: Applications in thermal interface materials. *Applied Physics Letters* 2012;100. doi:10.1063/1.3687173.
- [33] Shahil KMF, Balandin AA. Thermal properties of graphene and multilayer graphene: Applications in thermal interface materials. *Solid State Commun* 2012;152:1331–40. doi:10.1016/j.ssc.2012.04.034.
- [34] Xu J, Fisher TS. Enhancement of thermal interface materials with carbon nanotube arrays. *International Journal of Heat and Mass Transfer* 2006;49:1658–66. doi:10.1016/j.ijheatmasstransfer.2005.09.039.
- [35] Tong T, Zhao Y, Delzeit L, Kashani A, Meyyappan M, Majumdar A. Dense vertically aligned multiwalled carbon nanotube arrays as thermal interface materials. *IEEE Transactions on Components and Packaging Technologies* 2007;30:92–100. doi:10.1109/TCAPT.2007.892079.
- [36] Chung DDL. Thermal Interface Materials. *Journal of Material Engineering* 2001;10:56–9. doi:10.1361/105994901770345358.
- [37] M.H. Bunyan MS. Conformal thermal interface material for electronic components. US 6054198 A, 2000.
- [38] Prasher R. Thermal Interface Materials: Historical Perspective, Status, and Future Directions. *Proc IEEE* 2006;94:1571–86. doi:10.1109/JPROC.2006.879796.
- [39] Kandasamy R, Wang X-Q, Mujumdar AS. Application of phase change materials in thermal management of electronics. *Applied Thermal Engineering* 2007;27:2822–32. doi:10.1016/j.applthermaleng.2006.12.013.
- [40] Zeng C, Liu S, Shukla A. Adaptability research on phase change materials based technologies in China. *Renewable Sustainable Energy Reviews* 2017;73:145–58. doi:10.1016/j.rser.2017.01.117.
- [41] Song M, Niu F, Mao N, Hu Y, Deng S. Review on building energy performance improvement using phase change materials. *Energy and Buildings* 2018. doi:10.1016/j.enbuild.2017.10.066.
- [42] Tatsidjodoung P, Le Pierrès N, Luo L. A review of potential materials for thermal energy storage in building applications. *Renewable and Sustainable Energy Reviews* 2013;18:327–49. doi:10.1016/j.rser.2012.10.025.
- [43] Memon SA. Phase change materials integrated in building walls: A state of the art review. *Renewable and Sustainable Energy Reviews* 2014;31:870–906. doi:10.1016/j.rser.2013.12.042.
- [44] Solé A, Miró L, Barreneche C, Martorell I, Cabeza LF. Review of the T-history method to determine thermophysical properties of phase change materials (PCM). *Renewable and Sustainable Energy Reviews* 2013;26:425–36. doi:10.1016/j.rser.2013.05.066.
- [45] Liu J, Michel B, Rencz M, Tantolin C, Sarno C, Miessner R, et al. Recent progress of thermal interface material research - an overview. 14th Int. Work. Therm. Investig. ICs Syst. THERMINIC 2008, 2008. doi:10.1109/THERMINIC.2008.4669900.
- [46] Goel N, Anoop TK, Bhattacharya A, Cervantes JA, Mongia RK, Machiroutu S V, et al. Technical

- review of characterization methods for thermal interface materials (tim). 2008 11TH IEEE Intersoc. Conf. Therm. THERMOMECHANICAL Phenom. Electron. Syst. VOLS 1-3, 2008. doi:10.1109/ITHERM.2008.4544277.
- [47] Wang TH, Chen HY, Lee CC, Lai YS. High-powered thermal gel degradation evaluation on board-level HFCBGA subjected to reliability tests. *Microelectronic Engineering* 2011. doi:10.1016/j.mee.2011.06.007.
- [48] Bharatham L, Wong Shaw Fong, Torresola J, Chen Chee Koang. Qualification of Phase Change Thermal Interface Material for Wave Solder Heat Sink on FCBGA Package. 2005 7th Electronic Packaging Technolgy Conference, vol. 2, IEEE; n.d., p. 537–42. doi:10.1109/EPTC.2005.1614462.
- [49] Chiu CP, Chandran B, Mello M, Kelley K. An accelerated reliability test method to predict thermal grease pump-out in flip-chip applications. *Proc - Electron Components Technol Conf* 2001. doi:10.1109/ECTC.2001.927696.
- [50] Khuu V, Osterman M, Bar-Cohen A, Pecht M. Effects of Temperature Cycling and Elevated Temperature/Humidity on the Thermal Performance of Thermal Interface Materials. *Transactions on Device and Materials Reliability* 2009;9:379–91. doi:10.1109/TDMR.2009.2025367.
- [51] Lienhard JH. *A Heat Transfer Textbook*. 4th Edition Phlogiston Press; 2017.
- [52] Aditya L, Mahlia TMI, Rismanchi B, Ng HM, Hasan MH, Metselaar HSC, et al. A review on insulating materials for energy conservation in buildings. *Renewable and Sustainable Energy Reviews* 2017. doi:10.1016/j.rser.2017.02.034.
- [53] Papadopoulos AM. State of the art in thermal insulation materials and aims for future developments. *Energy and Buildings* 2005;37:77–86. doi:10.1016/j.enbuild.2004.05.006.
- [54] Košny J. *Short History of PCM Applications in Building Envelopes*, Springer, Cham; 2015, p. 21–59. doi:10.1007/978-3-319-14286-9_2.
- [55] Álvarez S, Cabeza LF, Ruiz-Pardo A, Castell A, Tenorio JA. Building integration of PCM for natural cooling of buildings. *Applied Energy* 2013. doi:10.1016/j.apenergy.2013.01.080.
- [56] Kymäläinen HR, Sjöberg AM. Flax and hemp fibres as raw materials for thermal insulations. *Buildings and Environment* 2008;43:1261–9. doi:10.1016/j.buildenv.2007.03.006.
- [57] D. Murphy, H. Behring HW. *The Use of Flax and Hemp Materials for Insulation Processing of Flax and Other Bast Plants*. Symp. Pozn., Poland: n.d., p. 79–84.
- [58] Roy A, Ender F, Azadmehr M, Aasmundtveit KE. CMOS micro-heater design for direct integration of carbon nanotubes. *Microelectron Reliability* 2017;79:517–25. doi:10.1016/j.microrel.2017.05.031.
- [59] Scorzoni A, Caputo D, Petrucci G, Placidi P, Zampolli S, De Cesare G, et al. Design and experimental characterization of thin film heaters on glass substrate for Lab-on-Chip applications. *Sensors Actuators, Applied Physics* 2015;229:203–10. doi:10.1016/j.sna.2015.03.011.
- [60] Li P, Ma JG, Xu HY, Lin D, Xue XD, Yan XZ, et al. Flexible transparent heaters based on silver nanotrough meshes. *Journal of Alloys and Compounds* 2016;664:764–9. doi:10.1016/j.jallcom.2015.12.216.
- [61] Chen K, Wang S, Song M, Chen L. Structure optimization of parallel air-cooled battery thermal management system. *International Journal of Heat and Mass Transfer* 2017;111:943–52. doi:10.1016/j.ijheatmasstransfer.2017.04.026.
- [62] Xie J, Ge Z, Zang M, Wang S. Structural optimization of lithium-ion battery pack with forced air cooling system. *Applied Thermal Engineering* 2017;126:583–93. doi:10.1016/j.applthermaleng.2017.07.143.
- [63] Hong S, Zhang X, Chen K, Wang S. Design of flow configuration for parallel air-cooled battery thermal management system with secondary vent. *International Journal of Heat and Mass Transfer* 2018;116:1204–12. doi:10.1016/j.ijheatmasstransfer.2017.09.092.
- [64] Yang T, Yang N, Zhang X, Li G. Investigation of the thermal performance of axial-flow air cooling for the lithium-ion battery pack. *International Journal of Thermal Sciences* 2016;108:132–44. doi:10.1016/j.ijthermalsci.2016.05.009.
- [65] Sun H, Dixon R. Development of cooling strategy for an air cooled lithium-ion battery pack. *Journal of Power Sources* 2014;272:404–14. doi:10.1016/j.jpowsour.2014.08.107.

- [66] Habibi A, Halgamuge SK. A Review on efficient thermal management of air- and liquid-cooled data centers: From chip to the cooling system. *Applied Energy* 2017;205:1165–88. doi:10.1016/j.apenergy.2017.08.037.
- [67] Rao Z, Wang S. A review of power battery thermal energy management. *Renewable and Sustainable Energy Reviews* 2011;15:4554–71. doi:10.1016/j.rser.2011.07.096.
- [68] Malik M, Dincer I, Rosen MA, Mathew M, Fowler M. Thermal and electrical performance evaluations of series connected Li-ion batteries in a pack with liquid cooling. *Applied Thermal Engineering* 2018;129:472–81. doi:10.1016/J.APPLTHERMALENG.2017.10.029.
- [69] Chang JY, Park HS, Jo JI, Julia S. A system design of liquid cooling computer based on the micro cooling technology. *Thermomechanical Phenom. Electron. Syst. -Proceedings Intersoc. Conf.*, vol. 2006, 2006, p. 157–60. doi:10.1109/ITHERM.2006.1645337.
- [70] Urata J, Hirose T, Namiki Y, Nakanishi Y, Mizuuchi I, Inaba M. Thermal control of electrical motors for high-power humanoid robots. *2008 IEEE/RSJ Int. Conf. Intell. Robot. Syst. IROS*, 2008, p. 2047–52. doi:10.1109/IROS.2008.4651110.
- [71] X.Shi. Low-Temperature Thermoelectric Properties of PtSb_{2-x} Te_x for Cryogenic Peltier Cooling Applications. *Journal of Electronic Materials* 2015;44:1562–5. doi:10.1007/s11664-014-3480-z.
- [72] Zhang X, Zhao L-D. Thermoelectric materials: Energy conversion between heat and electricity. *Journal of Electronic Materials* 2015;1:92–105. doi:10.1016/j.jmat.2015.01.001.
- [73] Zhao D, Tan G. A review of thermoelectric cooling: Materials, modeling and applications. *Applied Thermal Engineering* 2014;66:15–24. doi:10.1016/j.applthermaleng.2014.01.074.
- [74] Kim YM, Kim SY, Shin SW, Sohn JY. Contribution of natural ventilation in a double skin envelope to heating load reduction in winter. *Buildings and Environment* 2009;44:2236–44. doi:10.1016/j.buildenv.2009.02.013.
- [75] Shi Y, Mei D, Yao Z, Wang Y, Liu H, Chen Z. Nominal power density analysis of thermoelectric pins with non-constant cross sections. *Energy Conversion Management* 2015;97:1–6. doi:10.1016/j.enconman.2015.02.046.
- [76] Astrain D, Vián JG, Domínguez M. Increase of COP in the thermoelectric refrigeration by the optimization of heat dissipation. *Applied Thermal Engineering* 2003;23:2183–200. doi:10.1016/S1359-4311(03)00202-3.
- [77] Tsai CY, Chien HT, Ding PP, Chan B, Luh TY, Chen PH. Effect of structural character of gold nanoparticles in nanofluid on heat pipe thermal performance. *Material Letters* 2004. doi:10.1016/j.matlet.2003.10.009.
- [78] Wang Y, Vafai K. An experimental investigation of the thermal performance of an asymmetrical flat plate heat pipe. *International Journal of Heat Mass Transfer* 2000. doi:10.1016/S0017-9310(99)00300-2.
- [79] Chuang P-YA. An Improved Steady-State Model of Loop Heat Pipes Based on Experimental and Theoretical Analyses 2003.
- [80] Hamdan A, McLanahan A, Richards R, Richards C. Characterization of a liquid-metal microdroplet thermal interface material. *Experimental Thermal and Fluid Science* 2011. doi:10.1016/j.expthermflusci.2011.04.012.
- [81] Narumanchi S, Mihalic M, Kelly K, Eesley G. Thermal interface materials for power electronics applications. *11th Intersoc Conf Therm Thermomechanical Phenom Electron Syst* 2008:395–404. doi:10.1109/ITHERM.2008.4544297.
- [82] Heller EB, Youcef-Toumi K. Analysis and control of a thermal management system for robots in temperature-restricted environments. *Proceeding of the American Control Conference*, 2014, p. 3335–40. doi:10.1109/ACC.2014.6858774.
- [83] Kim SY, Hwang K, Moon J, Karng SW. Thermal management of liquid-cooled cold plates for multiple heat sources in a humanoid robot. *IMPACT Conf. 2009 Int. 3D IC Conf. - Proc.*, 2009, p. 453–6. doi:10.1109/IMPACT.2009.5382215.
- [84] Swanson TD, Birur GC. NASA thermal control technologies for robotic spacecraft. *Applied Thermal Engineering*, 2003. doi:10.1016/S1359-4311(03)00036-X.
- [85] Chein R, Huang G. Thermoelectric cooler application in electronic cooling. *Applied Thermal Engineering* 2004;24:2207–17. doi:10.1016/j.applthermaleng.2004.03.001.
- [86] Alaoui C, Salameh ZM. A novel thermal management for electric and hybrid vehicles. *IEEE*

- Transfer Vehicle Technolgy 2005;54:468–76. doi:10.1109/TVT.2004.842444.
- [87] Ismail KAR, Gonçalves MM. Thermal performance of a pcm storage unit. *Energy Conversation Management* 1999;40:115–38. doi:10.1016/S0196-8904(98)00042-9.
- [88] Abd El-Baky MA, Mohamed MM. Heat pipe heat exchanger for heat recovery in air conditioning. *Applied Thermal Engineering* 2007;27:795–801. doi:10.1016/j.applthermaleng.2006.10.020.
- [89] Lin C, Chung DDL. Graphite nanoplatelet pastes vs. carbon black pastes as thermal interface materials. *Carbon N Y* 2009;47:295–305. doi:10.1016/j.carbon.2008.10.011.
- [90] Cengel Y. Heat Transfer: A Practical Approach. *Journal of Chemical Information and Modeling* 2013. doi:10.1017/CBO9781107415324.004.
- [91] Schiavoni S, D’Alessandro F, Bianchi F, Asdrubali F. Insulating materials for the building sector: A review and comparative analysis. *Renewable and Sustainable Energy Reviews* 2016. doi:10.1016/j.rser.2016.05.045.
- [92] Vélez C, Ortiz De Zárate JM, Khayet M. Thermal properties of n-pentadecane, n-heptadecane and n-nonadecane in the solid/liquid phase change region. *Int J Therm Sci* 2015;94:139–46. doi:10.1016/j.ijthermalsci.2015.03.001.
- [93] Zhao R, Gu J, Liu J. Optimization of a phase change material based internal cooling system for cylindrical Li-ion battery pack and a hybrid cooling design. *Energy* 2017;135:811–22. doi:10.1016/j.energy.2017.06.168.